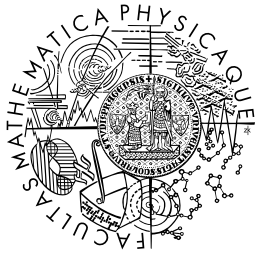

FACULTY
OF MATHEMATICS
AND PHYSICS
Charles University

MASTER THESIS

Filip Švábik

Study of screen level temperature dependency on interactions and feedbacks of physics parameterizations in numerical weather prediction and climate models

Department of Atmospheric Physics

Supervisor of the master thesis: Mgr. Peter Huszár, Ph.D.

Study programme: Physics

Study branch: Meteorology and Climatology

Prague 2021

I declare that I carried out this master thesis independently, and only with the cited sources, literature and other professional sources. It has not been used to obtain another or the same degree.

I understand that my work relates to the rights and obligations under the Act No. 121/2000 Sb., the Copyright Act, as amended, in particular the fact that the Charles University has the right to conclude a license agreement on the use of this work as a school work pursuant to Section 60 subsection 1 of the Copyright Act.

In Prague 6th January 2021 Filip Švábik

I would like to thank to following people who supported me very much during this work:

Mgr. Peter Huszár, Ph.D. who supervised me and introduced me to regional climate modelling,

RNDr. Radmila Brožková, CSc. who contributed exquisite advices from the field of Numerical Weather Prediction,

Mgr. Ján Mašek, Ph.D. who spent enormous amount of time explaining things into detail during our discussions so that I could finally understand them,

my fiancée Katka who helped to make my life better on everyday basis.

Title: Study of screen level temperature dependency on interactions and feedbacks of physics parameterizations in numerical weather prediction and climate models

Author: Filip Švábik

Department: Department of Atmospheric Physics

Supervisor: Mgr. Peter Huszár, Ph.D., Department of Atmospheric Physics

Abstract: Screen level temperature is measured at 2 meters above the ground. It is one of the most used atmospheric characteristics in various applications in meteorology and other fields related to weather prediction. Essential is not only the knowledge of its current state, but also its prediction. It is forecasted by numerical weather prediction (NWP) models from the atmospheric current state. Its long-term characteristics can be obtained from the integration of climate models. This text discusses fundamental parametrizations, mostly related to temperature forecast, used in the NWP model ALADIN and the regional climate model RegCM. Physical processes which influence temperature are studied using ALADIN in several cases which include the presence of low cloudiness, gravity waves and inappropriate thermic coefficient. A detailed description of the most relevant parametrization schemes is given and the results are studied in a form of individual feedback loops. Most dominant processes are also found. However, the level of 2 meters above the ground is not the model level, so temperature at 2 meters is obtained by interpolation from the surface temperature and the lowest model level temperature. Using RegCM, two differently complex interpolation schemes are compared to each other.

Keywords: numerical weather prediction model, regional climate model, parameterizations of physical processes, model physics-dynamics interface, screen level temperature

Contents

Introduction **2**

1 ALADIN and RegCM model **3**
1.1 Basic differences . . . 3
1.2 Dynamical core . . . 4
1.3 Parametrizations . . . 5
1.4 Verification and diagnostic tools . . . 8

2 Influence of selected parametrizations on temperature **10**
2.1 Low cloudiness case . . . 12
2.1.1 Relevant parametrizations . . . 15
2.1.2 Reference experiment . . . 17
2.1.3 Experiment with unified critical relative humidity profiles . 19
2.1.4 Feedback loops . . . 20
2.1.5 Verification . . . 31
2.1.6 Conclusion . . . 33
2.2 Gravity waves case . . . 35
2.2.1 Relevant parametrizations . . . 35
2.2.2 Reference experiment . . . 40
2.2.3 Experiment with parametrized gravity waves . . . 41
2.2.4 Feedback loops . . . 43
2.2.5 Verification . . . 53
2.2.6 Conclusion . . . 55
2.3 Overestimated minimum temperature case . . . 55
2.3.1 Relevant parametrizations . . . 56
2.3.2 Reference experiments . . . 59
2.3.3 Experiments . . . 60
2.3.4 Conclusion . . . 62

3 Influence of screen level interpolation on 2m temperature **64**
3.1 ALADIN screen level interpolation case . . . 66
3.1.1 Relevant parametrizations . . . 67
3.1.2 Reference experiments . . . 70
3.1.3 Experiments . . . 71
3.1.4 Conclusion . . . 75

Conclusion **77**

Bibliography **79**

List of Figures **84**

List of Tables **90**

List of Abbreviations **91**

Introduction

Atmospheric temperature is one of the most used characteristics in meteorology and also other fields which are related to weather prediction. Its prediction is based upon state-of-the-art numerical weather prediction (NWP) models which use the knowledge of its current state to forecast its evolution in few days, or even weeks, ahead. On the other side are climate models which estimate its long-term characteristics over many years.

Both NWP and climate models use parametrization schemes to handle complex sub-grid scale processes. The aim of this text is to present fundamental parametrizations in the NWP model ALADIN and the regional climate model RegCM. Physical processes interacts between themselves and it is essential to understand individual feedback loops to develop better weather forecast and climate models in the future.

However, to be able to create better models, they must be verified to real observations of the atmosphere. One of the most important quantity is the screen level temperature measured at 2 m above the ground. It is obtained by specific interpolation which uses the surface temperature and the lowest model level temperature and handles strong temperature gradients near the surface.

Chapter 1 gives the overview of both ALADIN and RegCM model. Their history, dynamical core, used parametrizations and verification is presented.

Chapter 2 presents the reader detailed description of individual studied cases using the model ALADIN. First, influence of low cloudiness on temperature is studied. Next, gravity waves in the model are once disabled and once enabled which provide an opportunity to study their affect on temperature. Finally, we will look at overestimated minimum temperatures and see what process is behind it.

Chapter 3 provides a study of two different screen level temperature interpolations using the model RegCM. An original RegCM interpolation which is very complex will be compared to ALADIN screen level interpolation which is translated from ALADIN code to RegCM code.

1. ALADIN and RegCM model

1.1 Basic differences

This paragraph is compiled from paper Termonia et al. (2018). The **ALADIN** system (fr. *Aire Limitée Adaptation Dynamique Développement International*, transl. International Development for Limited-Area Dynamical Adaptation) is a numerical weather prediction (NWP) system developed by the international ALADIN consortium for operational weather forecasting and research purposes. The consortium was created in 1990 and now consists of 16 European and northern African countries. The ALADIN system (hereafter ALADIN) is a set of pre-processing, data assimilation, forecast model, post-processing and verification software codes and it is based on a code that is shared with the global model IFS (Integrated Forecast System) of the ECMWF (European Centre for Medium-range Weather Forecasts) and the ARPEGE model (fr. *Action de Recherche Petite Echelle Grande Echelle*, transl. Research Project on Small and Large Scales) of Météo-France. Historically, ALADIN was created as a limited area model (LAM) of the ARPEGE model and today provides a multitude of high-resolution LAM configurations. The three of them, called Canonical Model Configurations (CMCs), are thoroughly validated and prepared to be used for the operational weather forecasting:

- the ALADIN baseline CMC: The oldest LAM configuration which uses the ARPEGE physics. It is maintained only in order to keep a close link with the global model ARPEGE. It could be used as a mesoscale model, but it undergoes a minimal validation.
- the AROME (Application of Research to Operations at Mesoscale) CMC: It has been developed to run in convection-permitting resolutions of 2.5 km and higher.
- the ALARO (ALADIN–AROME) CMC: Its aim is to provide a setup that can also be used in intermediate resolutions between the mesoscale and the convection-permitting scales, the so-called gray-zone. This configuration is used operationally at Czech Hydrometeorological Institute (CHMI).

This paragraph is compiled from paper Elguindi et al. (2014). The **RegCM** (Regional Climate Model) system is a regional climate model supported through Regional Climate Research Network (RegCNET), a widespread network of scientists coordinated by Abdus Salam International Centre for Theoretical Physics (ICTP). The first version of the model, called RegCM1, was developed in 1989 and was built based on the MM4 model (Penn State/NCAR Mesoscale Model, version 4) of Penn State and National Center for Atmospheric Research (NCAR). It has also been the first LAM developed for long-term regional climate simulations. As a LAM model, the RegCM system (hereafter RegCM) downscales climate change projections obtained from general circulation models (GCMs) to better characterize regional variability due to more detailed geographical features. Since the first version, the model has evolved both in terms of software codes and physics representations which has lead to the fourth version, RegCM4 (Giorgi

et al., 2012), with the latest version 4.7 released in 2018. RegCM is a community model designed to be public, user friendly, portable and open source, so it can be applied to any region in the world. It is used by a large community for a wide range of regional climate studies, such as paleoclimate and future climate projections. The later are often targeted on urban areas which are affected by anthropogenic forcings and land-use modifications (Huszár et al., 2016, 2020).

1.2 Dynamical core

The dynamical core of a model discretises equations of motion that resolve flow features. Following paragraph is compiled from papers Termonia et al. (2018) and Wang et al. (2018). **ALADIN** can be run with:

- a hydrostatic core: It solves the hydrostatic primitive equations that are obtained from the fully compressible Euler equations under the hydrostatic approximation.
- a nonhydrostatic core (ALADIN-NH): It solves the fully compressible Euler equations (Bénard et al., 2010) and has two additional prognostic variables compared to the hydrostatic core: the nonhydrostatic pressure departure and the vertical divergence. Typically, it is used for resolutions of 3 km and higher.

Both dynamical cores assume spherical Earth and employ the shallow-atmosphere approximation. Also, both of them use a mass-based hybrid terrain-following coordinate η for the vertical coordinate system (Laprise, 1992). The dynamical cores utilize a two-time level semi-implicit semi-Lagrangian scheme (Temperton et al., 2001) and apply bi-Fourier spectral transform in the horizontal. The vertical discretization is based on finite differences (Simmons and Burridge, 1981) or finite elements; see Untch and Hortal (2004) for the hydrostatic case and Vivoda and Smolíková (2013) for the nonhydrostatic case.

This paragraph is compiled from paper Elguindi et al. (2014). **RegCM** also implements two dynamical cores:

- a hydrostatic core: Its origin is in the MM4 model and it solves dynamic equations that are obtained from the compressible Euler equations under the hydrostatic approximation. It is used typically for resolutions of 10 km and coarser.
- a nonhydrostatic core: Since the release of the version 4.5 in 2016, the model can be run with a nonhydrostatic core which allows to use resolutions of few kilometers and higher.

Both cores are described in detail in Grell et al. (1994) because they are similar to those of the MM5 model (Penn State/NCAR Mesoscale Model, version 5); now superseded by the WRF model (Weather Research and Forecasting) with a large worldwide community. RegCM uses a terrain-following vertical coordinate σ, which is having a time-independent relation to geometrical height in nonhydrostatic case, and a split-explicit time integration scheme. Its horizontal and vertical discretization is based on finite differences, i.e. computations are done only in grid-point space. The model runs on an Arakawa B-grid in which thermodynamical and wind variables are horizontally staggered.

1.3 Parametrizations

The physics parametrizations describe how unresolved processes on a sub-grid scale will influence the resolved processes on a grid scale. The brief characteristics of **ALADIN** parametrizations are mentioned specifically for the ALARO CMC. For simplicity, the term ALADIN will hereafter refer to this particular configuration, used operationally at CHMI, because it is utilized in the following sections of the text. The summary of used parametrizations can be found in Table 1.1. The description of parametrizations is based on Termonia et al. (2018) and Wang et al. (2018). Some parametrizations will be characterized later in more detail. Unlike the dynamical core computations that are split between grid-point and spectral space, parametrizations are computed solely in grid-point space.

Deep convection, together with the treatment of microphysics, is parametrized by the 3MT (Modular Multiscale Microphysics and Transport) scheme (Gerard et al., 2009). The detailed meaning of the acronym is:

- Multi-scale: The scheme is developed to work across resolutions where moist deep convection is partly resolved, i.e. the gray-zone.
- Modular: The scheme uses a consistent set of thermodynamic assumptions and a flux-conservative interface which enables exchangeable parametrizations of individual processes.
- Microphysics and Transport: The scheme does not separate scales, but moist and dry processes, which is a more natural approach.

A time step in the 3MT scheme is organized in the so-called cascade:

1. Resolved condensation and updraft: First, grid-scale condensation (evaporation) is computed in the so-called thermodynamic adjustment. Moisture and temperature fields passed to consequent steps are accordingly modified, in order to prevent a double counting and help self switch-off behaviour when drafts start to be resolved. Then, a convective condensation on a sub-grid scale (in an updraft) is solved while using the prognostic equations for the updraft velocity and its mesh area fraction. Finally, the computed fluxes of suspended cloud liquid and ice water, from both condensation processes, are joined together and passed to the microphysics part.
2. Microphysics: The thermodynamic equations are derived in a total mass-based framework which express all relevant budgets in a flux-conservative form (Catry et al., 2007). The microphysics takes into account the geometry of clouds and precipitation vertical overlaps, and distinguishes five hydrometeors: suspended cloud liquid water, suspended cloud ice water, rain, snow and pseudo-graupel. The pseudo-graupel is sedimenting as rain, but has thermodynamic properties of snow.

   The foundations of autoconversion, collection, evaporation and freezing-melting parametrizations were developed by Lopez (2002). Other parametrized effects include, for example, the sedimentation of precipitation with variable fall speed of species (Geleyn et al., 2008) and the Wegener–Bergeron–Findeisen effect (Hage, 1995).

3. Downdraft: The precipitation flux from microphysics, consisting of rain, snow and pseudo-graupel, is passed to a downdraft computation which treats transport and evaporation of precipitation on a sub-grid scale. It uses the prognostic equations for the downdraft velocity and its mesh area fraction, similiar to the updraft computation. An interesting property of the 3MT scheme is that the downdraft is independent of an updraft existence.

The 3MT scheme uses prognostic treatment where possible, leading to smoother temporal behaviour with memory. It thus avoids a quasi-equilibrium approach with the stationary cloud hypothesis. The prognostic approach to a mass-flux eliminates the need of detrainment parameterization, only entrainment is parameterized. Transport has two independent closures: first for an updraft, second for a downdraft. They provide relations for tendencies of the updraft and downdraft mesh area fractions (Brožková and Mašek, 2020).

Turbulence and shallow convection is parametrized by the TOUCANS (Third Order Moments Unified Condensation Accounting and N-Dependent Solver) parameterization scheme (Bašták Ďurán et al., 2014, 2018), the so-called model II. It is based on a unified treatment of stability functions, applicable in both stable and unstable conditions. This scheme emulates several turbulence models that are compliant with observational evidence that there is no stability limit suppressing the turbulent mixing completely. The concept of the critical Richardson number, beyond which turbulence would cease, is abandoned. The TOUCANS scheme uses prognostic equations for turbulent kinetic energy and total turbulent energy as well as a parametrization of third order moments (TOMs). That makes it possible to better treat the anisotropy of the flow and to account for countergradient heat fluxes which simple eddy diffusivity schemes do not permit.

Radiative transfer is parametrized by the ACRANEB2 (fr. *Actif Calcul de Rayonement et Nébulosité, version 2*; transl. Active Radiation and Cloudiness Calculation, version 2) scheme (Mašek et al., 2016; Geleyn et al., 2017). Its key feature is a full cloud-radiation interaction using actual cloud and intermittently updated gaseous optical properties. That is made affordable via a broadband solver applied at every grid point and time step to account for the fast development and variability of cloudiness. This scheme uses single short-wave and single long-wave spectral intervals with the so-called net exchanged rate decomposition with bracketing.

For resolutions of roughly 5 km and coarser, a parametrization of sub-grid orographic effects is needed (Catry, 2006). The parametrization represents gravity wave drag, wave deposition, wave trapping, form drag and lift effects.

Land surface processes are parametrized by the ISBA (fr. *Interactions Sol-Biosphère-Atmosphère*, transl. Interactions between Soil, Biosphere and Atmosphere) scheme (Noilhan and Planton, 1989a; Noilhan and Mahfouf, 1996) which describes the energetic and hydrous exchanges at the continental surface. Because it was designed for meteorological models, it uses minimum parameters while preserving the representation of physical phenomena at the interface. Its main task is to model thermal and hydrous properties of the soil, which depend on its composition and water content; thermal inertia of the vegetation and its ability to immediately evaporate precipitation it intercepts, and the surface soil evaporation. The ISBA parameters, which describe, for example, dominant types of soil and vegetation and their physical properties, are specified within each grid

cell. The scheme also solves the prognostic equation of surface temperature which is one of the most important parameters used in the computation of screen level temperature.

In **RegCM**, one can choose from several parametrizations of a given physical process to better adapt the model for the usage in a wide range of regional climate studies. Hence, we will briefly describe only such parametrizations that are used in our study and that describe similar or the same processes as the aforementioned parametrizations in ALADIN. The summary of used parametrizations can be found in Table 1.1. The description is based on Giorgi et al. (2012) and Elguindi et al. (2014). The parametrizations are computed solely in grid-point space, similar to dynamical core computations.

Shallow and deep convection are parametrized by the Tiedke scheme (Tiedtke, 1993, 1996) and simultaneously, they are referred to as cumulus convection. The scheme uses a fully prognostic approach where the time evolution of cloud water content and fractional cloud cover is determined by sources and sinks due to various processes. The cloud formation is connected with turbulence in the boundary layer and horizontal transport of cloud water from convective updrafts. Clouds can dissipate through turbulent mixing, adiabatic and diabatic heating, and depletion of cloud water by precipitation.

The Nogherotto scheme (Nogherotto et al., 2016), a relatively new microphysics parametrization is based on a multiple-phase cloud microphysics scheme used in IFS. There are five prognostic variables: water vapour, cloud liquid water, rain, cloud ice water and snow. Because cloud liquid and ice water are independent, a mixed-phase cloud is considered in general and super-cooling of cloud liquid water is allowed. At the end of each timestep, the conservation of enthalpy and total moisture is checked. The processes between the prognostic variables include: condensation, evaporation, autoconversion, collection, freezing, melting and deposition. Rain and snow are advected by the wind and sediment with a fixed, finite fall speed. The Wegener–Bergeron–Findeisen process follows Rotstayn et al. (2000).

Turbulence and other processes in the planetary boundary layer can be parametrized by one of two major schemes: the Holtslag scheme (Holtslag et al., 1990) or the UW-PBL (University of Washington – Planetary Boundary Layer) scheme (University of Washington; Bretherton et al., 2004). A drawback of the Holtslag scheme is the production of an excessive vertical transport of scalars (heat, moisture) and momentum in very stable conditions resulting in a poor simulation of near-surface temperature inversions and low level clouds. Hence, the implementation of the Holtslag scheme in the RegCM code is slightly different from the original paper. A problem tied to the excessive vertical transport is the lack of simulation of low level stratus clouds. To address this problem, the UW-PBL scheme has been developed. It is a 1.5 order local, down-gradient diffusion parametrization with prognostic turbulent kinetic energy calculated from the balance of buoyant production or destruction, shear production, vertical transport of dissipation, and horizontal diffusion and advection. The scheme also parametrizes the entrainment process and the production of turbulence by cloud-top radiative cooling.

Radiative transfer parametrization is based on the one found in the CCM3 (Community Climate Model, version 3) global model (Kiehl et al., 1996) and it in-

cludes calculations for the short-wave and long-wave parts of the electromagnetic spectrum, including both atmospheric gases and aerosols. A δ-Eddington approximation is used to handle short-wave radiative processes. Short-wave optical properties use prognostic cloud liquid and ice water, diagnostic cloud fractional cover which is a function of relative humidity, and effective cloud particle size. In the long-wave spectrum, cloud emissivity is computed as a function of cloud liquid or ice water path. Long-wave cloud absorption cross sections depend on effective particle size for the liquid and ice phases.

No special treatment is currently included in RegCM for orographic effects.

Land processes are parametrized by so-called land surface models. The default, older BATS (Biosphere–Atmosphere Transfer Scheme) model (Dickinson et al., 1993) can be replaced by the more advanced Community Land Model (CLM), version 4.5, which is developed by NCAR as part of the Community Climate System Model (CCSM), and then modified for the use in RegCM. It represents specific land processes, e.g. vegetation composition and structure; absorption, reflection and transmittance of short-wave radiation; absorption and emission of long-wave radiation; momentum, sensible heat (ground and canopy) and latent heat (ground and canopy) fluxes; heat transfer in soil and snow including phase change; canopy hydrology (interception, throughfall and drip); snow hydrology (accumulation, melting and water transfer between snow layers); soil hydrology (surface runoff, infiltration, redistribution of water within a column and groundwater); lake temperatures and fluxes; urban energy balance and climate. The model also solves the prognostic equation of surface temperature which is one of the inputs for the calculation of screen level temperature. CLM uses a tile approach to account for land surface complexity within a grid cell. Each grid cell is divided into three sub-grid levels. The first sub-grid level, a land unit, contains up to five different land cover types (vegetated, lake, urban, glacier or crop). The second, a column, contains data about urban area surfaces (roof, sun or shade wall and pervious or impervious), the irrigation state of crops (irrigated or unirrigated) and variability in the soil and snow state variables. The third, a plant functional type (PFT), captures the biogeophysical and biogeochemical differences between broad categories of plants. On the vegetated land unit, up to 16 possible PFTs may coexist. Hydrological and energy balance equations are solved on these sub-grid levels and then aggregated back to the grid-cell level (Oleson et al., 2013). This way of dividing the grid cell allows to capture the grid cell heterogeneity and thus gives more realistic values from hydrological and energy balance equations and fluxes when using coarser resolutions. To resolve the meteorological phenomena specific to urban areas (like the urban heat island), the Community Land Model Urban (CLMU) canopy module is implemented inside CLM4.5 (Oleson et al., 2008).

1.4 Verification and diagnostic tools

The performance of **ALADIN** is regularly statistically assessed with respect to observations. They consist of surface synoptic and upper-air measurements available via the international exchange of observations. For this purpose, the verification package VERAL (Verification of ALADIN) can be used (Janoušek, 1999). First, the CANARI (fr. *Code d'Analyse Nécessaire à Arpege pour ses Re-*

	ALADIN	RegCM
Deep convection	3MT	Tiedtke (1993, 1996)
Microphysics	3MT	Nogherotto et al. (2016)
Orographic effects	Catry (2006)	*no special treatment*
Radiation	ACRANEB2	CCM3
Shallow convection	TOUCANS	Holtslag et al. (1990) or UW-PBL
Surface	ISBA	BATS or CLM
Turbulence	TOUCANS	Holtslag et al. (1990) or UW-PBL

Table 1.1: Overview of important parametrizations used in ALADIN and RegCM. Some schemes are referred to using an author name, so the relevant papers are shown.

jets et son Initialisation, transl. Code for the Analysis Necessary for ARPEGE for Its Rejects and Its Initialization) configuration (Taillefer, 2002) of ALADIN is applied for the quality control of observations and a calculation of forecast departures from the actual observations at the observation locations. Then, the departures are used to produce standard deviation, mean error and root mean square error of surface and upper-air variables averaged over the verification domain. Moreover, there is an extension of VERAL for precipitation accumulated in 6 and 24 hours which are assessed using contingency tables, constructed from predefined thresholds, and additional scores.

One of the diagnostic tools used in the development of ALADIN is the DDH tool (fr. *Diagnostics par Domaines Horizontaux*, transl. Diagnostics on Horizontal Domains). It provides the budged of prognostic variables (momentum, temperature, water vapour, etc.) split to contributions from different processes on user defined domains such as zonal bands, limited domains or isolated points. Is is an important tool used by researchers to understand dynamical and physical interactions in the model and to develop parametrizations. Moreover, there are countless custom-made tools used for specific purposes, e.g for basic visualization of vertical profiles or time evolution of domain averaged variables.

Because **RegCM** has a large, centrally uncoordinated community and it is used for a variety of studies, a specific tool for verification of model outputs is not, of course, developed. In the community, the verification process is often referred to as the validation. For this purpose, one can use more general tools, such as CDO (Climate Data Operator), GrADS (Grid Analysis and Display System) or NCL (NCAR Command Language) which can efficiently manipulate model data, perform data analysis and visualize the results. For the purpose of verification, gridded observations such as E-OBS (European temperature and precipitation) dataset (Cornes et al., 2018), reanalyses such as ERA5 (ECMWF Reanalysis, version 5) or individual measurements such as ECA (European Climate Assessment) dataset (Klein Tank et al., 2002) are used as the best estimates of the real atmospheric state. Similar to ALADIN, it is necessary to create custom-made tools for unique tasks.

2. Influence of selected parametrizations on temperature

In this chapter, we will cover how changes in selected parametrization schemes introduced in the operational version of ALADIN affect the modelled temperature. We will describe relevant parametrizations in more detail, introduce the reference experiments (or shortly "references") and additional experiments with changed parameters that will be compared to the references. But first, a description of the model domain and the configuration which will remain the same through all experiments is provided.

Since March 2019, CHMI has been running the operational version of ALADIN with the high horizontal resolution of 2.3 km and with non-hydrostatic dynamics. This configuration supersedes the older operational version which used the horizontal resolution of 4.7 km and hydrostatic dynamics (Brožková et al., 2019).

Fig. 2.1 shows the ALADIN/CHMI model domain with orography on which all experiments are computed. Besides the high horizontal resolution of 2.3 km, the model uses 87 vertical levels. The domain projection is a Lambert conformal projection with the tangent reference latitude and longitude of 46.2°N and 17.0°E, respectively.

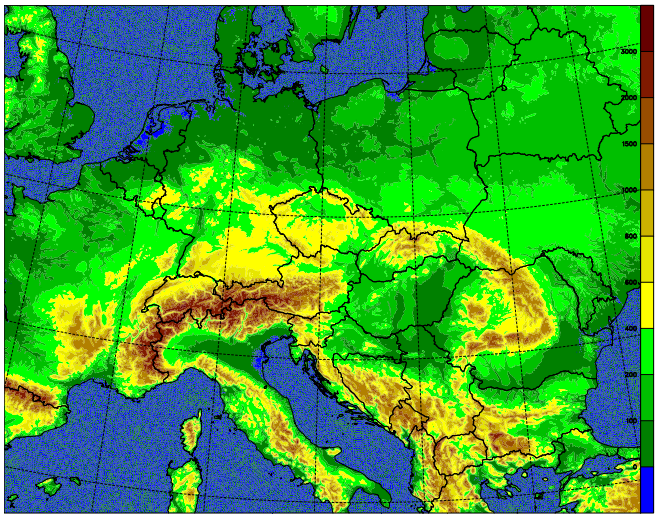

Figure 2.1: The ALADIN/CHMI model domain with the resolved orography (in meters) used for all experiments.

A vertical mass-based terrain-following hybrid coordinate η is used. In the non-hydrostatic version of ALADIN, it is based on the hydrostatic pressure denoted by π (Laprise, 1992). The vertical grid is staggered to gain the second order precision for vertical operators. The model level numbers are decreasing with an increasing height. Full levels are numbered from 1 to $L = 87$ which is the lowest full model level, half levels are numbered from $\tilde{0}$ to $\tilde{L} = 87$ corresponding to surface. The average distance between the surface and the lowest full model level is 9.7 m. Physical quantities treated by the parametrizations are associated with full model levels, unless stated otherwise. A quantity associated with specific level (for example a level l) will have this level specified in the lower index.

If the quantity is associated with the surface, the symbol s will be noted in the lower index instead of $\tilde{L}$. The physical quantities represent a gridbox average, if not stated otherwise, such as mentioning perturbations, subgrid-scale processes, etc.

In Table 2.1, there is an overview of full model levels in ALADIN with their corresponding pressure and height above the ground according to the International Standard Atmosphere (ISA). When mentioning model level numbers later in the text, we will also give the reader the corresponding rounded pressure from this table.

Model level	Pressure (hPa)	Height (m)
1	0.5	53 528
5	25	25 057
10	79	17 702
15	148	13 700
20	229	10 923
25	321	8716
30	415	6925
35	496	5630
40	568	4624
45	634	3786
50	696	3058
55	755	2414
60	811	1836
65	866	1303
70	915	853
75	955	498
80	986	233
85	1007	56
87	1012	10

Table 2.1: Full model levels in ALADIN and their corresponding pressure (in hPa) and height above the surface (in meters) according to the International Standard Atmosphere (ISA).

The budget from the DDH tool is computed on a λ-$\sin\phi$ polygon where λ and ϕ are longitude and latitude, respectively. In our case (the polygon is specified by two corners), it is a longitude-latitude rectangle which will be called a "DDH domain" to distinguish it from the model domain. That also means the budget is domain averaged. In the following experiments, the budget provided by DDH is typically computed for the next 24 hours to eliminate diurnal variations of prognostic variables if not stated otherwise.

Vertical profiles and temporal evolution graphs are computed on a rectangle in a Lambert conformal projection as domain averages. The rectangle will be called a "diagnostic domain". Verification is done on a longitude-latitude rectangle with the left bottom corner at (40°N, 2°E) and the right upper corner at (55.6°N, 29°E) and this rectangle will be called a "verification domain". To maintain readability, we will often omit the term "domain averaged" if it would have been repeated

several times in a paragraph.

Fig. 2.2 shows a scheme of the surface-atmosphere interface where the soil is divided into the surface soil layer and the deep soil layer. Surface fluxes are between the atmosphere and the surface soil layer, the soil heat flux is between the surface soil layer and the deep soil layer. A convention is that the net surface fluxes are positive downwards (towards the surface) and the soil heat flux is positive upwards (also towards the surface). The energy budget of the surface soil layer (shortly the surface energy budget) is the sum of the surface fluxes and the soil heat flux. When describing a change of a flux between experiments, we will always mean its absolute value if not stated otherwise.

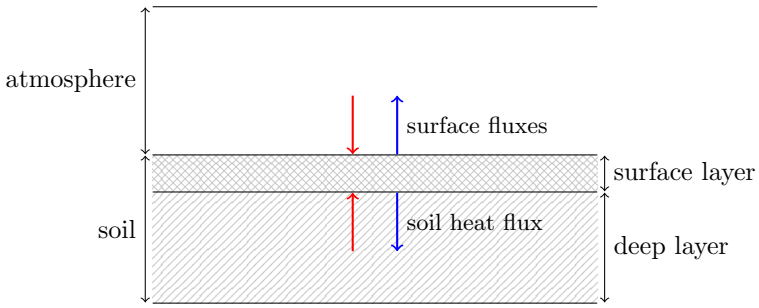

Figure 2.2: Scheme of the surface-atmosphere interface with associated fluxes. Red color indicates fluxes which add energy to the surface soil layer; blue color indicates fluxes which remove energy from the surface soil layer.

To evaluate the performance of ALADIN, the forecasted meteorological parameters are compared to observations and several statistical scores are computed using the verification package VERAL (Janoušek, 1999). Three main statistical scores are:

$$\mathrm{BIAS} = \frac{1}{N}\sum_{i=1}^{N}(F_i - O_i) \ , \tag{2.1}$$

$$\mathrm{RMSE} = \sqrt{\frac{1}{N}\sum_{i=1}^{N}(F_i - O_i)^2} \ , \tag{2.2}$$

$$\mathrm{STDE} = \sqrt{\mathrm{RMSE}^2 - \mathrm{BIAS}^2} \ , \tag{2.3}$$

where BIAS denotes mean error, RMSE denotes root mean squared error, STDE denotes standard deviation, N is the number of observations, O_i is the i-th observation and F_i is the i-th forecasted parameter in the observation space.

2.1 Low cloudiness case

In the current operational physical package ALARO 1 – Version B, there is a difference between cloud cover and cloud water used in the microphysics scheme and in the radiation scheme. Cloud water q_c is defined as the sum of cloud liquid water q_l and cloud ice water q_i. If there is a need to get cloud liquid water q_l

and cloud ice water q_i from cloud water q_c, the split is computed by the routine FONICE according to temperature, but it is not a binary split.

As the horizontal resolution of ALADIN is getting finer, the terms "stratiform" and "convective" can be no longer applied to distinguish between grid-scale and subgrid-scale cloudiness, respectively, because the convection is currently partially resolved and not just parametrized. However, we will use both terms "stratiform" and "convective" throughout the text, but they will strictly denote the grid-scale and the subgrid-scale level, respectively.

Fig. 2.3 illustrates a diagram of radiation and microphysics routines in ALADIN on which we will demonstrate the difference between cloud cover and cloud water for microphysics and for radiation. One of input parameters for both schemes is so-called total moisture q_{tot} which is the sum of specific humidity q_v, cloud liquid water q_l and cloud ice water q_i. Another input parameter for both schemes is the critical relative humidity $\mathrm{RH}_{\mathrm{crit}}$ which is responsible for possible stratiform condensation even when relative humidity for a gridbox is less than 100 % because the condensation can happen due to subgrid-scale variability. The critical relative humidity $\mathrm{RH}_{\mathrm{crit}}$ is dependent on height, i.e. it has some vertical profile. Note that both radiation and microphysics use different vertical profiles of critical relative humidity $\mathrm{RH}_{\mathrm{crit}}$.

Let us describe the relevant radiation routines first. Both total moisture q_{tot} and critical relative humidity profile are going into the ACNEBN routine. Total moisture q_{tot} is used to diagnose the stratiform cloud water for radiation $q_{c,s}^{\mathrm{rad}}$ while including a parametrization of shallow convection (see Section 2.1.1.2) and inversion clouds (see Section 2.1.1.3). Then, using the Xu-Randall scheme (Xu and Randall, 1996), the stratiform cloud water for radiation $q_{c,s}^{\mathrm{rad}}$ is converted to stratiform cloud cover for radiation n_s^{rad} (see Section 2.1.1.1). Another input going into the ACNEBN routine is deep convection cloud cover n_{cv} from a previous time step (denoted by $t - \Delta t$ in Fig. 2.3) which is supplied from the routine ACCVUD. The value from the previous time step is used because the routine ACCVUD will be called only after the ACNEBN routine in the current time step. The deep convection cloud cover n_{cv} is the sum of an updraft area fraction and a detrainment area fraction. To produce cloud cover for radiation n^{rad}, both stratiform cloud cover for radiation n_s^{rad} and deep convection cloud cover n_{cv} are combined together while assuming a random overlap hypothesis in a gridbox. The last three variables are part of the routine output and together are called "diagnostic cloudiness" because they are determined from other prognostic quantities.

Now, we will describe the relevant microphysics routines. Both total moisture q_{tot} and the vertical profile of critical relative humidity $\mathrm{RH}_{\mathrm{crit}}$ are going into the ACNEBCOND routine which applies thermodynamic adjustment as described in Chapter 1 for the 3MT scheme. It then computes stratiform condensation and evaporation fluxes for cloud liquid water P_l and cloud ice water P_i, and also stratiform cloud cover n_s by a bit different method compared to the one in the ACNEBN routine but also based on the Xu-Randall scheme. Next, the ACCVUD routine is called which computes updrafts and subgrid-scale convective condensation fluxes for cloud liquid water $P_{l,cv}$ and cloud ice water $P_{i,cv}$, and also deep convection cloud cover n_{cv}. Next, the ACUPU routine combines the outputs from the ACNEBCOND routine and the ACCVUD routine to produce

cloud cover n while assuming a random overlap hypothesis in a gridbox. Cloud cover n is then an input to the APLMPHYS routine which solves microphysics. The microphysics in ALADIN can be understood as a scheme for precipitating processes. Precipitation and evaporation fluxes computed by microphysics provide the closure to compute downdrafts in the ACMODO routine. Then, the ACMODO routine treats downdrafts and yields additional subgrid-scale evaporation fluxes of precipitation within downdrafts. Finally, the ACUPD routine finalizes sedimentation of precipitation linked to the evaporation in downdrafts. Note that there is no shallow convection in the microphysics scheme. Because microphysics routines use prognostic equations to determine the cloud water, it is called "prognostic cloudiness".

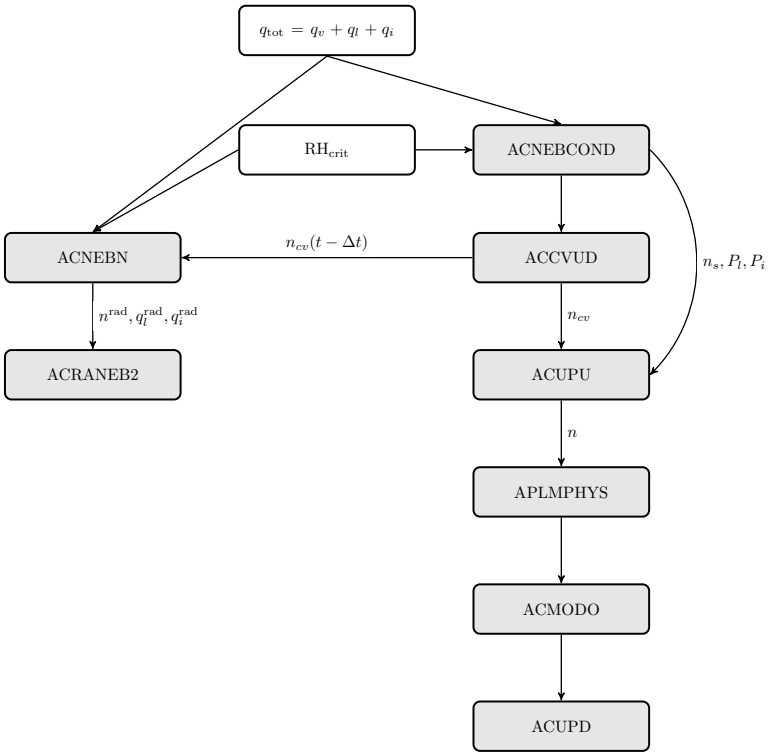

Figure 2.3: Scheme of important radiation and microphysics routines in ALADIN that are relevant to cloud cover and cloud water. Blocks with a gray background are used for routines and blocks with a white background indicate input parameters.

A long-term goal is to use both cloud water from microphysics and convective (deep and shallow) cloud water from the turbulent scheme TOUCANS in the radiation scheme. In that case, the diagnostics of cloud water in radiation would be no longer necessary and associated tuning parameters could be removed. One of the first steps is thus to unify the vertical profiles of the critical relative humidity for radiation and microphysics. We will do an experiment with such unified profile in Section 2.1.3.

In the next sub-sections, we will describe the computation of stratiform cloud cover in radiation using the Xu-Randall scheme (Xu and Randall, 1996) and additional parametrizations that were created later to modify the stratiform cloud

water, mainly the correction of saturation specific humidity in an inversion and the parametrization of shallow convection.

In the following text, we will deal only with parameters in radiation, so we will not further mention the parameters associated with microphysics if not stated otherwise. Therefore, we will not longer use the abbreviation "rad" in the upper index, e.g. for cloud cover or cloud water.

2.1.1 Relevant parametrizations

2.1.1.1 Xu-Randall scheme

The Xu-Randall scheme (Xu and Randall, 1996) is a basic method used to diagnose the stratiform cloud cover. The following description is valid for the computation of stratiform cloud cover for radiation (the ACNEBN routine). The Xu-Randall scheme uses stratiform cloud water q_s (see the equation (2.10)) and relative humidity r. Thus, the stratiform cloud cover is given by the Xu-Randall scheme as

$$n_s = r^p \left[1 - \exp\left(- \frac{\alpha \, q_s}{[(1-r) \, q_{\text{sat}}]^{\delta}} \right) \right] \tag{2.4}$$

where $p = 0.25$, α and δ are tuning parameters with default values given in the Table 2.2, and q_{sat} is the saturation specific humidity.

In ALADIN, one can also activate the scaling of relative humidity via the key LQXRTGH. The re-scaled relative humidity is computed as

$$r' = [\tanh(r^{\gamma})]^{\frac{1}{\gamma}} \tag{2.5}$$

and goes into the equation (2.4) instead of relative humidity r. A tuning parameter γ is used with a default value given in the Table 2.2. For the re-scaled relative humidity r', it applies that $0 \leq r' < 1$. Therefore, it is not possible to completely cover a single layer by clouds. Maximum sensitivity to the value of the parameter γ occurs close to the saturation ($r \approx 1$) (Mašek, 2008).

Parameter	Value	Units
α (QXRAL)	150	1
γ (QXRTGH)	2	1
δ (QXRDEL)	0.5	1

Table 2.2: Tuning parameters used in the Xu-Randall scheme.

2.1.1.2 Stratiform cloud water

The calculation of stratiform cloud water for radiation is based on the description of the ACNEBN routine (Gerard, 2018). First, the saturation excess is expressed as

$$\Delta q_{\text{exc}} = \langle q \rangle - r_{\text{crit}} \, q_{\text{sat}} \tag{2.6}$$

where r_{crit} is the vertical profile of the critical relative humidity and q_{sat} is the saturation specific humidity. The value of $\langle q \rangle$ is determined as the average of total moisture q_{tot} over all connected unstable layers below the current one, but maximally to a layer where the difference between the static energy of that layer and the current layer is below the tuning parameter QSSC with a default value of $400\,\text{m}^2\,\text{s}^{-2}$. This approach is used to parametrize shallow convection.

The next step is to re-scale the moisture excess to a new variable (without physical meaning) as

$$q'_s = \alpha'_s \Delta q_{\text{exc}} \tag{2.7}$$

where the parameter α'_s is computed as

$$\alpha'_s = \frac{\alpha_s}{\sqrt{1 + (\alpha'_v\, q_{\text{sat}})^2}} \tag{2.8}$$

where α_s is a tuning parameter with the value given in the Table 2.3 and the parameter α'_v is expressed as

$$\alpha'_v = \alpha_v \left[1 + (\text{QSMODC} - 1)\,(1 - \eta)\right] \tag{2.9}$$

where η is the vertical coordinate at full levels, and α_v and QSMODC are tuning parameters with values given in the Table 2.3.

The scaling factor α'_s of the moisture excess depends on the parameter α_s; it decreases with an increasing saturation specific humidity. The value of the parameter α'_v is linearly increasing due to decreasing η, from the surface value α_v up to the value of $\alpha_v \cdot \text{QSMODC}$. In our case, α'_v is in the range from 250 to 1000. The reason for the height modulation of the parameter α'_v is the necessity to reduce medium and high clouds.

Finally, stratiform cloud water is determined as

$$q_s = l_{\max}\left[1 - \exp\left(-\frac{q'_s}{l_{\max}}\right)\right] \tag{2.10}$$

where $l_{\max}$ is a tuning parameter which specifies the maximum of q_s and its value is given in the Table 2.3.

Parameter	Value	Units
α_s (QSSUSS)	0.4	1
α_v (QSSUSV)	250	1
$l_{\max}$ (QSUSXS)	3×10^{-4}	kg/kg
QSMODC	4	1

Table 2.3: Tuning parameters used in the calculation of stratiform cloud water.

2.1.1.3 Correction of saturation specific humidity

The saturation specific humidity can be approximated by

$$q_{\text{sat}} \approx \frac{R_d}{R_v}\frac{E(T)}{p} \tag{2.11}$$

where R_d is the gas constant for dry air, R_v is the gas constant for water vapour, $E(T)$ is the partial pressure of the saturated water vapour as a function of temperature and p is air pressure.

In the case of a temperature inversion, the mean temperature of a layer in the inversion is greater than the temperature at its base. Vertical motions are blocked by the inversion and the saturation specific humidity inducing condensation is overestimated, so it is not properly represented by the mean temperature. In this case, the mean temperature just below the inversion base should be used (Gerard, 2018).

Thus, a special treatment of low level inversion clouds has been added to ALADIN. To activate the treatment, an inversion layer needs to have a minimum thickness which can be tuned. Then, the temperature used in the equation (2.11) is lowered to decrease the saturation specific humidity to help the formation process of low level inversion clouds. The temperature shift itself is proportional to temperature gradient and it is expressed as

$$\Delta T = \mathrm{RPHI0} \cdot \frac{\partial T}{\partial \Phi} \tag{2.12}$$

where Φ is geopotential and RPHI0 is a tuning parameter with the default value of 1250 J/kg. Because the presence of clouds strengthens the inversion, the treatment creates a positive feedback loop (Brožková et al., 2006).

The cloud water for microphysics is not primarily affected, but can be influenced via a feedback loop because cloud cover for radiation has a considerable effect on temperature of cloud layers.

2.1.2 Reference experiment

This reference experiment is based on the CHMI version CY43T2_op2 of the model ALADIN. The vertical profile of the critical relative humidity for the stratiform cloud water for radiation is different than the one for the stratiform cloud water for microphysics. The reference is used as a baseline and the experiment with the unified critical relative humidity profiles (see Section 2.1.3) will be later compared to it.

To describe the feedback loops during a winter case, the start of the integration is chosen on 28th January 2017 at 0 UTC. The DDH domain has the left bottom corner (SW corner) at (47°N, 10°E) and the right upper corner (NE corner) at (52°N, 20°E). The diagnostic domain used for the vertical profiles and evolution graphs is the same as the DDH domain. The DDH and diagnostic domains are selected like this because of a strong cloudiness reduction as a consequence of the unification of the vertical profiles of the critical relative humidity, and because of an existence of a temperature inversion. That is shown in more detail in Section 2.1.3.

The influence of precipitation on feedback loops can be neglected on the selected domain, which is shown in Fig. 2.4. In Fig. 2.5, we can see that low cloudiness is occurring on the major part of the chosen domain.

Now, we will look at the surface energy budget and associated fluxes because their change will have a direct impact on the surface and near-surface temperature.

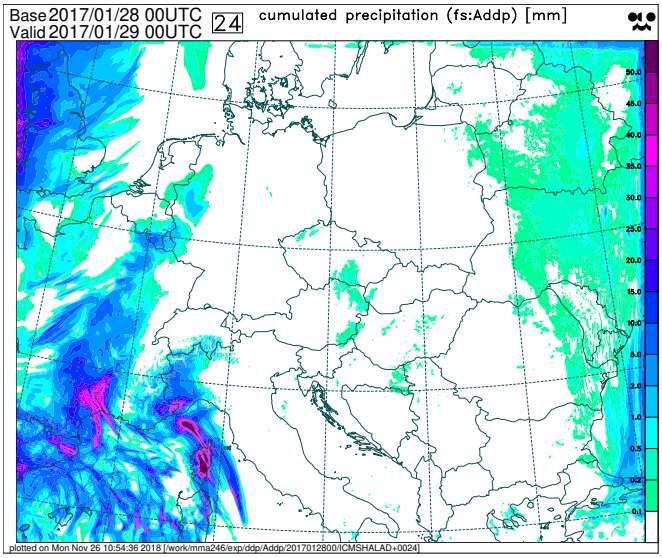

Figure 2.4: Precipitation accumulated in 24 hours (in mm) for the reference on 29.1.2017, 0 UTC. Integration starts on 28.1.2017, 0 UTC.

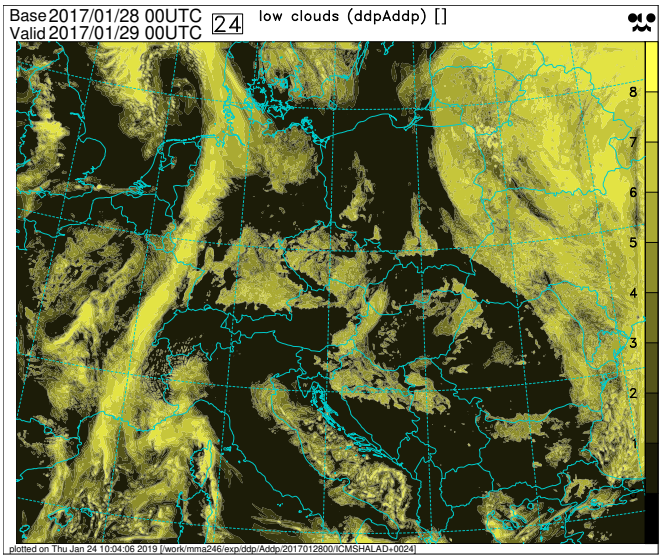

Figure 2.5: Low cloudiness (in oktas) for the reference on 29.1.2017, 0 UTC. Integration starts on 28.1.2017, 0 UTC.

Fig. 2.6 shows the evolution of the domain averaged surface energy budget and associated fluxes where the abbreviations LW and SW for radiation fluxes mean longwave and shortwave, respectively. The gain or the loss of energy of the surface soil layer will be hereafter called as the gain or the loss of energy of the surface. The surface longwave net radiation flux (red solid line) is negative which means that the surface is losing energy in thermal spectrum. The surface shortwave net radiation flux (yellow solid line) is positive during the day which means that the surface is gaining solar energy; and, of course, zero during the night. The surface sensible heat flux (light blue solid line) is positive during the night which means that the surface is gaining energy due to heat transfer from near-surface air layers that are cooling; and negative during the day which means

that the surface is losing energy to warm up near-surface air layers. The surface latent heat flux (dark blue solid line) is negative which means that the surface is losing energy by evaporation.

The total surface flux (green solid line) is the sum of the surface longwave net radiation flux, the surface shortwave net radiation flux, the surface sensible heat flux and the surface latent heat flux. The soil heat flux (brown dashed line) partially compensates the total surface flux and it is also phase-shifted from the total surface flux. The surface energy budget (black solid line) is the sum of the total surface flux and the soil heat flux.

The total surface energy balance is determined as the signed area under the surface energy budget line. After 24 hours, it is positive which means that the surface got warmer.

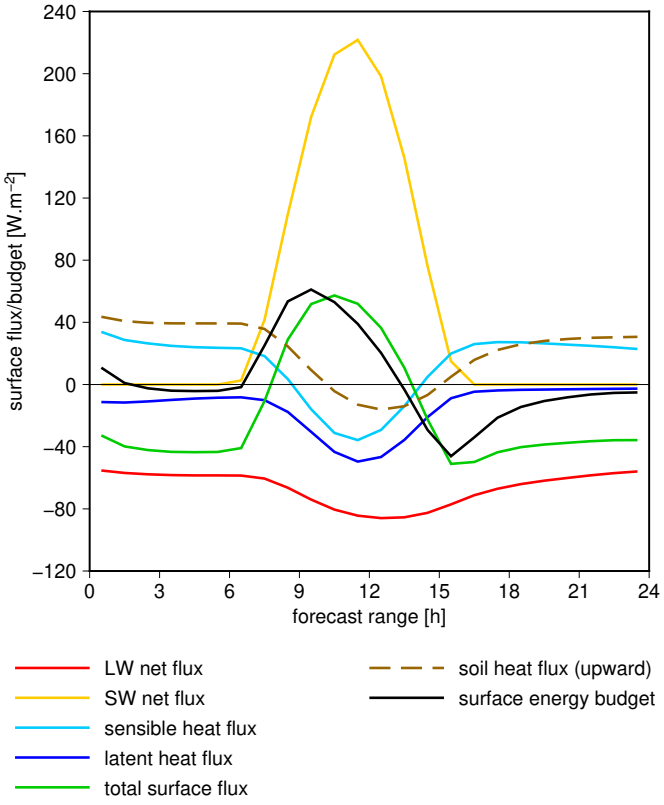

Figure 2.6: Evolution of domain averaged surface energy budget and associated fluxes (in W/m^2) for the reference. Integration starts on 28.1.2017, 0 UTC.

2.1.3 Experiment with unified critical relative humidity profiles

The main characteristic of this experiment is the unification of vertical critical relative humidity profiles for the stratiform cloud water in radiation and microphysics according to the one used in microphysics. Moreover, the computation of the average total moisture $\langle q \rangle$ in the equation (2.6) is slightly modified. We use the CHMI model version CY43T2_op2rhc.

There are the following changes in the model setup compared to the reference:

1. set LQXRTGH from .T. to .F. (no relative humidity scaling according to the equation (2.5)),
2. add LRHC_ADJ = .T. (the activation of the unified critical relative humidity profiles),
3. set QSSUSS from 0.4 to 0.8 (the enhancement of the stratiform cloud water in the equation (2.8)),
4. set QSSUSV (the parameter α_v) from 250 to 0 (the parameter α'_v is zero in the equation (2.9)),
5. set RPHI0 from 1250 to 0 (no correction of the saturation specific humidity is done).

Following differences are calculated between this experiment and the reference described in Section 2.1.2. When specifying model level numbers, we will also mention the corresponding rounded pressure from the Table 2.1.

In Fig. 2.7, the low cloud cover is shown. Comparing it to Fig. 2.5, the spatial extent of low clouds is reduced and cloud fraction had almost a binary behaviour (clear sky – overcast).

One can see in Fig. 2.8 the domain averaged vertical profile of cloud liquid water for radiation. When the value of RPHI0 is set to 0, the consequence is a strong reduction of cloud liquid water for radiation at model levels 70 (approx. 920 hPa) and more and a small reduction in absolute value at model levels 45–50 (approx. 630–700 hPa), but the relative reduction is huge because there is almost no cloud liquid water. Together with a reduction in cloud ice water for radiation (not shown), it means a reduction of cloud water for radiation.

In Fig. 2.9, the domain averaged vertical profile of cloud liquid water for microphysics is shown. It can be seen that the cloud liquid water for microphysics is reduced at model levels 40–55 (approx. 570–760 hPa) and 60–86 (810–1010 hPa) which are similar levels as those for the cloud liquid water for radiation in Fig. 2.8. This is the only time we present a quantity related solely to microphysics to demonstrate a secondary effect on cloud water for microphysics because the cloud water for radiation has a considerable effect on temperature of involved cloud layers as mentioned in Section 2.1.1.3.

2.1.4 Feedback loops

Individual feedback paths that are relevant in the studied case are illustrated by the diagram in Fig. 2.10. The feedback paths will be further described in more detail.

Path 1, 2 The domain averaged surface downward shortwave radiation flux accumulated in 24 hours is increased by 5.4 % due to a decrease in low and high cloudiness. That can be seen in Fig. 2.11 which shows the domain averaged cloud fraction for radiation. The reduction in cloudiness happens for all levels which had clouds in the reference. The high cloudiness was at model levels 17–40 (approx. 180–570 hPa) in the reference and now it is mostly at model levels 18–25 (approx. 200–320 hPa). The low cloudiness is at model levels 70 (approx. 920 hPa) and more but extremely reduced. The reduction is the result of the aforementioned changes in the model setup compared to the reference.

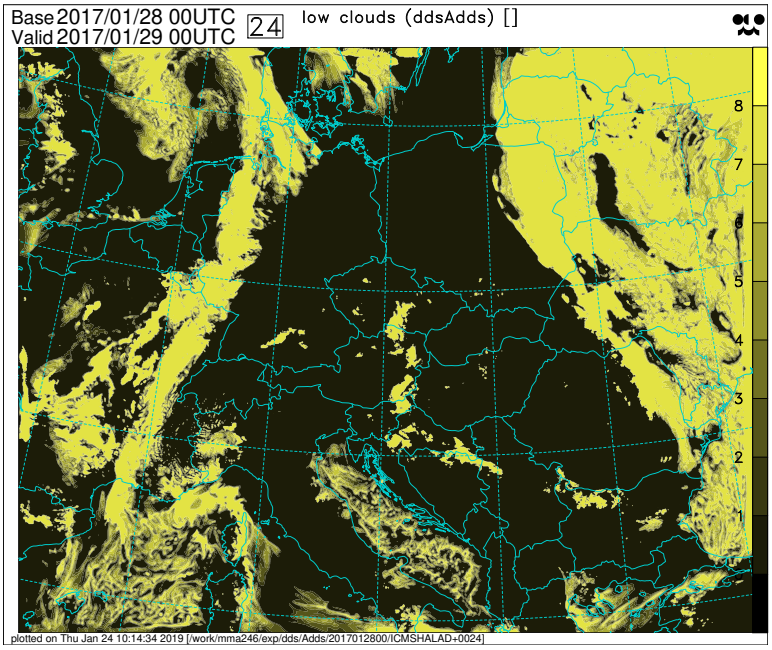

Figure 2.7: Low cloudiness (in oktas) for the experiment with unified critical relative humidity profiles on 29.1.2017, 0 UTC. Integration starts on 28.1.2017, 0 UTC.

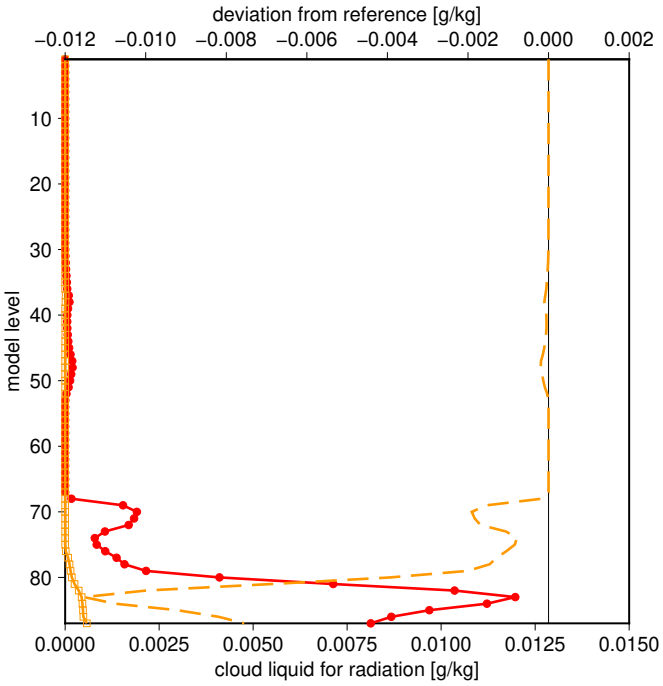

Figure 2.8: Vertical profiles of domain averaged cloud liquid water for radiation (in g/kg) for the experiment with unified critical relative humidity profiles (orange), the reference (red) and their difference (dashed) on 29.1.2017, 0 UTC. Integration starts on 28.1.2017, 0 UTC. The image contains two scales. The lower scale is for reference and experiment values, and the upper scale is for their difference.

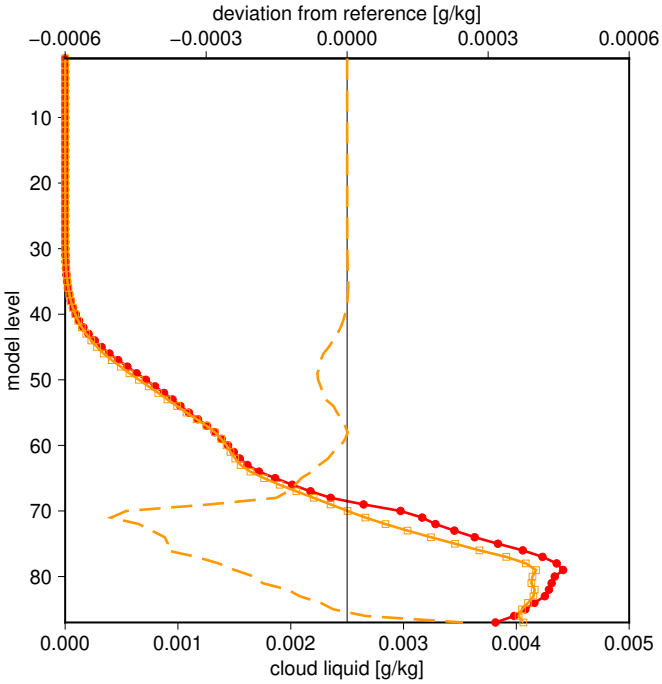

Figure 2.9: Vertical profiles of domain averaged cloud liquid water for microphysics (in g/kg) for the experiment with unified critical relative humidity profiles (orange), the reference (red) and their difference (dashed) on 29.1.2017, 0 UTC. Integration starts on 28.1.2017, 0 UTC. The image contains two scales. The lower scale is for reference and experiment values, and the upper scale is for their difference.

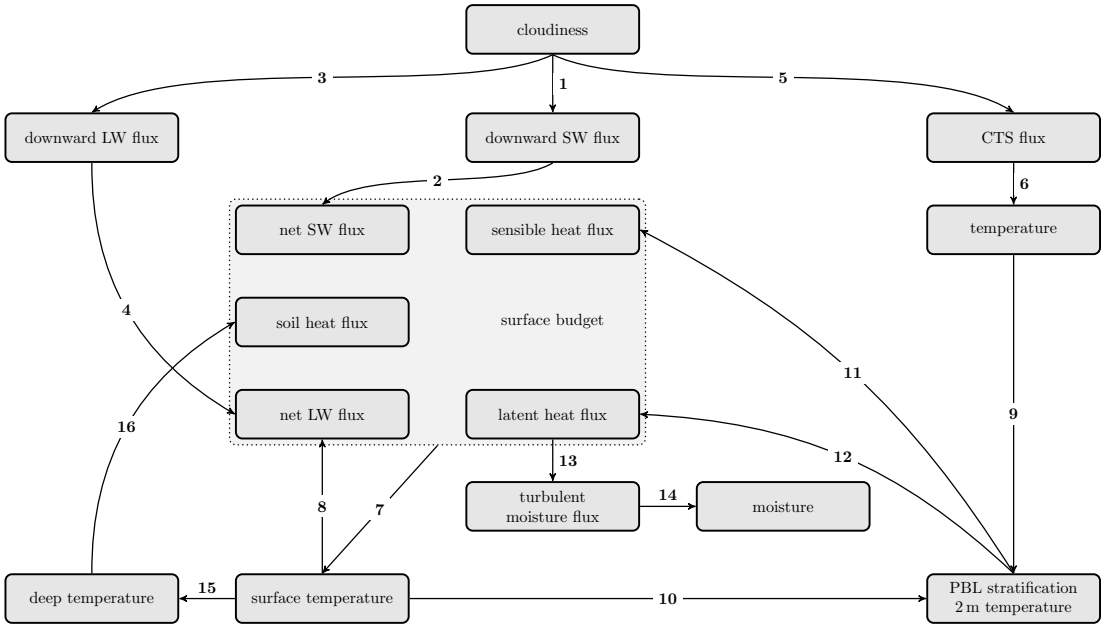

Figure 2.10: Diagram of feedback loops with numbered paths for the experiment with unified critical relative humidity profiles.

Fig. 2.12 shows the evolution of domain averaged surface energy budget for the difference between the experiment and the reference. A consequence of the surface downward shortwave radiation flux increase is the increase in the surface shortwave net radiation flux up to $7\,\mathrm{W/m^2}$ at 12 UTC. We will neglect the changes, if any, of the surface albedo between both experiments in the interpretation of results. As a result, the surface gains more energy from the shortwave radiation during the day.

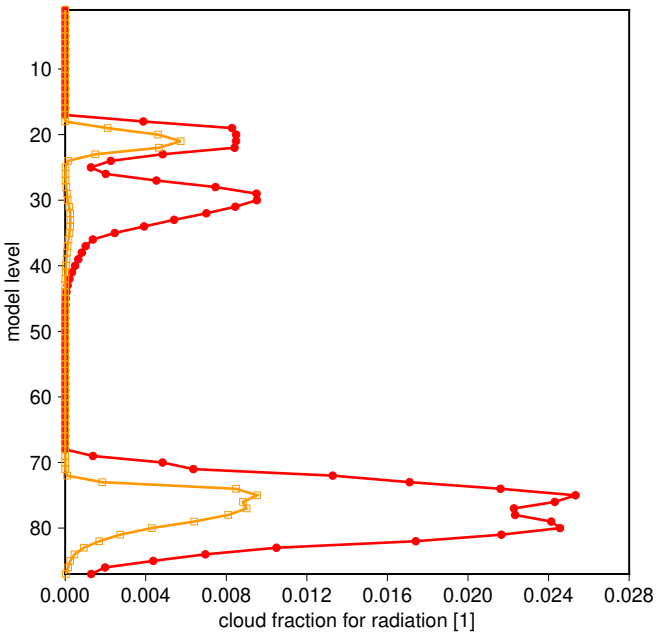

Figure 2.11: Vertical profiles of domain averaged cloud fraction for radiation (dimensionless) for the experiment with unified critical relative humidity profiles (orange) and the reference (red) on 28.1.2017, 12 UTC. Integration starts on 28.1.2017, 0 UTC.

Path 3, 4 The domain averaged surface downward longwave radiation flux accumulated in 24 hours is decreased by 5.5 %. This change is the result of the decrease in cloudiness as was presented in Fig. 2.11 which means there are less clouds to emit longwave radiation back to the surface. The most influence on the surface downward longwave radiation flux reduction bears the reduction of low cloudiness because the emitted longwave radiation by clouds depends on the fourth power of the cloud temperature as described by the Stefan–Boltzmann law.

Fig. 2.13 shows vertical profiles of the domain averaged temperature for the experiment and the reference. The temperature profile at 12 UTC has the same characteristics as the one at 24 UTC, so we will omit the former. It can be seen that temperature is higher for low-level clouds than for high-level clouds as expected. When considering only the temperature change between the high-level clouds at model levels 20–30 (approx. 230–420 hPa) and the low-level clouds at model levels 70 (approx. 920 hPa) and more, the low clouds emits 2.2x more

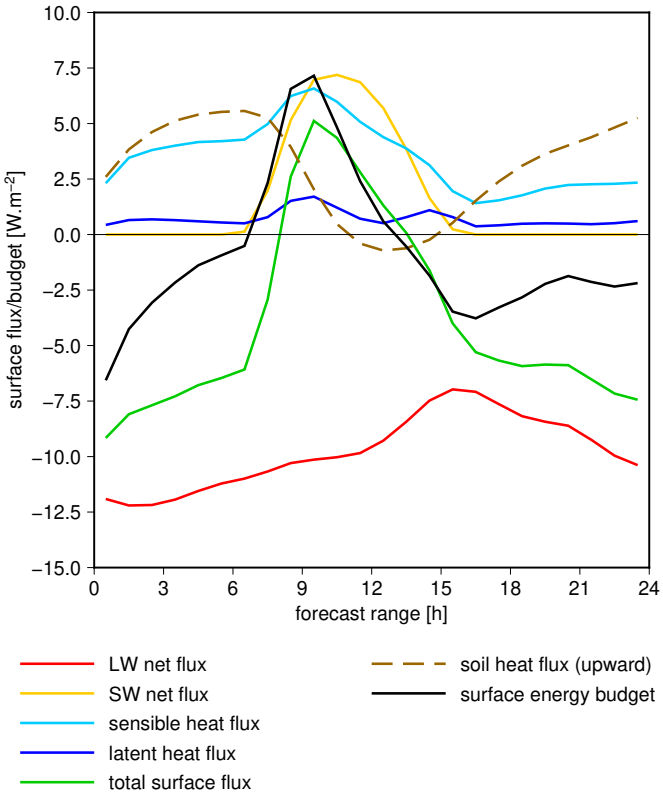

Figure 2.12: Evolution of domain averaged surface energy budget and associated fluxes (in W/m^2) for the difference between the experiment with unified critical relative humidity profiles and the reference. Integration starts on 28.1.2017, 0 UTC.

longwave radiation than the high clouds as follows from the Stefan–Boltzmann law. Additional information can be found in Path 5 and 6.

The increase of the absolute value of the surface net longwave radiation flux, as can be seen in Fig. 2.12, is mainly caused by the decrease of the surface downward longwave radiation flux. Hence, the surface is losing more energy by the longwave radiation during all day.

Path 5 The cloudiness reduction has a direct impact on longwave radiation emitted by clouds. To illustrate this effect, we use the ACRANEB2 single column model (SCM) which solves the radiative transfer in the atmosphere. The input is a vertical profile that is obtained as the domain average of the vertical profiles at 12 UTC. The output is a vertical profile of thermal heating rate obtained from this domain averaged input profile. For simplicity, the vertical profile of ozone, which has a little effect in the troposphere, is not used in the calculation.

In Fig. 2.11, we saw the reduction of high-level and low-level cloudiness. The cloud fraction for radiation has a significant impact on thermal heating rate. The larger the cloud fraction for radiation, the more clouds emit radiation in the longwave spectrum.

The vertical profile of the thermal heating rate is presented in Fig. 2.14. The cooling is the most significant at pressure levels near 900 hPa which correspond

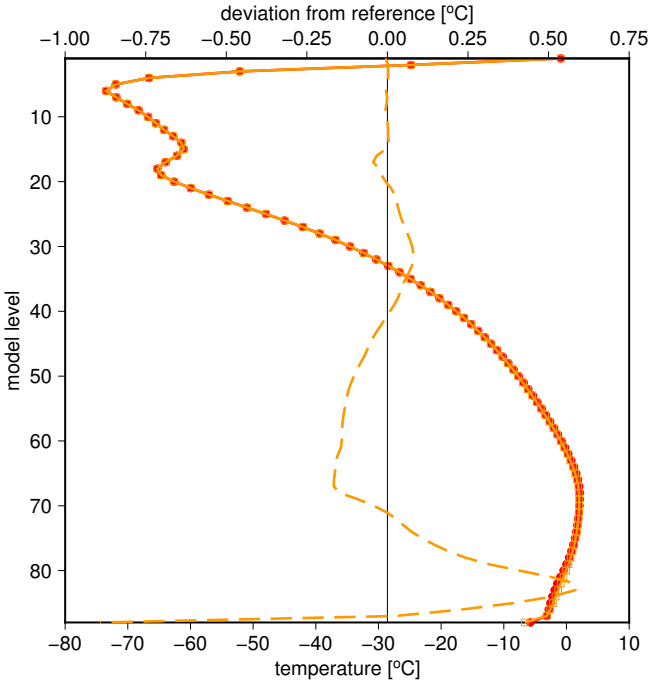

Figure 2.13: Vertical profiles of domain averaged temperature (in °C) for the experiment with unified critical relative humidity profiles (orange), the reference (red) and their difference (dashed) on 29.1.2017, 0 UTC. Integration starts on 28.1.2017, 0 UTC. The lowest model level corresponds to the surface. The image contains two scales. The lower scale is for reference and experiment values, and the upper scale is for their difference.

roughly to the low clouds tops at model levels near 70 in Fig. 2.11. Due to the low cloudiness reduction in the experiment, the absolute value of the thermal heating rate is less up to 0.6 K/day. As we discussed before (in Path 3 and 4), the reduction of the thermal heating rate at pressure levels near 400 hPa, which correspond roughly to model levels 25–30 in Fig. 2.11, is negligible due to low temperature of clouds compared to clouds at pressure levels near 900 hPa.

Fig. 2.15 shows the vertical profile of the cooling-to-space (CTS) heating rate which is a part of the thermal heating rate and gives the heating rate due to the longwave radiation going to space. When looking at the difference between the experiment and the reference (dashed) in Fig. 2.14 and 2.15, it can be seen that the CTS heating rate is largely responsible for the difference in thermal heating rates. That means the longwave radiation emitted by a cloud top to space stands for the cooling of levels with cloud tops. Once the cloudiness is reduced, those levels get warmer as can be seen in Fig. 2.13.

Path 6 The reduction in longwave cooling as presented in Fig. 2.14 has an impact on the heating of the atmosphere, mainly on the heating of the planetary boundary layer (PBL) which was presented in Fig. 2.13. The temperature inversion at model levels 70 (approx. 920 hPa) and more (where PBL is located) is now warmer up to 0.6 K. However, there is a cooling up to 0.2 K at model levels

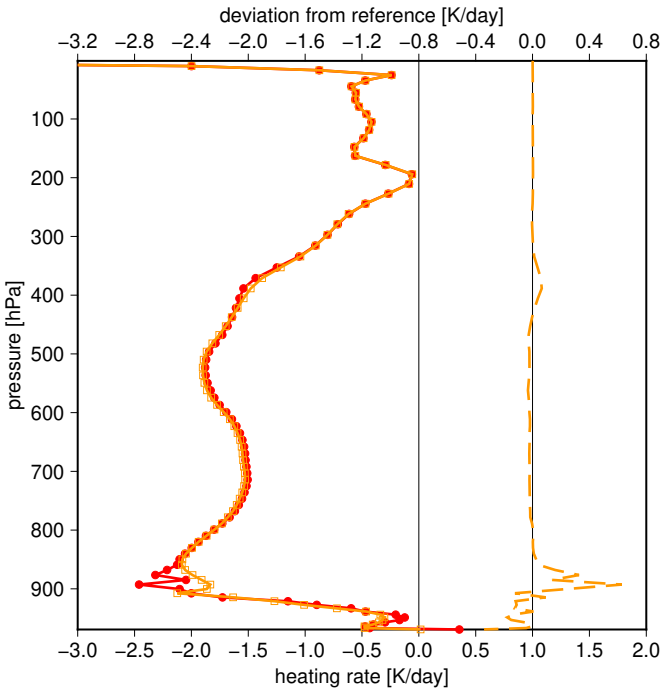

Figure 2.14: Vertical profiles of thermal heating rate (in K/day) for the experiment with unified critical relative humidity profiles (orange), the reference (red) and their difference (dashed) calculated on averaged inputs from 28.1.2017, 12 UTC. The image contains two scales. The lower scale is for reference and experiment values, and the upper scale is for their difference.

40–70 (approx. 570–920 hPa).

We will use the DDH tool to confirm that the longwave radiation is responsible for the change in temperature. The difference of domain averaged temperature budget between the experiment and the reference is shown in Fig. 2.16. The aforementioned changes in the vertical profile of temperature can be seen in the gray colour because DDH is computed for the next 24 hours and the vertical profile is given at 24 UTC. For pressure levels 900 hPa and less which correspond roughly to model levels 70 and less in Fig. 2.13, the change in temperature is caused solely by advection (red). However, we can see three processes in total that influence the temperature budget. The first is advection (red) which is partially compensated by turbulence (light blue) at pressure levels 950 hPa and more. The third is the longwave radiation flux (black) which is partially compensated by advection (red) at pressure levels 850–950 hPa.

To finalize the description of this path, note that there is a qualitatively agreement between the longwave radiation (black) in Fig. 2.16 and the computed thermal heating rate (dashed) in Fig. 2.14. However, details are different due to the changed order of radiative calculations and averaging.

Path 7 The surface energy budget has a direct impact on the surface temperature. Both the evolution of domain averaged surface energy budget for the reference in Fig. 2.6 and the difference between the experiment and the reference

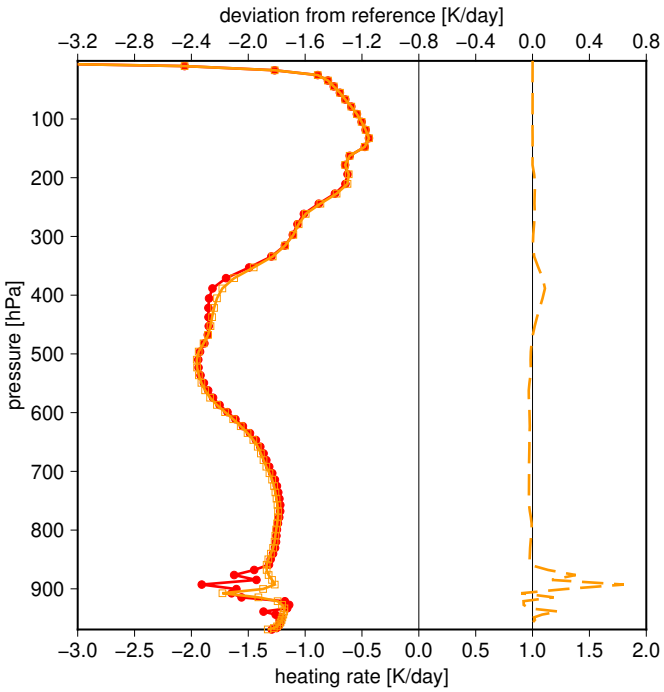

Figure 2.15: Vertical profiles of cooling-to-space heating rate (in K/day) for the experiment with unified critical relative humidity profiles (orange), the reference (red) and their difference (dashed) calculated on averaged inputs from 28.1.2017, 12 UTC. The image contains two scales. The lower scale is for reference and experiment values, and the upper scale is for their difference.

in Fig. 2.12 were presented. When comparing them, it can be seen that the surface energy budget for the experiment accumulated in 24 hours is positive but less than the one for the reference.

The result can be seen in Fig. 2.17 which shows the evolution of domain averaged surface temperature. The conclusion drawn about the surface energy budget can be confirmed by this figure. The surface temperature is indeed higher at 24 UTC than at 0 UTC and moreover, the surface temperature in the experiment compared to the reference is less up to 0.9 K.

Two significant drops in the surface temperature difference occurs. The first shows a maximum at 7 UTC and the second shows a maximum at 24 UTC, both of them up to 0.9 K. When looking at the surface budget for the reference in Fig. 2.6 and the difference in the surface budgets in Fig. 2.12, both drops can be explained by the change in the surface longwave net radiation flux. The surface temperature differs little between 12–14 UTC because the surface energy budget difference is close to zero for this time period and the difference in the surface temperature with the maximum at 7 UTC had quickly returned to 0.1 K due to the changes in shortwave surface net radiation flux and surface sensible heat flux.

Path 8 The cooling of the surface as presented in Fig. 2.17 has an impact on the domain averaged surface upward radiation flux. Its value accumulated in 24 hours is decreased by 0.9 %. The cooling of the surface is the main reason

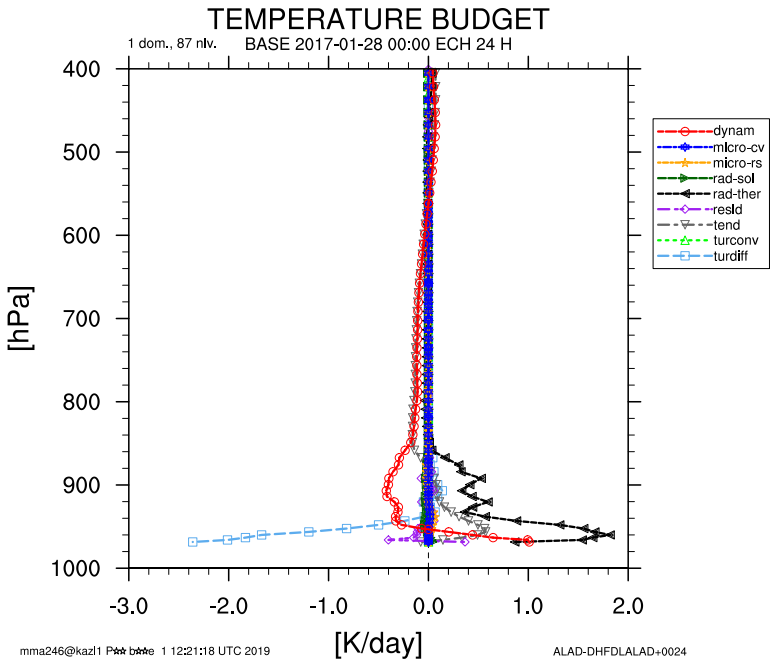

Figure 2.16: Domain averaged temperature budget (in K/day) for the difference between the experiment with unified critical relative humidity profiles and the reference on 29.1.2017, 0 UTC. Integration starts on 28.1.2017, 0 UTC.

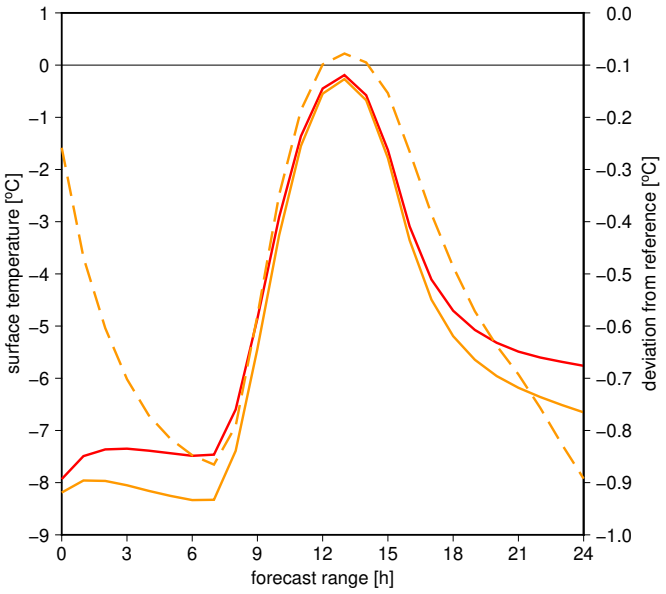

Figure 2.17: Evolution of domain averaged surface temperature (in °C) for the experiment with unified critical relative humidity profiles (orange), the reference (red) and their difference (dashed). Integration starts on 28.1.2017, 0 UTC. The image contains two scales. The left scale is for reference and experiment values, and the right scale is for their difference.

for the lower longwave surface net radiation flux as can be seen in Fig. 2.12 as

mentioned before.

Path 9, 10 We will describe the atmospheric stability at model levels 70 (approx. 920 hPa) and more at 24 UTC using Fig. 2.13. The case at 12 UTC will be omitted due to the similar characteristics of the temperature profile (except near the surface). However, this is not true for the atmospheric stability between the lowest model level and the surface. Because the surface and the lowest model level are relatively close, less than 10 m on average, the temperature would lower by just approx. 0.1 K when going from the surface to the lowest model level according to the dry adiabatic lapse rate in neutral stability conditions.

The differences between the current experiment and the reference will be described. The atmosphere is slightly less stable at model levels 70–80 (approx. 920–990 hPa) due to a slightly weaker inversion caused by the higher heating rate at model levels near 80 (approx. 990 hPa) due to the clouds reduction. At the same time, it is more stable at model levels 81 and more where PBL is located.

The atmosphere is stable between the surface and the lowest model level at 24 UTC which can be seen from Fig. 2.13. The temperature difference between the lowest model level and the surface is 2.6 K for the reference and 3.5 K for the experiment. Note that the atmosphere is unstable between the lowest model level and the surface at 12 UTC due to a warmer surface than at 24 UTC.

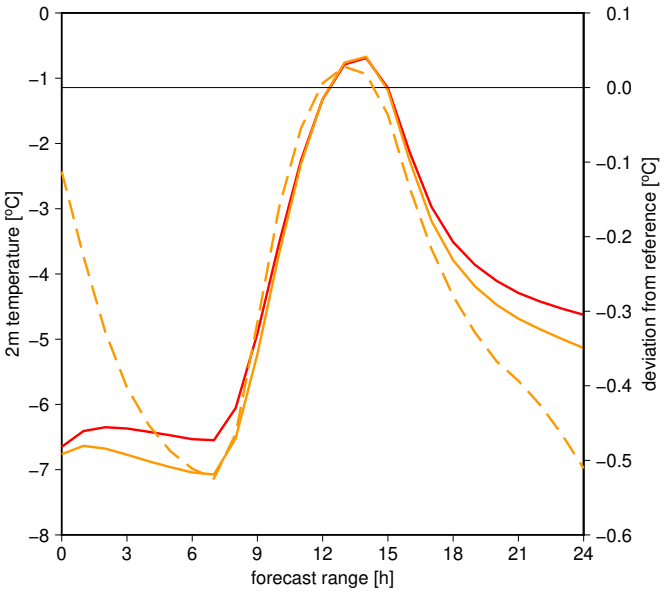

Figure 2.18: Evolution of domain averaged temperature at 2 m (in °C) for the experiment with unified critical relative humidity profiles (orange), the reference (red) and their difference (dashed). Integration starts on 28.1.2017, 0 UTC. The image contains two scales. The left scale is for reference and experiment values, and the right scale is for their difference.

The colder surface has an impact on the evolution of the domain averaged temperature at 2 m as can be seen in Fig. 2.18. The temperature at 2 m is lower up to 0.5 K at 7 UTC and 24 UTC. When looking at both the surface temperature and the temperature at 2 m, a very similar diurnal characteristics

can be noticed as expected. Around 12 UTC, the surface temperature is higher than the temperature at 2 m due to surface heating by the shortwave radiation. Otherwise, it is lower mainly due to surface cooling by the longwave radiation.

Path 11 The changes in the domain averaged surface sensible heat flux are as follows. We will start with the situation at 9–15 UTC when the surface sensible heat flux is negative as can be seen in Fig. 2.6 for the reference and in Fig. 2.12 for the difference between the experiment and the reference. The atmospheric stability between the surface and the lowest model level has not changed much. However, turbulence is weakened due to more stable conditions in the lower part of PBL. Hence, the heat transfer from the surface to PBL is limited and the surface sensible heat flux is less negative. Thus, the surface is losing less energy by heat transfer to PBL.

For the rest of the day, at 0–9 UTC and 15–24 UTC, the surface sensible heat flux is slightly more positive due to the greater temperature difference between the surface and the lowest model level compared to the reference. Hence, the surface is gaining more energy by the heat transfer from PBL. You can find more details about the surface sensible heat flux calculation in Section 2.2.4, Path 9.

Path 12, 13 Now, we will look how the domain averaged surface latent heat flux has changed. According to Fig. 2.6 and 2.30 which describe the surface budget, the surface latent heat flux is slightly less negative or unchanged. Hence, the surface is losing less energy by evaporation or sublimation to PBL. This is expected due to the lower surface temperature, and weaker turbulence at 9–15 UTC, because the evaporation or the sublimation decreases with lower temperature. Thus, the surface turbulent moisture flux is also limited.

Path 14 Fig. 2.19 shows the vertical profiles of domain averaged specific humidity. It can be seen that the reduction of specific humidity up to 0.06 g/kg dominates at model levels 40 (approx. 570 hPa) and more, and the absolute value of the difference between the experiment and reference is roughly decreasing with height. However, there is a small increase of specific humidity up to 0.01 g/kg at model levels 55–70 (approx. 760–920 hPa). For the remaining model levels, the change is negligible.

Fig. 2.20 presents the difference of domain averaged water vapour budget between the experiment and the reference obtained from DDH. The difference of specific humidity from Fig. 2.19 can be seen also in Fig. 2.20 and it is marked by the light green colour. For pressure levels 500–850 hPa which correspond roughly to model levels 35–65 in Fig. 2.19, the change is caused solely by advection (orange). For pressure levels 850 hPa and more which roughly correspond to model levels 65 and more in Fig. 2.19, the change is due to three partly compensating processes: advection (orange), turbulence (dark red) and stratiform condensation (dark blue). They reduce the final tendency which is the reason for the drying of PBL as can be seen in Fig. 2.19.

Path 15, 16 The evolution of domain averaged temperature of the deep soil layer (shortly deep temperature) for the reference and the experiment is shown in Fig. 2.21. Compared to the evolution of surface temperature in Fig. 2.17, it

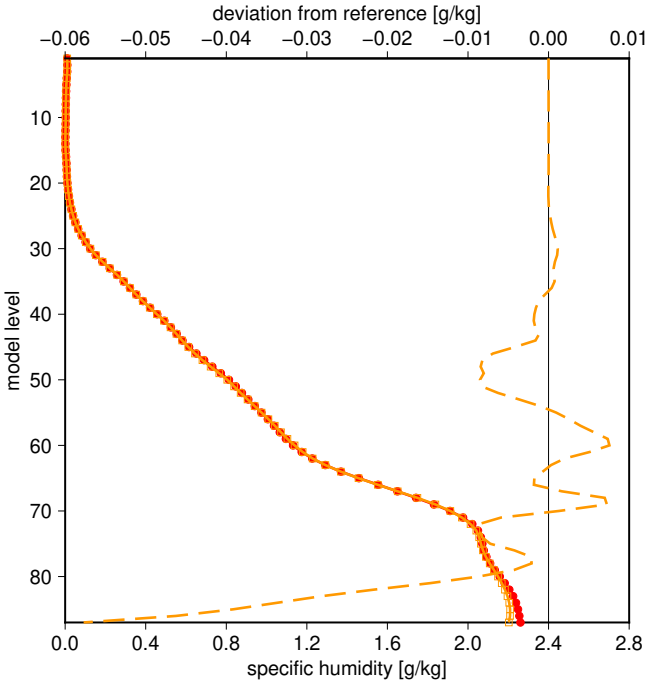

Figure 2.19: Vertical profiles of domain averaged specific humidity (in g/kg) for the experiment with unified critical relative humidity profiles (orange), the reference (red) and their difference (dashed) on 29.1.2017, 0 UTC. Integration starts on 28.1.2017, 0 UTC. The image contains two scales. The lower scale is for reference and experiment values, and the upper scale is for their difference.

can be seen that the evolution of deep temperature is phase-shifted by 1–3 hours and its diurnal variability is much lower, only 1.2 K compared to 8.0 K for the surface temperature.

The evolution of the deep temperature is calculated using the so-called force-restore method (Blackadar, 1976). More details on this method can be found in Section 2.2.4, Path 14.

The soil heat flux is proportional to the difference between the surface temperature and the deep temperature. The surface is losing energy via the soil heat flux during the day when the surface is sufficiently heated ($T_s > T_d$); the opposite holds during the night. In Fig. 2.6, it can be seen that the soil heat flux is positive except 11–15 UTC.

2.1.5 Verification

Verification of this experiment is done for five consecutive 72 hour forecasts, from 27th to 31st January 2017, all of them start at 0 UTC. The verification time step is 6 hours. The verification period of five model runs is adequate to get some information about the experiment and its reference when both are compared to observations. We will show only biases (BIAS) and standard deviations (STDE) because root mean squared errors (RMSE) can be easily calculated using the equation (2.3).

Because the verification is done for five model runs, a statistical significance

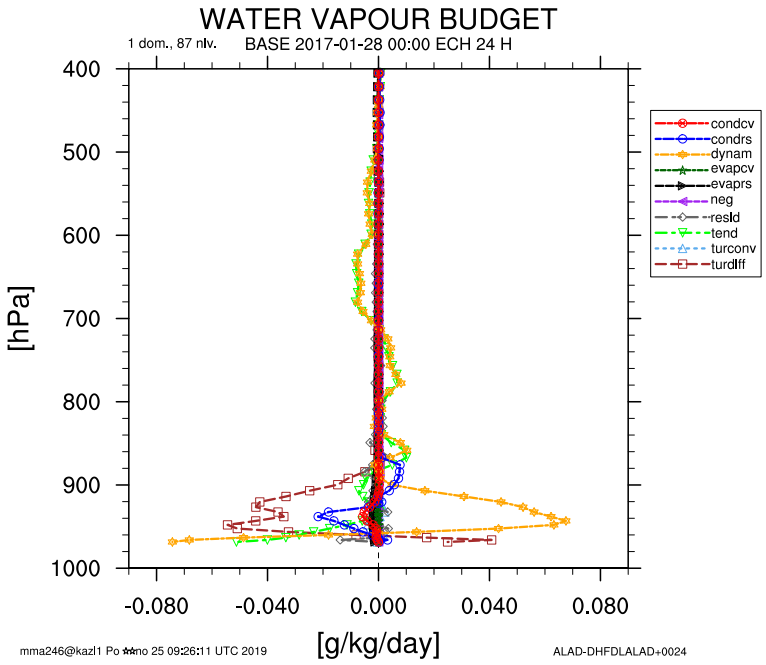

Figure 2.20: Domain averaged water vapour budget (in g/kg/day) for the difference between the experiment with unified critical relative humidity profiles and the reference on 29.1.2017, 0 UTC. Integration starts on 28.1.2017, 0 UTC.

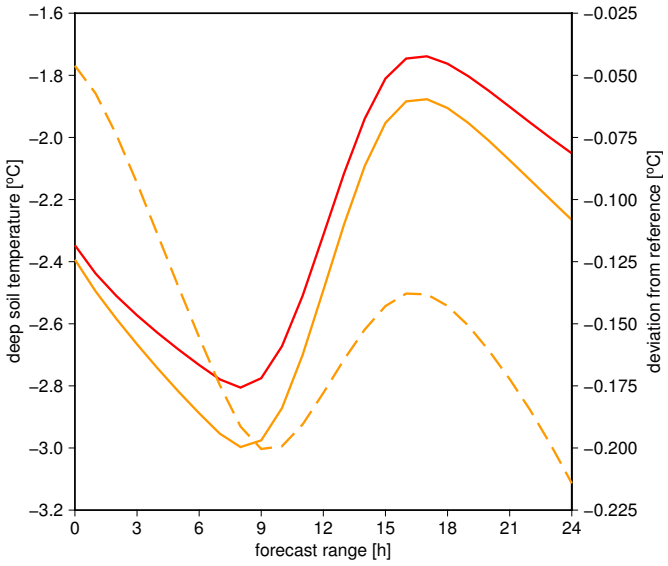

Figure 2.21: Evolution of domain averaged deep temperature (in °C) for the experiment with unified critical relative humidity profiles (orange), the reference (red) and their difference (dashed). Integration starts on 28.1.2017, 0 UTC. The image contains two scales. The left scale is for reference and experiment values, and the right scale is for their difference.

of both verification scores (BIAS, STDE) can be at least visually evaluated. In this case, we will look at the experiment mean verification scores with respect to the reference mean verification scores and their respective standard deviations. Moreover, we will analyze a response of the verification scores due to changes in the model setup which is called a "meteorological significance".

Fig. 2.22 shows the evolution of both verification scores (BIAS, STDE) with the forecast range for temperature at 2 m and total cloudiness. Positive BIAS of temperature at 2 m is reduced for the full forecast range and this reduction is statistically significant for only some verification time steps. Negative BIAS of total cloudiness is drastically increased for the full forecast range and this reduction can be seen as statistically significant. It indicated that the reduction of low cloudiness is undesirable when compared to observations. STDE of temperature at 2 m has not changed. However, STDE of total cloudiness is increased and this change is statistically significant during the day. This increase is probably caused by the unrealistic binary behaviour of low clouds.

In addition, a verification of hourly surface shortwave and longwave downward radiation flux is computed on twenty-nine 24 hour forecasts from 3rd to 31st January 2017 (a winter case) and on eighteen 24 hour forecasts from 14th to 31st May 2018 (a spring case). All forecasts start at 0 UTC. The surface shortwave downward radiation flux is verified at 19 stations and the surface longwave downward radiation flux at one station (Hradec Králové). All stations are located in the Czech Republic.

In the winter case, positive BIAS is slightly increased and STDE is slightly increased for surface shortwave downward radiation flux. For surface longwave downward radiation flux, positive BIAS is slightly reduced, but STDE is increased. In the spring case, positive BIAS is increased and STDE is slightly reduced at 2-9 UTC but increased at 10-19 UTC for surface shortwave downward radiation flux. For surface longwave downward radiation flux, positive BIAS is slightly reduced and STDE remains unchanged.

2.1.6 Conclusion

The main change in this experiment was the unification of the vertical critical relative humidity profiles for the stratiform cloud water in radiation and in microphysics according to the one for microphysics. The direct consequence is the reduction of low clouds due to higher critical relative humidity needed for the cloud formation. Adjusting the calculation of $\langle q \rangle$ and setting the parameter RPHI0 to zero caused further reduction of cloud cover. However, turning off the scaling of relative humidity via the key LQXRTGH, doubling the parameter QSSUSS and setting the parameter QSSUSV to zero partially compensated the mentioned cloud reduction.

We described what happened with cloud water for radiation when using a more realistic critical relative humidity profile and when removing some auxiliary parameters, such as RPHI0 which was set to zero. The low clouds cover was reduced. The cloud fraction exhibits a binary behaviour which was presented in Fig. 2.7.

The aforementioned changes were reflected in several feedback loops. All relevant feedback paths were illustrated by the diagram in Fig. 2.10 and thoroughly

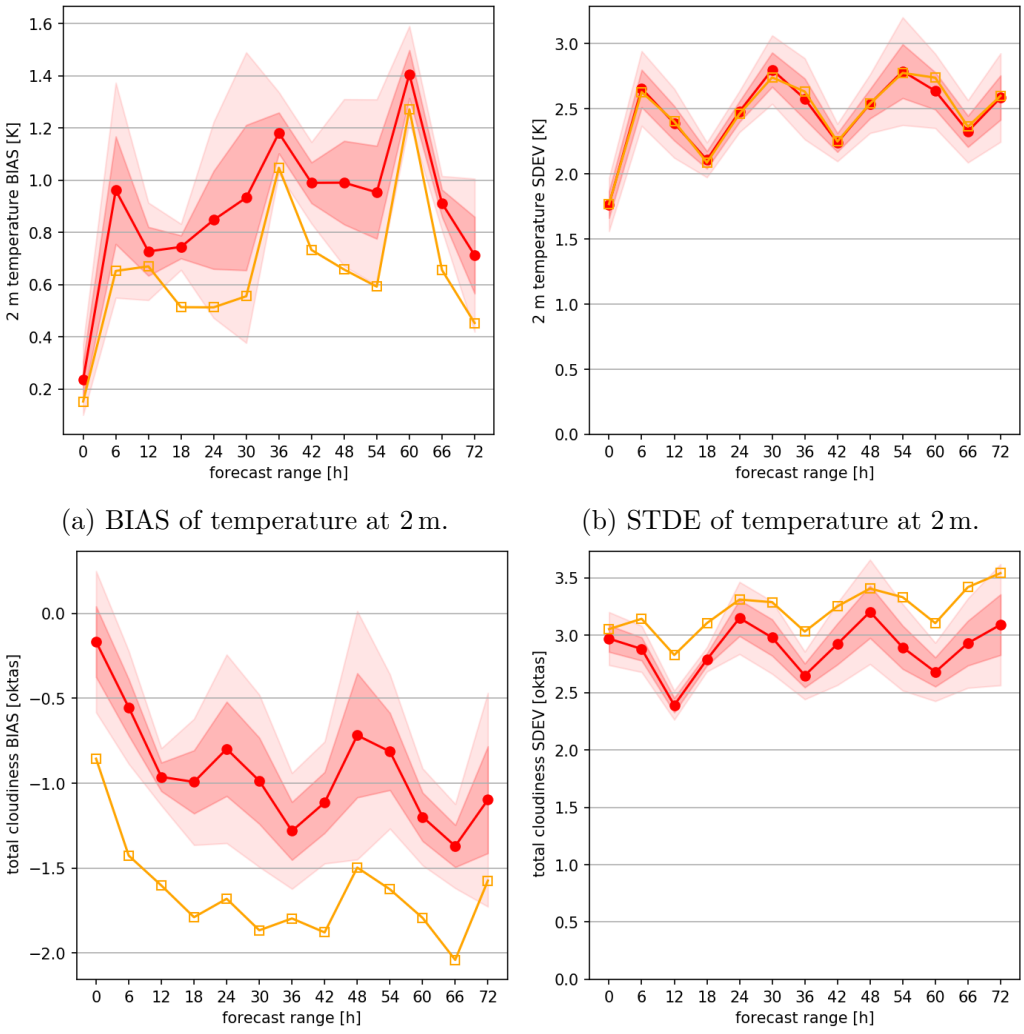

(a) BIAS of temperature at 2 m.

(b) STDE of temperature at 2 m.

(c) BIAS of total cloudiness.

(d) STDE of total cloudiness.

Figure 2.22: Evolution of verification scores with the forecast range for the experiment with unified critical relative humidity profiles (orange) and the reference (red). Verification is done for five consecutive 72 hour forecasts which start on 27.–31.1.2017, all of them at 0 UTC. The dark red area and the light red area represent one standard deviation and two standard deviations, respectively, from the mean values of reference verification scores.

described. The description was supplemented by domain averaged evolution and vertical profile graphs. We also included the outputs from DDH to understand how much individual processes influence the changes. Moreover, we used the radiation ACRANEB2 SCM to detect dominant exchange type causing observed longwave response.

The dominant process which influenced temperature at 2 m was the change in surface longwave net radiation flux due to a cloudiness reduction (caused by the changes in the model setup). This way, the surface cools more via the longwave radiation transfer to space.

The experiment verification was carried over five model runs, each is a 72 hour

forecast. This time period was sufficient to reveal a very significant cloud reduction compared to observations.

The changes made in the experiment are not suitable for further use due to the significant cloud reduction, the worsening of several verification scores and the binary behaviour of the low clouds cover. The experiment has shown the significance and feedbacks of the tested changes in the computing of cloud cover for radiation. The unification of vertical profiles of critical relative humidity cannot be applied without another modifications of the scheme to compensate for too much reduced cloud cover.

2.2 Gravity waves case

When a stable stratified flow goes above an obstacle such as a mountain, internal gravity waves (or mountain waves) are generated. They create the mountain wave drag associated with a flow deceleration occurring at a considerable distance from the mountain which is due to the transfer of momentum by the waves. The gravity wave drag (GWD) is frequently interchanged with the mountain wave drag and we will use the former term when describing the mountain wave drag parametrization.

The aim of this section is to determine if the usage of the GWD parametrization for horizontal resolution of 2.3 km can be still beneficial to the forecast quality. However, we will not study the lift parametrization which computes the wind horizontal deflection due to subgrid-scale mountains. It will be disabled for both the reference and the experiment.

In the next sub-sections, we will describe in more detail the GWD parametrization (computed by the routine ACDRAG) and the budget of enthalpy, which is related to the time evolution of temperature.

2.2.1 Relevant parametrizations

2.2.1.1 Gravity wave drag parametrization

The description of the GWD parametrization is based on Catry (2006). The lift parametrization will not be discussed. Only isotropic subgrid-scale mountains will be considered to simplify equations.

The basis of the GWD parametrization is how to express a stress generated by gravity waves. It can be generally written as

$$\vec{\tau} = \rho \left(\overline{u'w'}, \overline{v'w'} \right) \tag{2.13}$$

where ρ is the air density, the bar indicates the gridbox averaging and u', v', w' are the subgrid-scale perturbations of the respective mean values u, v, w describing the flow velocity. The vertical divergence of the stress $\frac{\partial \vec{\tau}}{\partial z}$ (called the drag), where z denotes the height, is a sink term in the equations of motion.

The atmospheric stability can be described by the Brunt-Väisälä frequency N, which is defined for the compressible atmosphere and unsaturated air as

$$N^2 = \frac{g}{\theta_v} \frac{\partial \theta_v}{\partial z} \tag{2.14}$$

where g is the acceleration due to gravity and θ_v is the virtual potential temperature. In stable atmospheric conditions ($N^2 > 0$), an air parcel will oscillate with a period of $2\pi/N$ (in an adiabatic case) after moving it a small distance out of its equilibrium. In unstable conditions ($N^2 < 0$), the air parcel distance from its original location will grow exponentially in time. In neutral conditions ($N^2 = 0$), the air parcel will remain in the equilibrium.

A characteristics of a subgrid-scale mountain is the effective obstacle height, expressed in the pressure units as

$$H = \min\left(p_s - p_1, \max\left(p_s - p_L, R\rho_s g h\right)\right) \tag{2.15}$$

where p is the air pressure, ρ_s is surface air density, h is the standard deviation of subgrid-scale (unresolved) orography and R is a dimensionless tuning parameter with a default value given in the Table 2.4. Therefore, the effective obstacle height H is proportional to the standard deviation of subgrid-scale orography h via the tuning parameter R. Then, there are two additional securities. The first one is to limit the effective obstacle height H to the pressure difference between the surface (denoted by s) and the model top (denoted by 1). The second security enforces a minimum value of the effective obstacle height H to the pressure difference of the surface and the lowest model level (denoted by L). However, then the scheme becomes practically inactive.

In order to apply results of inviscid gravity wave theory (with free slip surface condition) to a viscous case with zero surface velocity, values of the averaged surface wind $\vec{\overline{v}} = (\overline{u}, \overline{v})$ and the averaged surface squared Brunt-Väisälä frequency $\overline{N}^2$ characterizing the surface layer of height H are needed. They are obtained as averages of the wind $\vec{v} = (u, v)$ and the squared Brunt-Väisälä frequency N^2, respectively, over model levels below H, weighted by layer mass.

To avoid a discontinuity at the surface, the effective wind $\vec{\widetilde{v}}_l = (\widetilde{u}_l, \widetilde{v}_l)$ at model levels below H is defined as a linear combination of the averaged surface wind $\vec{\overline{v}}$ and the original value $\vec{v}_l$. The squared Brunt-Väisälä frequency N_l^2 is recalculated in the same way.

Now, we will express the wave component of the surface stress due to one subgrid-scale mountain with a circular base according to Catry (2006) as

$$\vec{\tau}_s = \kappa\rho_s\overline{N}h\vec{\overline{v}} \cdot \begin{cases} 1\ , & \text{if } F \le F_c \\ \frac{F_c}{F}\ , & \text{otherwise} \end{cases} \tag{2.16}$$

where κ is a dimensionless tuning parameter with a default value given in the Table 2.4, ρ_s is the surface air density, F and F_c are the Froude and the critical Froude numbers[1], respectively (more details given below). The equation (2.16) is similar to the one in Boer et al. (1984) for the case $F \le F_c$ but modified by the factor F_c/F for the case $F > F_c$. The expression of the surface stress $\vec{\tau}_s$ is assuming that the stress is caused only by generated waves with the same wavelength which is so-called monochromatic approach.

After the surface stress $\vec{\tau}_s$ is expressed, a vertical profile of stress relating $\vec{\tau}_l$ to $\vec{\tau}_s$ has to be found. Following Lindzen's saturation theory (Lindzen, 1981),

[1] Catry (2006) uses the inverse Froude number and the inverse critical Froude number in his formulations.

the ratio (evaluated at half levels) between the stress at level l and the surface is given by Catry (2006) as

$$\gamma_l = \frac{\overline{N}}{N_l}\left(\frac{\rho_l}{\rho_s}\right)^2\left(\frac{U_l}{\overline{U}}\right)^3 \tag{2.17}$$

where $\overline{U} = \left|\vec{\overline{v}}\right|$ and U_l is the effective wind $\vec{\tilde{v}}_l$ projected onto the averaged surface wind $\vec{\overline{v}}$ as follows

$$U_l = \frac{\vec{\tilde{v}}_l \cdot \vec{\overline{v}}}{\left|\vec{\overline{v}}\right|} \ . \tag{2.18}$$

The equation (2.17) reflects the assumption that the surface stress is saturated.

The stress cannot increase with height because there is no source term. Therefore, the factor Γ (at half levels) non-increasing with height is introduced as

$$\Gamma_l = \max\left\{0, \min\left(\gamma_l, \Gamma_{l+1}\right)\right\} \ . \tag{2.19}$$

Finally, the stress at a half level l is written as

$$\vec{\tau}_l = \Gamma_l \vec{\tau}_s \ . \tag{2.20}$$

We can see that the stress has the same direction as the surface stress which is so-called uni-directional representation.

Fig. 2.23 shows a vertical profile of Γ with $\Gamma_s = 1$. An example of model values is given by the solid line, possible real values are indicated by the dotted line, and the first critical level and an extinction level are both shown as dashed horizontal lines. The first critical level is defined as the first level (counted from the surface upwards) where Γ starts to decrease ($\Gamma < 1$) which means that the drag occurs. The extinction level ($\Gamma = 0$) is defined as the level where $U = 0$, meaning that the wind ceases to sustain the wave, or $\rho = 0$, which is the model top. Hence, there is no stress generated by gravity waves.

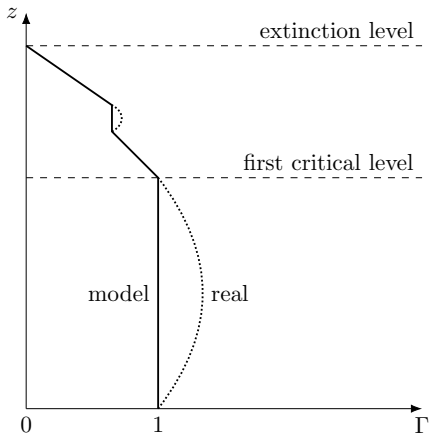

Figure 2.23: The vertical profile of Γ in model and in the reality, after (Catry, 2006).

In summary, the stress at the half level l expressed in the equation (2.20), depending on the surface stress, is given by the vertical profile of Γ . However,

for practical use, the vertical profile of Γ expressed in the equation (2.19) is oversimplified. Thus, the stress is further modified to include effects as resonance, wave trapping and low level flow blocking.

Resonance As mentioned before, the wave deposition, called the drag, occurs at the first critical level. Here, a part of the wave is reflected down and can interfere with incoming waves. The reflected wave will undergo several reflections between the first critical level and the surface.

In the case of resonant amplification of waves, the value Γ_s is increased which causes the increase of the surface stress $\vec{\tau}_s$. Then, the profile of Γ_l is linearly interpolated in the pressure coordinate between the increased value Γ_s at the surface and the original value Γ at the first critical level. The profile of Γ_l is not modified above the first critical level.

In the case of resonant destruction of waves, the value Γ_s is decreased which causes the decrease of the surface stress $\vec{\tau}_s$. Then, the profile of Γ_l is set to the constant value of Γ_s up to the level where the original Γ_l is smaller than Γ_s. Above this level, the profile of Γ_l is not modified.

Wave trapping We start by searching for the lowest level where $N^2 < 0$. This level is called the trapping level, the wave cannot propagate above it and will be reflected downwards.

If the trapping level is below the first critical level, the resonance will not occur. Then, the vertical profile of Γ_l is linearly interpolated in the pressure coordinate between the value $\Gamma_s = 1$ at the surface and zero at the trapping level. Above the trapping level, we set $\Gamma_l = 0$.

If the trapping level is above the first critical level, the resonance occurs. Then, the vertical profile of Γ_l is linearly interpolated in the pressure coordinate between the value Γ_s at the surface and zero at the trapping level. In the case of resonant amplification, the value of Γ_s is set to one. In the case of resonant destruction, the value $\Gamma_s < 1$. Above the trapping level, we set $\Gamma_l = 0$.

Blocked flow To describe the flow stability, the Froude number is defined as

$$F = \frac{\overline{U}}{Rh\overline{N}} \ . \tag{2.21}$$

When the flow is stable ($F \leq F_c$), the low-level flow is blocked by the mountain and goes around it. However, the upper-level flow can still go above the mountain. The parameter F_c is the critical Froude number with the default value given in the Table 2.4.

Following Lott and Miller (1997), the height of the blocked flow (in pressure units) is expressed as

$$Z_b = H \max\left(0, \frac{F_c - F}{F_c}\right) \ . \tag{2.22}$$

Below the level Z_b, the flow goes around the mountain which exerts a drag on the flow, called a form drag (Catry, 2006). The term "form drag" is also used in the turbulence parametrization (the scheme TOUCANS), but it has a different

meaning there because it is generated by turbulent wakes behind small-scale obstacles and parametrized via the effective surface roughness.

In the case of the blocked flow, the value Γ_s is increased beyond 1 and the value Γ_l is decreasing with an increasing height up to the value $\Gamma \gtrapprox 1$ at the height Z_b. Above the height Z_b, the value Γ_l is decreasing down to $\Gamma = 1$ at the height H.

Parameter	Value	Units
R (HOBST)	3	1
κ (GWDSE)	$5{\times}10^{-3}$	1
F_c (GWDBC)	2	1

Table 2.4: Tuning parameters used in the gravity wave drag parametrization scheme.

Note that the only output of the GWD parametrization scheme is the momentum flux which we wrote as stress at half levels $\vec{\tau}_l$. It is calculated via the equation (2.20) where the factor Γ_l is modified to include aforementioned effects of resonance, wave trapping and low level flow blocking. In the next section, we will introduce how the change in the momentum flux can influence temperature.

2.2.1.2 Enthalpy budget

The enthalphy budget is relevant for the studied case, so we mention it here. It describes the temperature tendency which can be expressed as (Piriou, 2018)

$$\frac{\partial}{\partial t}\left(r_\eta c_p T\right) = -\nabla_\eta.\left(r_\eta c_p T \vec{v}\right) - \frac{\partial}{\partial \eta}\left(r_\eta c_p T \dot{\eta}\right) + r_\eta R T \frac{\omega}{\pi} + F \tag{2.23}$$

where t is time, c_p is the specific heat capacity at constant pressure for air, T is the air temperature, $\nabla_\eta.$ is the divergence operator applied along the constant η-surface, $\vec{v}$ is the horizontal wind, $\dot{\eta} = \frac{\mathrm{d}\eta}{\mathrm{d}t}$ is the vertical velocity in η-coordinate, R is the gas constant for air, $\omega = \frac{\mathrm{d}\pi}{\mathrm{d}t}$ is the vertical velocity in π-coordinate, π is the hydrostatic air pressure, F contains the remaining terms (e.g. vertical divergence of the net radiation flux) and r_η is expressed as

$$r_\eta = -\frac{1}{g}\frac{\partial \pi}{\partial \eta}\ . \tag{2.24}$$

In the equation (2.23), the expression

$$r_\eta R T \frac{\omega}{\pi} \tag{2.25}$$

is called the "conversion term" and the expression

$$\nabla_\eta.\left(r_\eta c_p T \vec{v}\right) + \frac{\partial}{\partial \eta}\left(r_\eta c_p T \dot{\eta}\right) \tag{2.26}$$

is the 3D divergence of the resolved enthalpy flux.

The conversion term describes how enthalpy (temperature) of an air particle changes due to a vertical adiabatic motion described by the vertical velocity ω. It expresses the conversion between kinetic and potential energy.

The 3D divergence of the resolved enthalpy flux shown in the equation (2.26) combines effects from both advection and compression (expansion). One can separate the advection and compression effects by writing out the divergence into more terms.

As can be seen, both the conversion term and the 3D divergence of the resolved enthalpy flux are influenced by changes in the momentum flux, e.g. by the GWD parametrization. Thus, they will have an important role when describing the experiment with parametrized gravity waves in Section 2.2.3.

2.2.2 Reference experiment

This reference experiment is the same as the one used in Section 2.1.2 with the exception of the DDH and diagnostic domain. Both, the GWD and lift parametrizations are disabled. The reference is used as a baseline and the experiment with parametrized gravity waves (see Section 2.2.3) will be later compared to it.

To describe the feedback loops in a winter case, the start of the integration is chosen on 28th January 2017 at 0 UTC. The DDH domain has the left bottom corner at (47.5°N, 12°E) and the right upper corner at (51°N, 16°E). The diagnostic domain used for the vertical profiles and evolution graphs is the same as the DDH domain. The DDH and diagnostic domains are selected like this because of a cooling at the pressure levels near 925 hPa and a warming at the pressure levels near 850 hPa. This is shown in Section 2.2.3 in more detail.

The existing temperature inversion (Fig. 2.24) makes the conditions suitable for propagation of gravity waves due to strongly stable stratification. The influence of precipitation on feedback loops can be neglected on the selected domain as shown in Fig. 2.4.

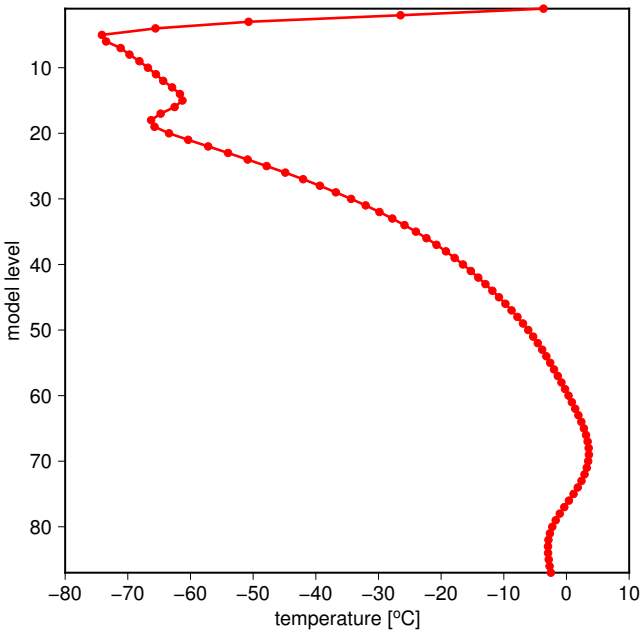

Figure 2.24: Vertical profile of domain averaged temperature (in °C) for the reference on 28.1.2017, 12 UTC. Integration starts on 28.1.2017, 0 UTC.

Now, we will look at the surface energy budget and associated fluxes. Fig. 2.25 shows the evolution of the domain averaged surface energy budget and associated fluxes. Because each flux and the surface energy budget has the same characteristics as those in Section 2.1.2, one can read the detailed description there and we will omit it here. The fluxes are similar because the DDH and diagnostic domains changed only slightly compared to those in Section 2.1.2.

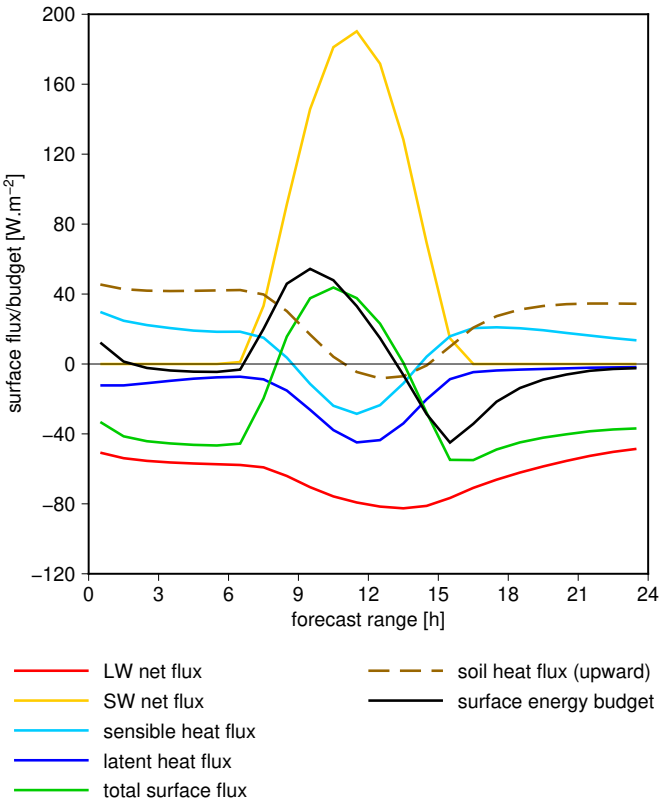

Figure 2.25: Evolution of domain averaged surface energy budget and associated fluxes (in W/m^2) for the reference. Integration starts on 28.1.2017, 0 UTC.

2.2.3 Experiment with parametrized gravity waves

The main characteristics of this experiment is the activation of the GWD parametrization with its tuning from the model version used with the horizontal resolution of 4.7 km. However, the lift parametrization remains deactivated. We use the CHMI model version CY43T2_op2. The changes in the model setup compared to the reference are as follows:

1. set LGWD from .F. to .T. (the activation of the GWD parametrization),
2. set GWDCD from 6.0 to 5.4 (drag coefficient for low level GWD),
3. set GWDSE from 0.0035 to 0.02 (aspect ratio coefficient for GWD at the surface),
4. set GWDVALI from 0.0 to 0.5 (decoupling coefficient for GWD in valleys).

Following differences are calculated between this experiment and the reference described in Section 2.2.2. When specifying model level numbers, we will also mention the corresponding rounded pressure from the Table 2.1.

First, in Fig. 2.26 the difference of 10 m wind speed between the current experiment and the reference is shown. The wind speed at 10 m is slower over almost the entire domain which confirms the expectation that the mountain wave drag slows down the near-surface flow.

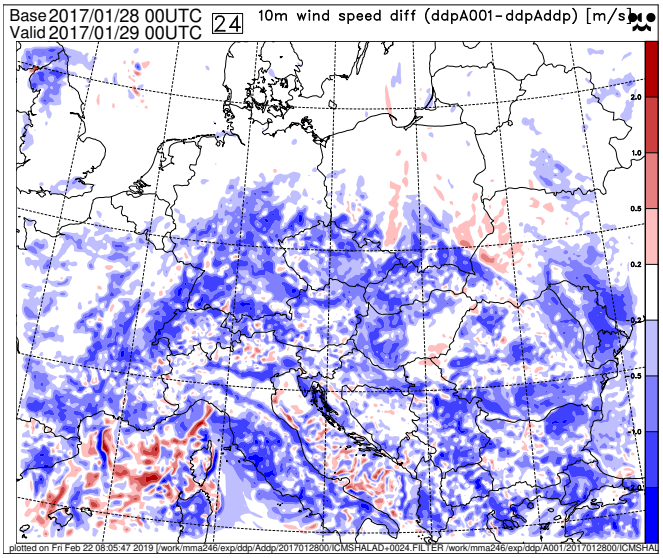

Figure 2.26: The difference of wind speed at 10 m above the surface (in m/s) between the experiment with parametrized gravity waves and the reference on 29.1.2017, 0 UTC. Integration starts on 28.1.2017, 0 UTC.

Next, Fig. 2.27 shows the vertical profile of domain averaged wind speed. We can see that a significant deceleration occurs below the model level 75 (approx. 960 hPa) which slows down the wind. The wind speed reduction reaches up to 0.8 m/s which is caused by the GWD parametrization. Another section is between the model levels 30–65 (approx. 420–870 hPa) where the wind speed reduction reaches up to 0.3 m/s. However, this deceleration is not that significant due to high absolute wind speeds compared to near-surface values.

Finally, in Fig. 2.28 the vertical profile of domain averaged wind direction is shown at 12 UTC to represent atmospheric conditions during the day. The near-surface wind direction is approx. 145° and it veers up to 250° at the model level 70 (approx. 920 hPa), and then it is backing. Just below the model level 70 (approx. 920 hPa), the wind has turned 90° compared to the near-surface value which means that here is the extinction level. According to equations 2.18 and 2.20, when wind veers more than 90°, there should be an acceleration of wind speed which is confirmed in Fig. 2.27 at the model levels 65–75 (approx. 870–960 hPa). However, the vertical profiles are domain averaged, therefore, the extinction level does not have to exist at some grid points for these model levels but at different heights. Hence, we can see slight wind speed deceleration even at model levels 30–65 (approx. 420–870 hPa) as mentioned before.

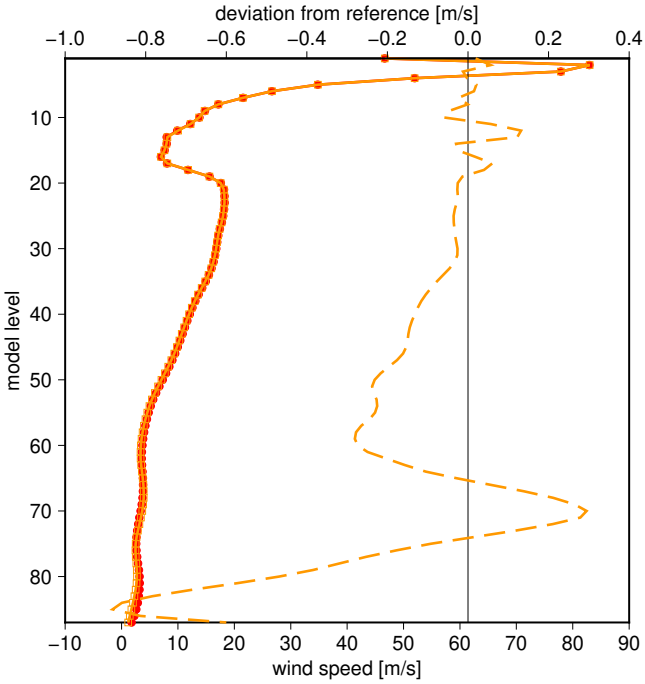

Figure 2.27: Vertical profiles of domain averaged wind speed (in m/s) for the experiment with parametrized gravity waves (orange), the reference (red) and their difference (dashed) on 29.1.2017, 0 UTC. Integration starts on 28.1.2017, 0 UTC. The image contains two scales. The lower scale is for reference and experiment values, and the upper scale is for their difference.

2.2.4 Feedback loops

In Fig. 2.29 individual feedback paths that are relevant in the studied case are shown. These feedback paths will be further described in more detail. Note the different changes in this experiment compared to the experiment with unified critical relative profiles (see Section 2.1.3). Both experiments and their respective references start on the same day and at the same time.

Path 1, 2 The domain averaged surface downward shortwave radiation flux accumulated in 24 hours is reduced only slightly by 1.4 % due to an increase in low cloudiness. Fig. 2.30 presents the evolution of domain averaged surface energy budget for the difference between the experiment and the reference. As a consequence of the surface downward shortwave radiation flux reduction, we can also see a reduction in the surface shortwave net radiation flux up to 3 W/m^2 at 12 UTC. We will neglect the changes, if any, of the surface albedo between both experiments in the interpretation of results.

The domain averaged surface downward longwave radiation flux accumulated in 24 hours is increased by just 0.2 %. This change is due to the increase in low cloudiness until 15 UTC which can be, for example, seen in Fig. 2.31 at model levels 75–85 (approx. 960–1010 hPa). However, in this layer, the temperature is lower in the current experiment than in the reference which can be seen in Fig. 2.32. The temperature profile at 12 UTC has the same characteristics as the

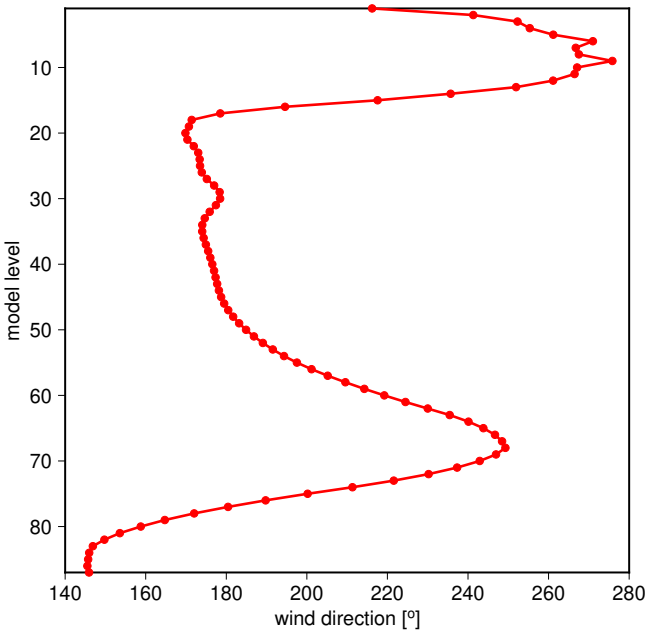

Figure 2.28: Vertical profile of domain averaged wind direction (in degrees) for the experiment with parametrized gravity waves on 28.1.2017, 12 UTC. Integration starts on 28.1.2017, 0 UTC.

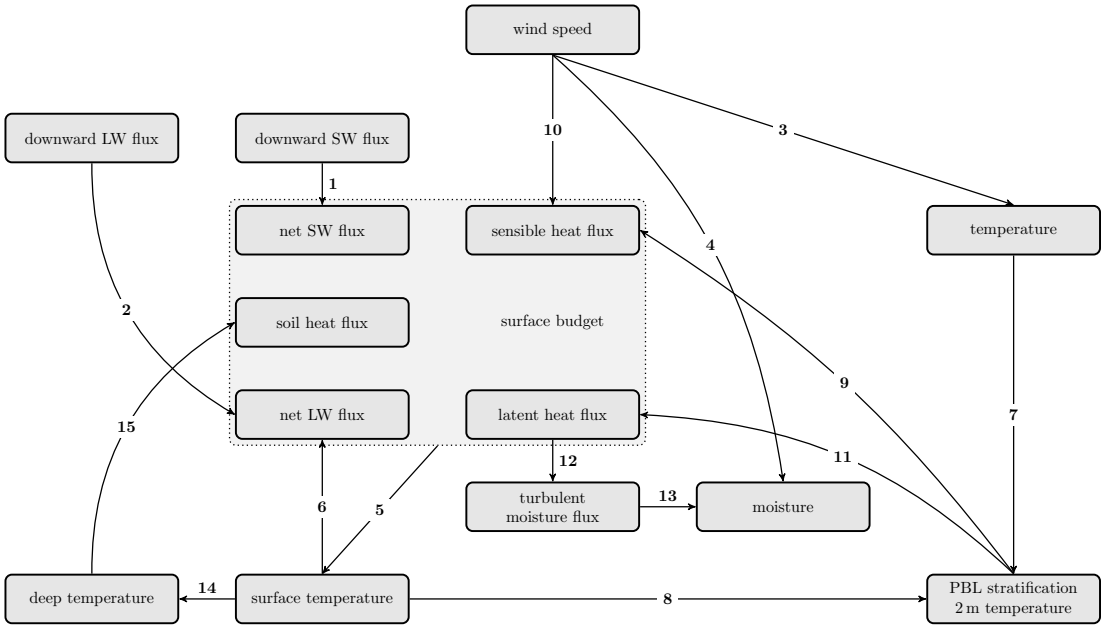

Figure 2.29: Diagram of feedback loops with numbered paths for the experiment with parametrized gravity waves.

one at 24 UTC, so we will omit it. These two partly compensating effects are the reason why the surface downward longwave radiation flux has not changed much.

The increase in low cloudiness is a result of another two partly compensating factors: a cooling of PBL as we saw in Fig. 2.32 and a drying of PBL (for more details see Path 4). The decrease of the net surface longwave radiation flux, as

can be seen in Fig. 2.30, is due to an other process (for more details see Path 6). Note that the net surface longwave radiation flux is negative which means that the decrease of its absolute value will show as a positive value when doing the difference between the experiments.

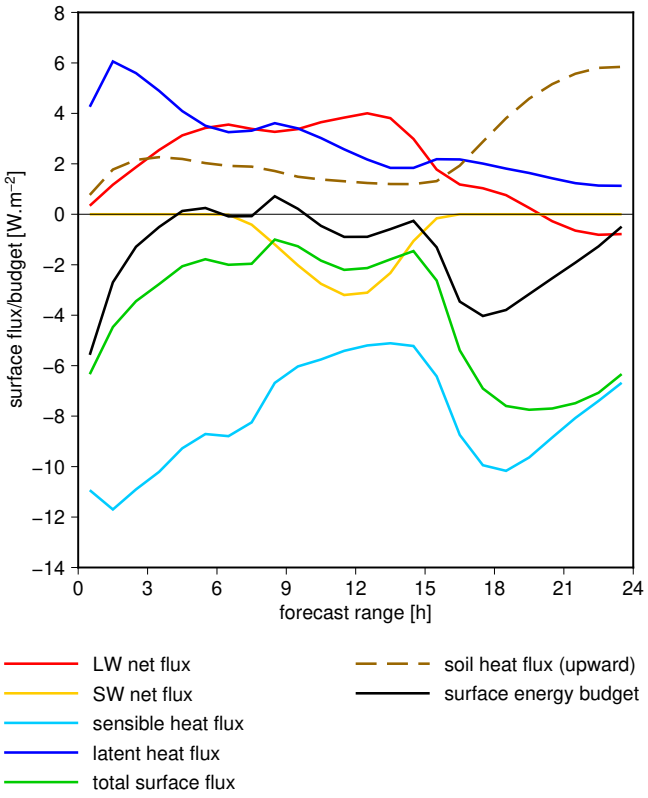

Figure 2.30: Evolution of domain averaged surface energy budget and associated fluxes (in W/m^2) for the difference between the experiment with parametrized gravity waves and the reference. Integration starts on 28.1.2017, 0 UTC.

Path 3 The GWD parametrization has modified the vertical profile of wind speed (Fig. 2.27) and wind direction (Fig. 2.28). This change has an impact on the vertical profile of temperature which we saw in Fig. 2.32 in previous feedback paths. The temperature inversion at model levels 70 (approx. 920 hPa) and more is now cooler up to 0.5 K and these levels are also parts of the PBL. However, we can see a warming of the free atmosphere at model levels 30–70 (approx. 420–920 hPa) up to 0.2 K.

To understand how the wind can influence the temperature, we will use DDH. It will show us how individual terms of a budget equation, for example the one in the equation (2.23), affect the tendency of a studied quantity.

Fig. 2.33 shows the difference of domain averaged temperature budget between the experiment and the reference, obtained from DDH. It can be seen that the aforementioned change in the vertical profile of temperature is shown in the black colour and it is caused by the "conversion term" (red) with the definition given in the equation (2.25) and the 3D divergence of the resolved enthalpy flux (orange) with the definition given in the equation (2.26). We explained what both terms

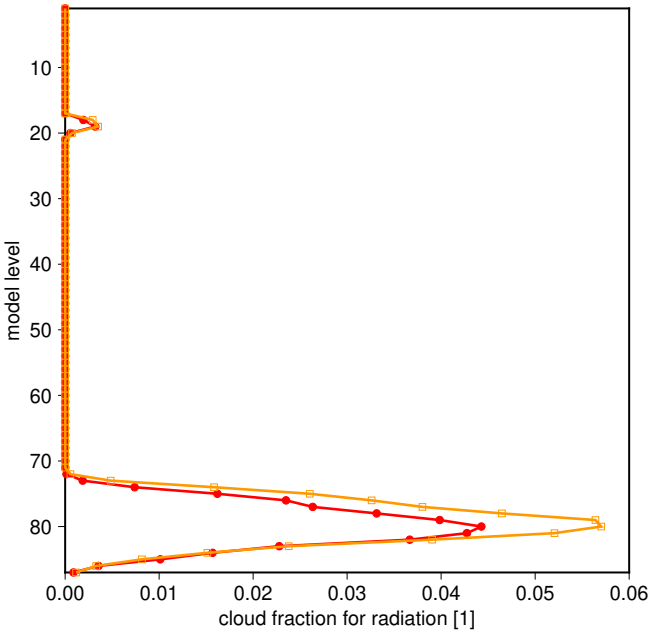

Figure 2.31: Vertical profiles of domain averaged cloud fraction for radiation (dimensionless) for the experiment with parametrized gravity waves (orange) and the reference (red) on 28.1.2017, 12 UTC. Integration starts on 28.1.2017, 0 UTC.

mean just below their definitions.

These two terms compensate each other but not perfectly. This partial compensation is the cause of aforementioned change in the vertical profile of temperature. There is almost total compensation at pressure levels 500 hPa and less, which roughly correspond to model levels 30 and less in Fig. 2.32 where we can see that the change is negligible.

Path 4 The GWD parametrization has modified the wind velocity as we showed before. This change has also an impact on the domain averaged vertical profile of specific humidity which can be seen in Fig. 2.34. It can be seen that the atmosphere is more dry at model levels 45 (approx. 630 hPa) and more up to 0.13 g/kg which includes both the PBL and the free atmosphere. Above this layer, the specific humidity remains almost unchanged.

In Fig. 2.35 the difference of domain averaged water vapour budget between the experiment and the reference is presented. The change in the vertical profile of specific humidity is shown in the light green colour. For pressure levels 600–940 hPa which roughly correspond to model levels 40–80 in Fig. 2.34, the change is caused solely by advection (orange). For pressure levels 960 hPa and more which roughly correspond to model levels 81 and more in Fig. 2.34, the change is due to a partly compensating process: the advection and the turbulence in the PBL (dark red) which tries to balance the water vapour budget (more on the turbulence later in Path 13). For remaining pressure and model levels, the change is negligible.

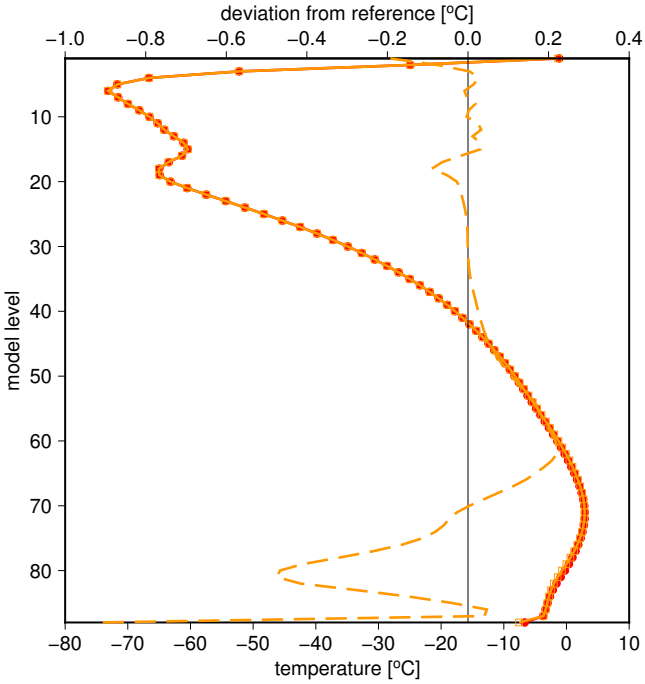

Figure 2.32: Vertical profiles of domain averaged temperature (in °C) for the experiment with parametrized gravity waves (orange), the reference (red) and their difference (dashed) on 29.1.2017, 0 UTC. Integration starts on 28.1.2017, 0 UTC. The lowest model level corresponds to the surface. The image contains two scales. The lower scale is for reference and experiment values, and the upper scale is for their difference.

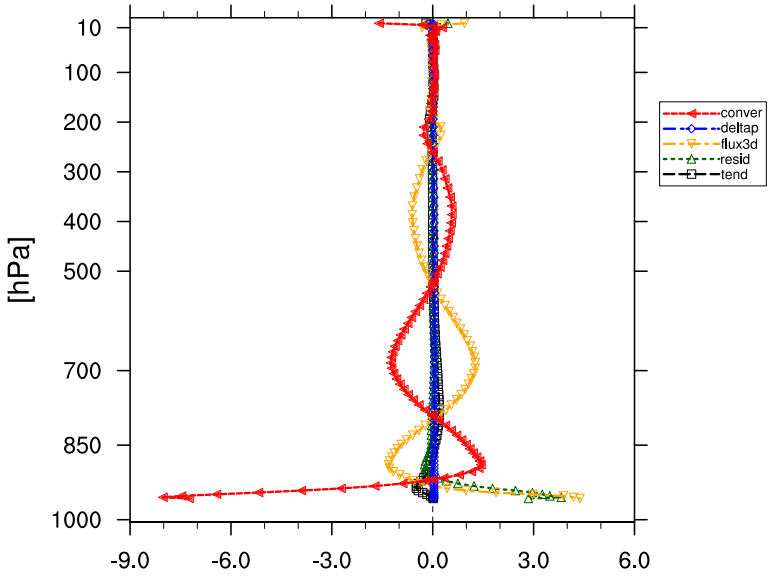

Figure 2.33: Domain averaged temperature budget (in K/day) for the difference between the experiment with parametrized gravity waves and the reference on 29.1.2017, 0 UTC. Integration starts on 28.1.2017, 0 UTC.

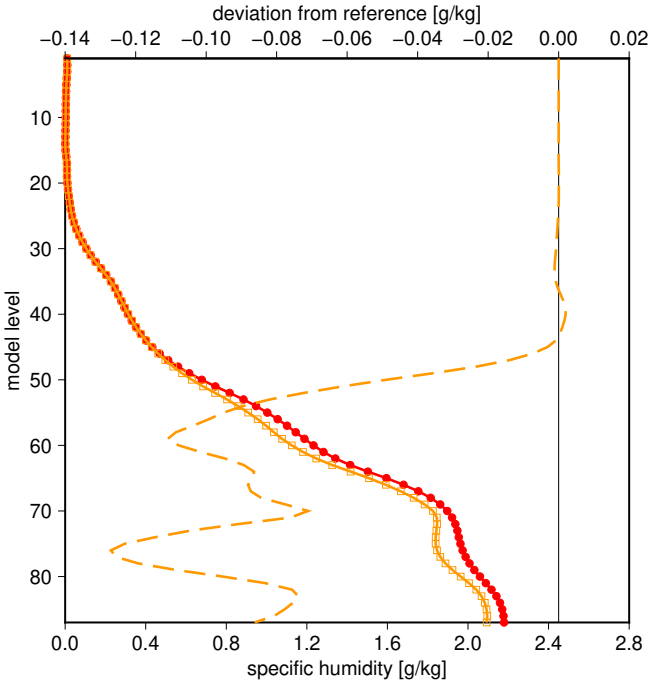

Figure 2.34: Vertical profiles of domain averaged specific humidity (in g/kg) for the experiment with parametrized gravity waves (orange), the reference (red) and their difference (dashed) on 29.1.2017, 0 UTC. Integration starts on 28.1.2017, 0 UTC. The image contains two scales. The lower scale is for reference and experiment values, and the upper scale is for their difference.

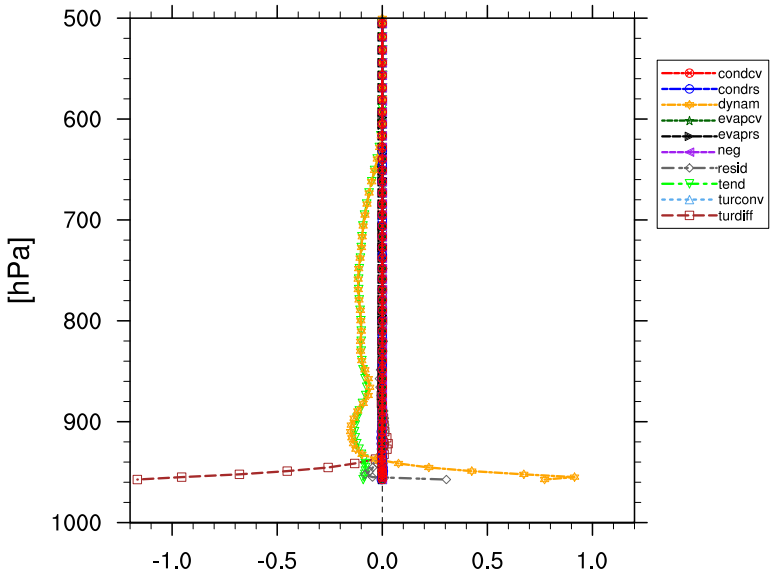

Figure 2.35: Domain averaged water vapour budget (in g/kg/day) for the difference between the experiment with parametrized gravity waves and the reference on 29.1.2017, 0 UTC. Integration starts on 28.1.2017, 0 UTC.

Path 5 The surface energy budget has a direct impact on the surface temperature. We showed both the evolution of domain averaged surface energy budget for the reference in Fig. 2.25 and the difference between the experiment and the reference in Fig. 2.30. After the comparison, we can say that the surface energy budget for the experiment accumulated in 24 hours is positive but less than the one for the reference.

The consequence can be seen in Fig. 2.36 which shows the evolution of domain averaged surface temperature. We can now confirm for the current experiment that the surface temperature is indeed higher at 24 UTC than at 0 UTC. Moreover, the surface temperature is now less than in the reference with differences up to 0.9 K.

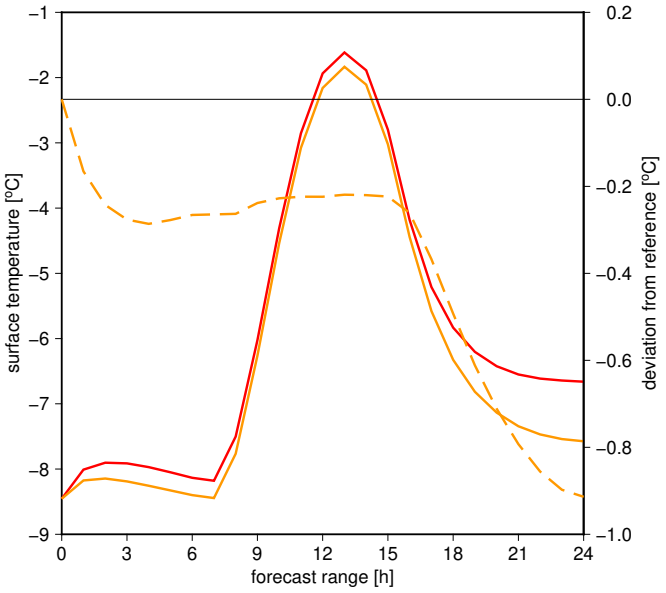

Figure 2.36: Evolution of domain averaged surface temperature (in °C) for the experiment with parametrized gravity waves (orange), the reference (red) and their difference (dashed). Integration starts on 28.1.2017, 0 UTC. The image contains two scales. The left scale is for reference and experiment values, and the right scale is for their difference.

Two drops in the surface temperature difference occur. The first at 0–3 UTC when the difference drops by 0.2 K and the second at 15–24 UTC when the difference drops gradually by another 0.7 K. When looking at both surface energy budgets, both drops can be explained mostly by the lower sensible heat flux in the experiment for those time periods. The surface temperature difference does not change much between 3–15 UTC because the surface energy budget difference is near zero for this time period.

Path 6 The cooling of the surface as seen in Fig. 2.36 has an impact on the domain averaged surface upward longwave radiation flux. Its value accumulated in 24 hours is decreased by 0.5 %. This cooling is the main reason for the decrease of the net surface longwave radiation flux, which can be seen in Fig. 2.30, as we mentioned before.

Path 7, 8 The atmospheric stability at model levels 70 (approx. 920 hPa) and more at 12 UTC has a similar characteristics as the one at 24 UTC (see below), so we will describe only the later case and omit the former. However, this statement does not hold for the atmospheric stability between the lowest model level and the surface. Because the surface and the lowest model level are relatively close, less than 10 m on average, the temperature would lower by just approx. 0.1 K when going from the surface to the lowest model level according to the dry adiabatic lapse rate in neutral stability conditions.

Now, we will describe the differences between the current experiment and the reference. The atmosphere is more stable at model levels 70–80 (approx. 920–990 hPa) due to a stronger inversion made mainly by the cooling at model levels near 80 (approx. 990 hPa), but it is slightly less stable at model levels 81 and more. These levels also belongs to the PBL.

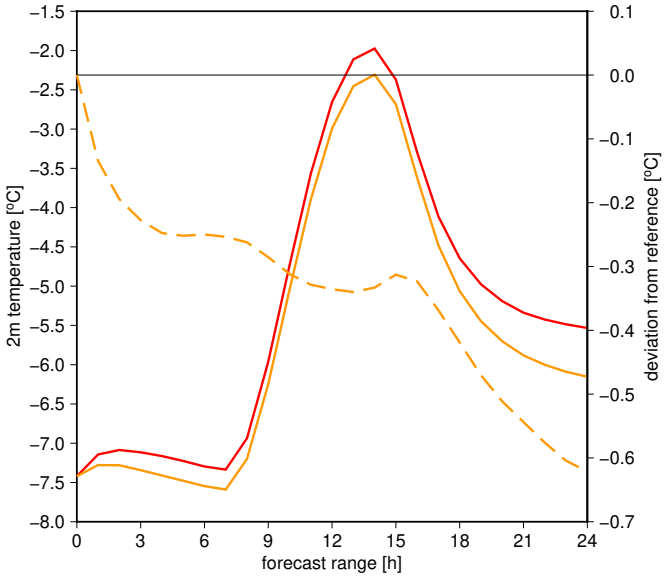

Figure 2.37: Evolution of domain averaged temperature at 2 m (in °C) for the experiment with parametrized gravity waves (orange), the reference (red) and their difference (dashed). Integration starts on 28.1.2017, 0 UTC. The image contains two scales. The left scale is for reference and experiment values, and the right scale is for their difference.

The atmosphere is stable between the surface and the lowest model level at 24 UTC which can be seen in Fig. 2.32. The difference of temperature between the lowest model level and the surface is 3.0 K for the reference and 3.9 K for the experiment. However, the atmosphere is unstable for the aforementioned levels at 12 UTC due to a warmer surface than at 24 UTC.

The colder surface also affects the evolution of the domain averaged temperature at 2 m which can be seen in Fig. 2.37. The temperature at 2 m is lower up to 0.6 K at 24 UTC. When looking at both the surface temperature and the temperature at 2 m, we can notice a very similar diurnal variation as expected. At 12 UTC and near, the surface temperature is higher than the temperature at 2 m due to surface heating by the shortwave radiation. Otherwise, it is lower mainly due to surface cooling by the longwave radiation.

Path 9, 10 Now, we will describe the changes in the domain averaged surface sensible heat flux. First, lets discuss the situation at 9–15 UTC when the surface sensible heat flux is more negative which can be seen in Fig. 2.25 for the reference and in Fig. 2.30 for the difference between the experiment and the reference. That means the surface is losing more energy by heat transfer to the PBL. The atmospheric stability between the surface and the lowest model level has not changed much, however, turbulence is weakened and the wind at the lowest model level is slower which was shown in Fig. 2.26 because the distance between the lowest model level height and the surface is near 10 m.

The surface sensible heat flux can be expressed as

$$\text{surface sensible heat flux} \sim C_H(Ri)(T_L - T_s)u_L \tag{2.27}$$

where T is temperature, u is wind speed and C_H is a proportionality factor dependent on the Richardson number Ri. The Richardson number is more negative due to the slower wind at the lowest model level which increases the value of C_H. This is the main reason for the stronger surface sensible heat flux even if the other terms in the equation (2.27) are smaller or unchanged.

Finally, for the rest of the day, at 0–9 UTC and 15–24 UTC, the atmospheric stability between the surface and the lowest model level is more stable. The surface sensible heat flux is less positive which can be seen in Fig. 2.25 for the reference and in Fig. 2.30 for the difference between the experiment and the reference. Hence, the surface is gaining less energy by the heat transfer from PBL.

Path 11, 12 The description of the domain averaged surface latent heat flux is simpler than the surface sensible heat flux because its value is just negative which also means that the surface is losing energy by evaporation or sublimation to the PBL. Fig. 2.38 shows the snow cover for the reference at 12 UTC, so we can assume that a part of the total lost energy is due to the sublimation of snow. The atmospheric stability and turbulence situation is described in more detail in Paths 9 and 10 above.

Due to weaker turbulence and the lower surface temperature, the surface latent heat flux is lower which can be seen when comparing Fig. 2.25 and Fig. 2.30. The lower surface temperature helps with the reduction of the surface latent heat flux because the snow sublimation decreases with lower temperature.

Path 13 The reduction of the turbulent moisture transport is the reason for the drying of the six lowest model levels (approx. 990–1010 hPa). This can be seen in Fig. 2.35 where the turbulence contribution is shown by dark red colour. However, one can also see a partial compensation done by the advection (yellow), so the tendency for the lowest part of the atmosphere is only -0.1 g/kg/day.

Path 14, 15 Fig. 2.39 shows the evolution of domain averaged temperature of the deep soil layer (shortly deep temperature) for the reference and the experiment. When comparing it to the evolution of the surface temperature in Fig. 2.36, note how it is phase-shifted by 2–4 hours and its diurnal variability is much lower, only 1.3 K compared to 7.0 K for the surface temperature.

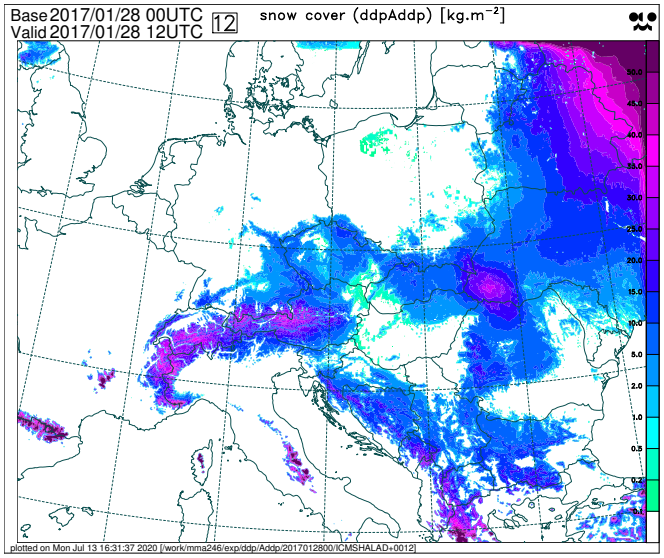

Figure 2.38: Snow cover (in kg/m^2) for the reference on 28.1.2017, 12 UTC. Integration starts on 28.1.2017, 0 UTC.

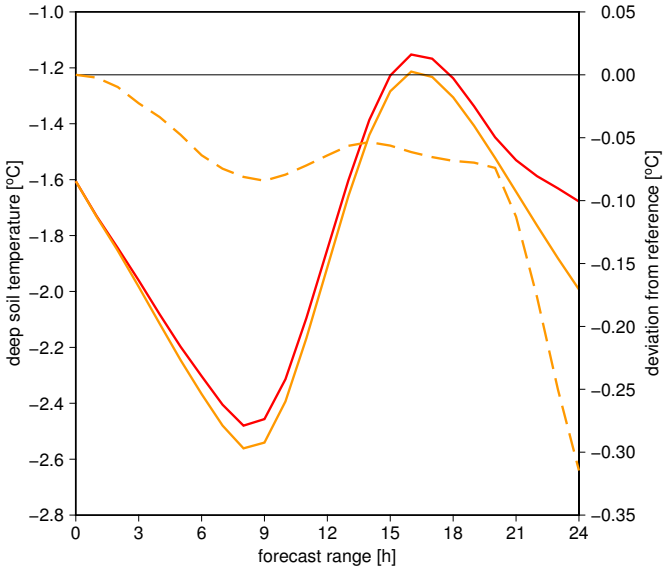

Figure 2.39: Evolution of domain averaged deep temperature (in °C) for the experiment with parametrized gravity waves (orange), the reference (red) and their difference (dashed). Integration starts on 28.1.2017, 0 UTC. The image contains two scales. The left scale is for reference and experiment values, and the right scale is for their difference.

The evolution equation of the deep temperature is using the so-called force-restore method (Blackadar, 1976). In this method, the ground is split into two layers: a thin top layer (the surface) and a deep layer. The method states that the soil heat flux tends to restore the surface layer, opposing the radiative forcing. The evolution of the deep temperature is expressed as

$$\frac{\partial T_d}{\partial t} = \frac{1}{\tau}\left(T_s - T_d\right) \tag{2.28}$$

where T_d is the deep temperature, T_s is the surface temperature and τ is the length of the day in seconds.

The soil heat flux is proportional to the difference of the surface and deep temperatures. That means, the surface is losing energy via the soil heat flux during the day when the surface is sufficiently heated ($T_s > T_d$); the opposite applies during the night. We can see this in Fig. 2.25 where the soil heat flux is mostly positive except near 13 UTC.

2.2.5 Verification

Verification of this experiment is done for only one 72 hour integration, which starts on 28th January 2017 at 0 UTC, with a time step of 6 hours. Although the verification period is short, it still provides a useful piece of information about the experiment and its reference when both are compared to observations. We will show only biases (BIAS) and standard deviations (STDE) because root mean squared errors (RMSE) can be easily calculated using the equation (2.3).

Because the verification is done for one model run, the statistical significance of both verification statistics (BIAS, STDE) will not be evaluated and we will confine ourselves only to the "meteorological significance", i.e. to analyze a response of the verification scores due to modifications in the model setup.

Fig. 2.40 shows the evolution of both verification scores (BIAS, STDE) with the forecast range for near-surface parameters. Positive BIAS of temperature at 2 m is reduced for the full forecast range. Positive BIAS of wind direction at 10 m is also reduced for almost the full forecast range. However, negative BIAS of wind speed at 10 m is increased which means that the GWD parametrization slows down the near-surface wind too much. It can be seen that STDE of all three parameters is slightly increased which indicates that the GWD parametrization is not properly tuned for the use on the horizontal resolution of 2.3 km.

The verification of parameters at height (not shown) is as follows. Negative BIAS of temperature is slightly reduced for pressure levels near 700 hPa but increased for those near 850 hPa. STDE of temperature does not change much for all pressure levels. The impact on wind speed is neutral.

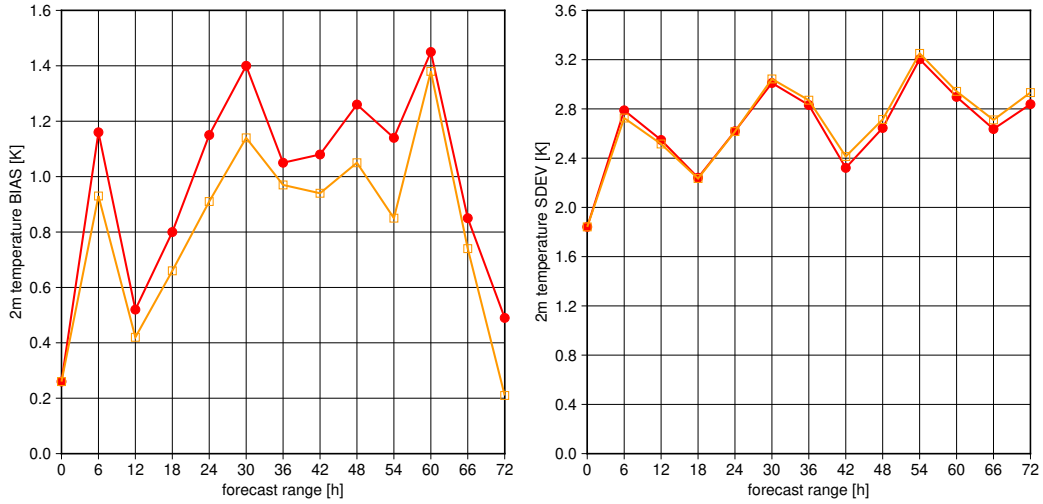

(a) BIAS of temperature at 2 m.

(b) STDE of temperature at 2 m.

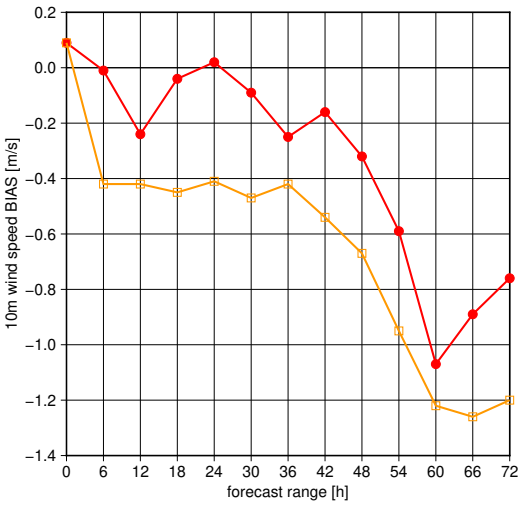

(c) BIAS of wind speed at 10 m.

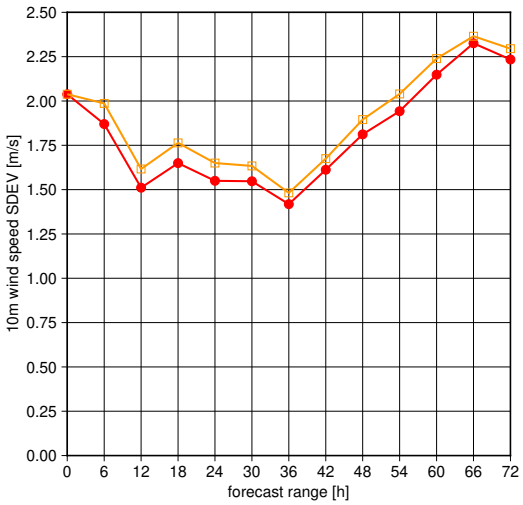

(d) STDE of wind speed at 10 m.

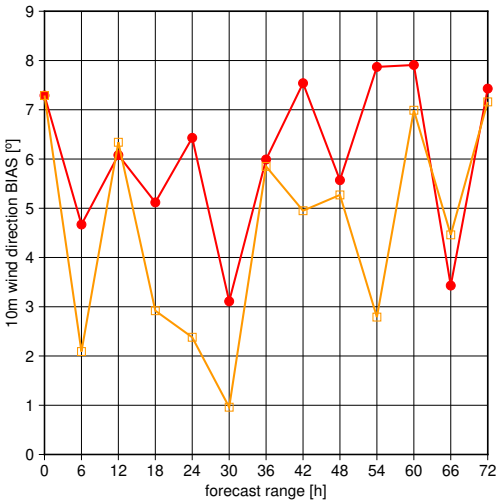

(e) BIAS of wind direction at 10 m.

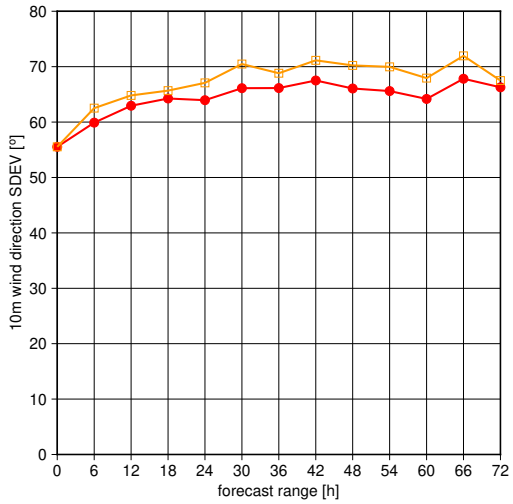

(f) STDE of wind direction at 10 m.

Figure 2.40: Evolution of verification scores with the forecast range for the experiment with parametrized gravity waves (orange) and the reference (red). Verification is done for one 72 hour forecast which starts on 28.1.2017, 0 UTC.

2.2.6 Conclusion

This experiment was characterized by the activation of the GWD parametrization with its tuning taken from the model version used with the horizontal resolution of 4.7 km. The lift parametrization remained disabled. A direct consequence of this setup was the reduction of wind speed at 10 m over almost the entire model domain as seen in Fig. 2.26.

The domain averaged wind speed was reduced at almost all model levels which was shown in Fig. 2.27. However, there were approx. ten model levels where the wind speed was increased. That happened due to the wind veering more than 90° compared to the near-surface wind.

The changes in the wind velocity were reflected via several feedback loops which were illustrated by the diagram in Fig. 2.29. We described them and supplemented the domain averaged evolution and vertical profile graphs and also outputs from DDH to understand the physical processes.

The dominant process which influenced temperature at 2 m was the change in sensible heat flux at 0–9 UTC and 15–24 UTC due to more stable conditions between the surface and the lowest model level, and due to slower wind at 10 m (caused by the activation of the GWD parametrization).

The experiment was verified on one day for the full 72 hour integration. It was enough to confirm the decrease in the screen-level temperature at 2 m and in wind speed at 10 m. This experiment showed a suitable improvement in the bias of the temperature at 2 m. However, the bias of the wind speed at 10 m was more negative and standard deviations of several other parameters were increased which indicates that the tuning taken from the model version used with the horizontal resolution of 4.7 km makes the scheme too active on the horizontal resolution of 2.3 km.

This experiment has shown that for further development, it is possible to keep the GWD parametrization activated, but it is needed to lower its impact via additional tuning. However, as the horizontal resolution is getting finer, gravity waves will be fully resolved and the GWD parametrization will be no longer required and should be disabled in the future.

With the transition to the horizontal resolution of 2.3 km, the elevation dataset is progressively updated. The older elevation dataset Global Topographic Data with a horizontal grid spacing of 30″ (GTOPO30) is being replaced by the newer dataset GMTED2010 (Global Multi-resolution Terrain Elevation Data 2010) which has the horizontal resolution of 7.5″. During the experiment, both datasets were used together: GMTED2010 for the grid-scale orography and GTOPO30 for the subgrid-scale characteristics, such as the standard deviation of the subgrid-scale orography h, and the anisotrophy and the orientation of the subgrid-scale orography. However, the qualitative results remain unchanged even when using only GMTED2010 for both grid-scale and subgrid-scale characteristics.

2.3 Overestimated minimum temperature case

In the ALADIN model, minimum night-time temperatures can be significantly overestimated at some places, especially in winter and spring. A spring case

example happened at the Doksany station on 20th April 2019 where ALADIN overstated the minimum night-time temperature by more than 5 °C. A winter case example occurred at the Kocelovice station on 20th January 2017 where ALADIN overstated the minimum night-time temperature by more than 7 °C. Both stations are located in the Czech Republic.

Mostly in winter, the main problem with these extreme cases of overstating minimum temperatures is an absence of warnings that are issued to warn against potential hazards and to prevent possible property damage. The aim of this section is to determine what influences the overestimated minimum night-time temperatures.

In the next sub-sections, we will describe in more detail the ISBA scheme (Noilhan and Planton, 1989b) which is a parametrization of surface processes in ALADIN. Next, a temperature sensitivity to changes of the thermic coefficient will be discussed and a modified soil heat flux formula will be introduced.

2.3.1 Relevant parametrizations

2.3.1.1 Surface parametrization

The ISBA scheme (Noilhan and Planton, 1989b) is used in ALADIN to parameterize the surface processes. Its main task is to model thermal and hydrous properties of the soil (which depend on its composition and water content), thermal inertia of the vegetation and its ability to immediately evaporate precipitation it intercepts, the surface evaporation, and the heat and moisture exchange between the surface and deep soil layer.

The soil and vegetation are characterized by various variables. For example, two of several variables determining the soil are a clay and a sand content, and two of a variety of variables describing the vegetation are a leaf-area index (a leaf surface area per unit soil surface area) and the vegetation height type (high or low). The soil is split to two layers: a thin top surface layer and a deep layer as can be seen in Fig. 2.2.

The evolution of deep soil temperature (shortly deep temperature) is given by the so-called force-restore method (Blackadar, 1976). It is expressed as

$$\frac{\partial T_d}{\partial t} = \frac{1}{\tau}\left(T_s - T_d\right) \tag{2.29}$$

where T_d is the deep temperature, T_s is the surface temperature and τ is the length of the day (86 400 seconds).

In the absence of freezing or melting of soil water, the evolution of the surface temperature is given by

$$\frac{\partial T_s}{\partial t} = C_T\left(Q_{\mathrm{R}} + Q_{\mathrm{sens}} + Q_{\mathrm{lat}} - F_{\mathrm{sp}}\right) \tag{2.30}$$

where C_T is the thermic coefficient (in $\mathrm{K\,m^{-2}\,J^{-1}}$), Q_{R} is the surface net radiation flux, Q_{sens} is the surface sensible heat flux, Q_{lat} is the surface latent heat flux and F_{sp} is the heat flux between the surface and deep soil (shortly soil heat flux). The soil heat flux F_{sp} is expressed as

$$F_{\mathrm{sp}} = \frac{1}{C_T}\frac{2\pi}{\tau}\left(T_s - T_d\right)\ . \tag{2.31}$$

The thermic coefficient C_T is defined as

$$\frac{1}{C_T} = (1 - f_{\text{veg}}) \frac{1}{C_G} + f_{\text{veg}} \frac{1}{C_V} \tag{2.32}$$

where f_{veg} is the vegetation fraction, C_G is the bare ground thermic coefficient (in $\mathrm{K\,m^{-2}\,J^{-1}}$) and C_V is the vegetation thermic coefficient (in $\mathrm{K\,m^{-2}\,J^{-1}}$). The vegetation thermic coefficient C_V is different for low and high vegetation and its values are given in Table 2.5. The bare ground thermic coefficient C_G can be expressed as

$$C_G = C_{G_{\text{sat}}} f(W) \tag{2.33}$$

where $f(W)$ is a function of the total liquid soil water W and $C_{G_{\text{sat}}}$ is the bare ground thermic coefficient at saturation which is computed as

$$C_{G_{\text{sat}}} = \text{G1CGSAT} \cdot \text{sab} + \text{G2CGSAT} \cdot \text{arg} + \text{G3CGSAT} \tag{2.34}$$

where G1CGSAT, G2CGSAT and G3CGSAT are tuning parameters given in Table 2.5, and sab and arg are percentages of sand and clay in the gridbox, respectively. Finally, the bare ground thermic coefficient C_G is limited by the value of $C_{G_{\max}}$ which is given in Table 2.5.

Parameter	Value	Units
G1CGSAT	-1.6×10^{-8}	$\mathrm{K\,m^{-2}\,J^{-1}}$
G2CGSAT	-1.4×10^{-8}	$\mathrm{K\,m^{-2}\,J^{-1}}$
G3CGSAT	4.7×10^{-6}	$\mathrm{K\,m^{-2}\,J^{-1}}$
$C_{G_{\max}}$ (RCGMAX)	0.8×10^{-5}	$\mathrm{K\,m^{-2}\,J^{-1}}$
C_V for low vegetation (RCTVEG(3))	1.4×10^{-5}	$\mathrm{K\,m^{-2}\,J^{-1}}$
C_V for high vegetation (RCTVEG(4))	1.1×10^{-5}	$\mathrm{K\,m^{-2}\,J^{-1}}$

Table 2.5: Tuning parameters used in the ISBA scheme.

2.3.1.2 Surface temperature sensitivity to thermic coefficient changes

The temperature tendency is proportional to the surface soil layer thermic coefficient C_T as can be seen in the equation 2.30. It may seem reasonable that a change of the thermic coefficient C_T would have a symmetric impact on minimum and maximum temperatures. However, the thermic coefficient C_T has no influence on surface temperature when the surface budget is zero. There is a feedback between the thermic coefficient C_T and the surface budget.

In this section, we will present that the change is in fact asymmetric even in a simple model. We will see the same behaviour later when discussing the overestimated minimum temperatures in ALADIN.

To illustrate this asymmetric behaviour, we will use a simple 3-layer model of atmosphere and soil. Its scheme is shown in Fig. 2.41. The atmosphere is represented only by PBL, the soil is divided into two layers (the surface soil layer and the deep soil layer) as in ALADIN. The arrows show surface shortwave net radiation flux, surface longwave net radiation flux, soil heat flux, and surface sensible heat flux which are denoted as SW, LW, SH and M, respectively. The

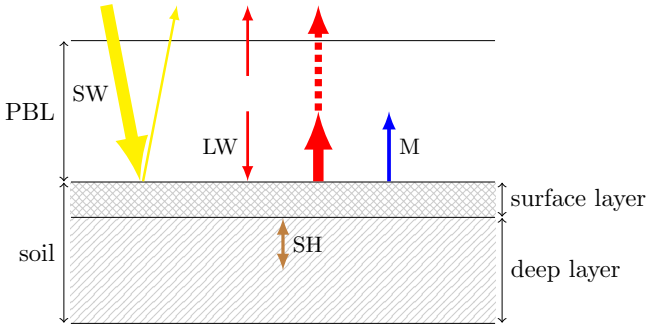

Figure 2.41: Scheme of the 3-layer surface-atmospheric model with associated fluxes. The arrow thickness corresponds to the relative ratios of the absolute daily averaged flux values.

arrow thickness corresponds to the relative ratios of the absolute daily averaged flux values.

The 3-layer model is constructed as follows. The shortwave radiation forcing is given by a truncated cosine function, the atmosphere is fully transparent in the shortwave spectrum, the surface behaves as a black body in the longwave spectrum, the surface albedo is 0.2 and the soil heat flux is given by the force-restore method (Blackadar, 1976). PBL accounts for 10 % of the atmosphere mass. The surface sensible heat flux from surface to PBL is proportional to the difference of potential temperature between the surface and the middle of PBL, with the proportionality constant of $30\,\mathrm{W\,m^{-2}\,K^{-1}}$. It is not zero only in unstable conditions. Evolution equations for the temperatures of the three layers are discretized explicitly with the timestep of 60 s.

Fig. 2.42 shows the evolution of surface energy budget and associated fluxes for the 3-layer model where $C_T = 0.8{\times}10^{-5}\,\mathrm{K\,m^{-2}\,J^{-1}}$ (reference). The surface energy budget is denoted as sum. After the transition phase, a periodic diurnal pattern settles down.

Fig. 2.43 shows the evolution of surface temperature for the 3-layer model with $C_T = 1.0{\times}10^{-5}\,\mathrm{K\,m^{-2}\,J^{-1}}$ (experiment) and $C_T = 0.8{\times}10^{-5}\,\mathrm{K\,m^{-2}\,J^{-1}}$ (reference). The asymmetric change of maximum and minimum surface temperatures is clearly visible. Temperature at 2 m is not available in the 3-layer model, but its diurnal evolution would follow surface temperature with a reduced amplitude.

Gradual construction of the 3-layer model has shown that the surface sensible heat flux is responsible for the mentioned asymmetry which is missing when the surface sensible heat flux parametrization is off. Thus, a small change in the maximum temperature compared to the large change in the minimum temperature is caused by the heat transfer from the surface to the atmosphere during the day. Meanwhile, the atmosphere is losing its energy via longwave radiation into space.

2.3.1.3 Modified soil heat flux parametrization

There is an assumption in the ISBA scheme that the surface soil layer and snow cover have the same temperature. This assumption is not realistic, especially with a thick snow cover, as snow limits the heat exchange between the atmosphere and the soil, and it enables a development of a sharp temperature gradient between

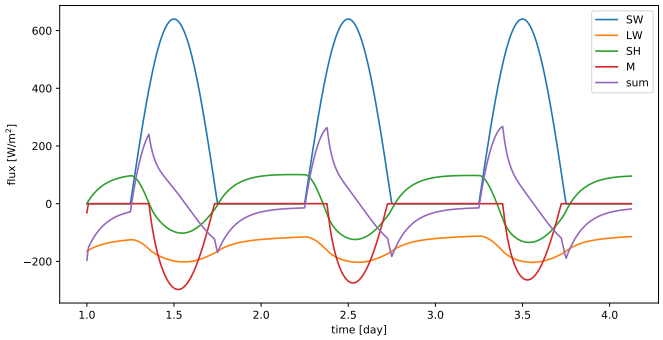

Figure 2.42: Evolution of surface energy budget and associated fluxes (in $\mathrm{W/m^2}$) for the 3-layer model reference where $C_T = 0.8{\times}10^{-5}\,\mathrm{K\,m^{-2}\,J^{-1}}$. Integration starts at 0 UTC.

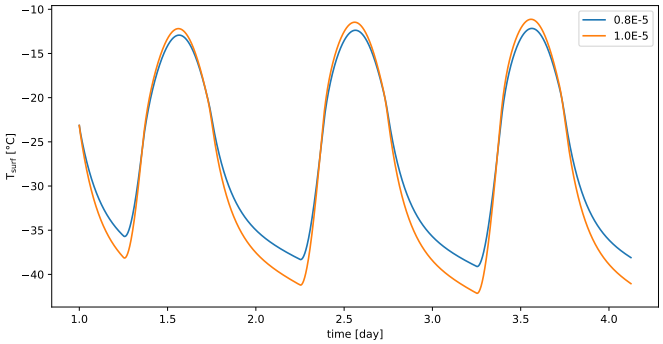

Figure 2.43: Evolution of surface temperature (in °C) for the 3-layer model experiment where $C_T = 1.0{\times}10^{-5}\,\mathrm{K\,m^{-2}\,J^{-1}}$ (orange) and the reference where $C_T = 0.8{\times}10^{-5}\,\mathrm{K\,m^{-2}\,J^{-1}}$ (blue). Integration starts at 0 UTC.

soil and the snow skin layer. It is a skin temperature that affects turbulence and determines longwave surface emission. However, for the energy budget, the average layer temperature is relevant.

It is possible to reduce the computed soil heat flux when snow cover is present. However, that does not retain the original formula of the force-restore method (the equation 2.31). In addition, the surface temperature will no longer represent the surface soil layer, but only the skin layer of snow (and the vegetation above it), which is also an unrealistic characteristics (Mašek, 2017).

Then, the modified soil heat flux can be expressed as

$$F_{\mathrm{sp}} = \frac{1}{C_T}\frac{2\pi}{\tau}\left[1 - \left(f_{\mathrm{snow}}^{\mathrm{bg}}\right)^n\right](T_s - T_d) \tag{2.35}$$

where $f_{\mathrm{snow}}^{\mathrm{bg}}$ is the fraction of the bare ground covered by snow and n is a tuning parameter. Note that the modification is only experimental and it has never been used in any ALADIN operational version.

2.3.2 Reference experiments

There are two reference experiments described in this section, one for the spring case and another for the winter case. Both are based on the CHMI version

CY43T2plus_op1. They are used as baselines and later experiments will be compared to them.

2.3.2.1 Spring case

The overestimation of the minimum temperature can happen in the spring when snow cover is not present. To describe the overestimation in such case, the start of the integration is chosen on 19th April 2019 at 0 UTC. The studied domain is reduced to one point, the professional meteorological station Doksany in the Czech Republic which is located at (50.47°N, 14.17°E).

Fig. 2.44a shows the evolution of 2 m temperature at the Doksany station. The overestimation of minimum temperatures happen during all nights and it is up to 5 °C. However, maximum temperatures are predicted well. Note the weather situation, the maximum temperatures reach more than 20 °C, but the minimum temperatures are close to 0 °C. In Fig. 2.45a, it can be seen that the snow cover is absent. Thus, it does not influence the overestimation of minimum temperatures.

2.3.2.2 Winter case

During winter, when significant snow cover is present, an overestimation of the minimum temperature is likely to happen. To study the overestimation in this case, the start of the integration is chosen on 20th January 2017 at 12 UTC. We will be looking at the professional meteorological station Kocelovice in the Czech Republic which is located at (49.47°N, 13.83°E).

Fig. 2.44b shows the evolution of 2 m temperature at the Kocelovice station. Similarly to the spring case, the overestimation is present during all nights and it is up to 7 °C. The maximum temperature values are predicted with an error less than 1 °C.

The start of integration date is selected due to following criteria: the model and observations have clear sky or very few clouds, and there is a thick snow cover both in the model ($6\,\mathrm{kg\,m^{-2}}$ for the Kocelovice station) and in observations ($16\,\mathrm{kg\,m^{-2}}$ for the Kocelovice station). Fig. 2.45b shows the snow cover for the model domain. The thick snow cover is essential to limit the soil heat flux and the clear sky eliminates the influence of clouds on the daily temperature variation.

2.3.3 Experiments

The main characteristics of these experiments are a tuning of thermic coefficients in the spring case and a modification of soil heat flux computation in the winter case. We use the CHMI model version CY43T2plus_op1. We will look at differences between these experiments and the references described in Section 2.3.2.

2.3.3.1 Spring case

There are two changes in the model setup compared to the reference:

1. set RCTVEG(3) from 1.4E-5 to other values (the modification of the thermic coefficient C_V for low vegetation),

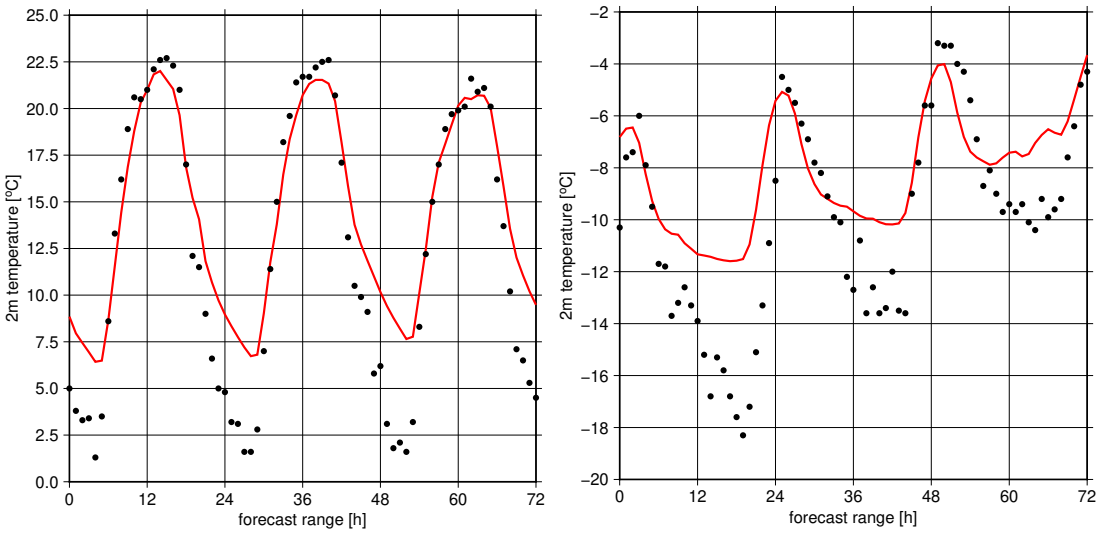

(a) Doksany station. Integration starts on 19.4.2019, 0 UTC.

(b) Kocelovice station. Integration starts on 19.1.2017, 12 UTC.

Figure 2.44: Evolution of 2 m temperature (in °C) for the references (red) and observations (black dots).

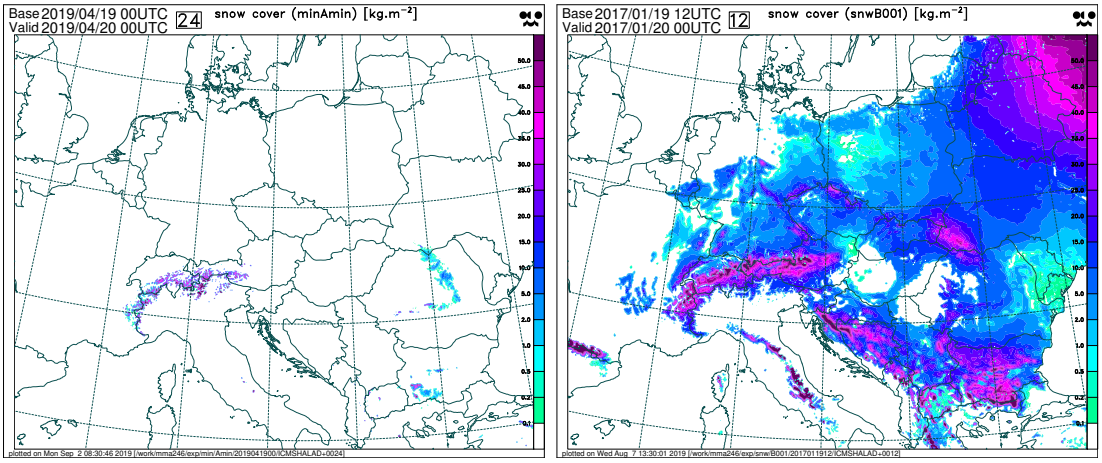

(a) 20.4.2019, 0 UTC. Integration starts on 19.4.2019, 0 UTC.

(b) 20.1.2017, 0 UTC. Integration starts on 19.1.2017, 12 UTC.

Figure 2.45: Snow cover (in $\mathrm{kg\,m^{-2}}$) for the references.

2. set RCTVEG(4) from 1.1E-5 to other values (the modification of the thermic coefficient C_V for high vegetation).

Fig. 2.46a shows the evolution of temperature at 2 m with one reference and several experiments which tune the thermic coefficient C_V for vegetation. One can see that when the thermic coefficient C_V is higher, the model values better represent observations.

The results using $C_V = 9\times10^{-5}\,\mathrm{K\,m^{-2}\,J^{-1}}$ for both low and high vegetation are as follows. Minimum night-time temperatures have now error of just approx. 2 °C. Maximum day-time temperatures correspond better to the observations as well, the error is approx. 0.1 °C even on the third day of integration. It can be seen that the changes of temperature at 2 m correspond qualitatively

to those described in Section 2.3.1.2 illustrated in Fig. 2.43. The equation (2.32) does not allow C_T to be higher than $C_G/(1 - f_{\mathrm{veg}})$ which is $3.0{\times}10^{-5}\,\mathrm{K\,m^{-2}\,J^{-1}}$ for the Doksany station.

However, such changes in the evolution of 2 m temperature can be also made by setting LIMC from .T. to .F. which switches off the limitation of the bare ground thermic coefficient C_G to the value of $C_{G_{\mathrm{max}}}$. In this case, it is enough to set $C_V = 3{\times}10^{-5}\,\mathrm{K\,m^{-2}\,J^{-1}}$ which is 3x less then the value described in the previous paragraph and therefore, closer to the default value. However, this approach can be numerically unsafe and should not be used except for testing purposes.

The third option how to get the evolution of temperature at 2 m similar to that in Fig. 2.46a, is to set RCGMAX to a higher value. Then, the bare ground thermic coefficient C_G is still limited up to the value of $C_{G_{\mathrm{max}}}$ which would be, however, higher. The intention of the last two methods was to increase the thermic coefficient C_T via C_G.

2.3.3.2 Winter case

There is only one change in the model setup compared to the reference:

1. set RCHSP from 0 (corresponding to $n = \infty$) to other values (the modification of the tuning parameter n in the equation (2.35)).

Fig. 2.46b shows the evolution of temperature at 2 m with one reference and several experiments which modify the tuning parameter n. It can be seen that lower n helps to reduce the 2 m temperature in general. However, the match with observations is not particularly improved when compared to the spring case. There was less snow in the model, we have no information about the real snow fraction, albedo, etc. Thus, the winter case is more difficult to improve. The results using $n = 1$ are as follows. Minimum night-time temperatures are close to observations only for the second night. Maximum day-time temperatures are lower with lower n and they have a worse agreement with observations when compared to the reference.

2.3.4 Conclusion

These experiments were characterized by the tuning of the thermic coefficient C_V for vegetation, the bare ground thermic coefficient C_G, and the coefficient n (the equation (2.35)) for the spring case and for the winter case, respectively.

In the spring case, temperature at 2 m agreed well with observations for higher values of the thermic coefficient C_V for vegetation as was presented in Fig. 2.46a. These changes qualitatively correspond to those described for the 3-layer model in Section 2.3.1.2 and showed in Fig. 2.43. In the winter case, temperature at 2 m was lower with a lower tuning parameter n as could be seen in Fig. 2.46b. However, lower n decreases also maximum temperatures which is not desirable. Minimum night-time temperatures agreed well ($n = 1$) with observations for the second night only.

Verification scores were not included, since the error for the single station is sufficiently illustrated by Fig. 2.44 and 2.46. For the spring case, the tuning works

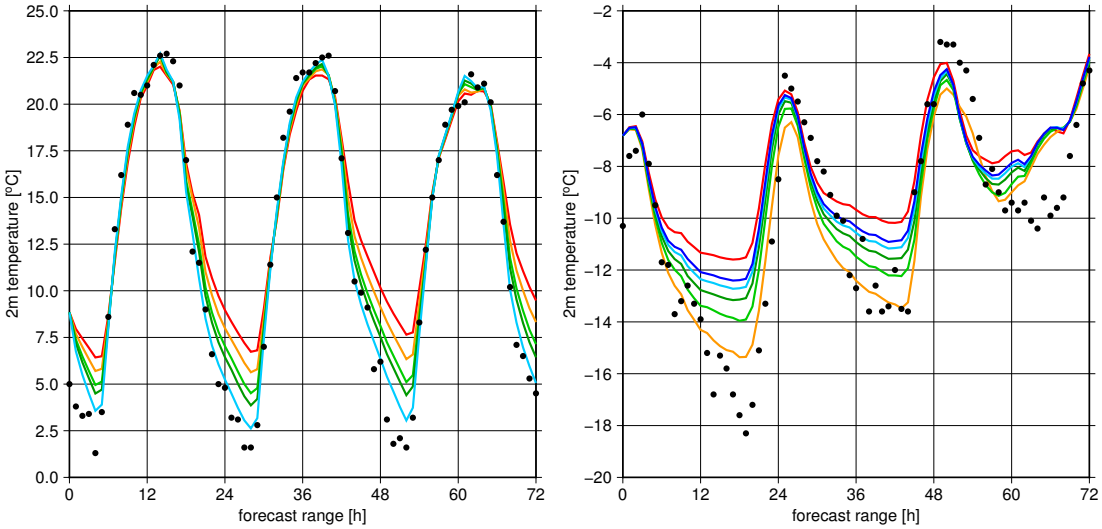

(a) Doksany station. Experiment with $C_V = 2{\times}10^{-5}\,\mathrm{K\,m^{-2}\,J^{-1}}$ (orange), $C_V = 3{\times}10^{-5}\,\mathrm{K\,m^{-2}\,J^{-1}}$ (light green), $C_V = 4{\times}10^{-5}\,\mathrm{K\,m^{-2}\,J^{-1}}$ (dark green) and $C_V = 9{\times}10^{-5}\,\mathrm{K\,m^{-2}\,J^{-1}}$ (light blue). Thermic coefficients for low and high vegetation are the same, except in the reference (red) where $C_V = 1.4{\times}10^{-5}\,\mathrm{K\,m^{-2}\,J^{-1}}$ for low vegetation and $C_V = 1.1{\times}10^{-5}\,\mathrm{K\,m^{-2}\,J^{-1}}$ for high vegetation. Integration starts on 19.4.2019, 0 UTC.

(b) Kocelovice station. Experiment with $n = 1$ (orange), $n = 1.5$ (light green), $n = 2$ (dark green), $n = 2.5$ (light blue) and $n = 3$ (dark blue), and the reference with $n = \infty$ (red). Integration starts on 19.1.2017, 12 UTC.

Figure 2.46: Evolution of 2 m temperature (in °C) for experiments (orange, light green, dark green, light blue, dark blue), the references (red) and observations (black dots).

well for Doksany, but minimum night-time temperatures are underestimated for some stations nearby. This can be due to a strong variation of local soil/vegetation characteristics. Moreover, STDE is worsened when verifying this tuning settings in the winter. For the winter case, the experimental modification of the soil heat flux via the tuning parameter n does not work well due to lower maximum day-time temperatures and a varying impact on minimum night-time temperatures. These experiments have shown that

1. for accurate predictions of 2 m temperature, quality of high resolution physiography datasets is uttermost important,
2. in winter, we need more sophisticated snow scheme discriminating between soil and snow temperatures.

3. Influence of screen level interpolation on 2m temperature

In this chapter, we will cover how modifications in the 2 m temperature interpolation (also called screen level interpolation) implemented in the regional climate model RegCM affect the modelled 2 m temperature while using two different PBL parametrization schemes.

We will describe relevant parametrizations in more detail, introduce the reference experiments (or shortly "references") and additional experiments with changed parameters that will be compared to the references. To begin, a description of the model domain and the configuration which will remain the same through all experiments follows.

Fig. 3.1 shows the RegCM/CE12 model domain with orography on which all experiments are computed. The model uses a horizontal resolution of 12.0 km and only 23 levels in the vertical. Due to the relatively low horizontal resolution, the model is run with hydrostatic dynamics. A Lambert conformal projection is used with a tangent latitude of 48.6°N and a reference longitude of 14.9°E.

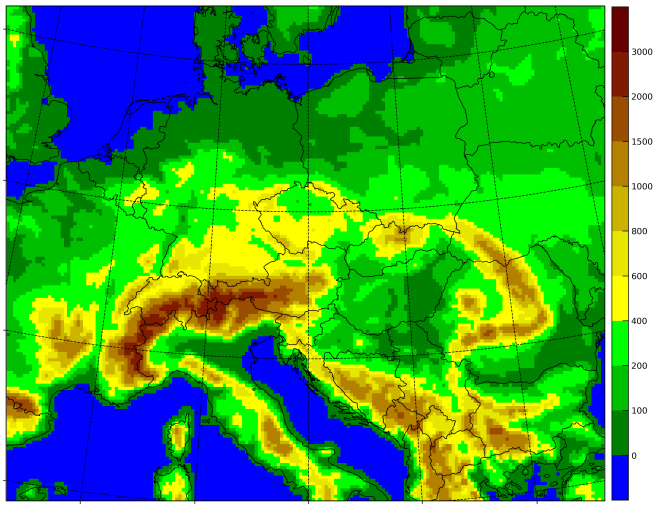

Figure 3.1: The RegCM/CE12 model domain with the resolved orography (in meters) used for all experiments.

A vertical mass-based coordinate σ is used (Grell et al., 1994). Horizontal discretization uses a staggered Arakawa B-grid which separates thermodynamical and wind variables. The model level numbers are decreasing with an increasing height. Full levels are numbered from 1 to $L = 23$ which is the lowest full model level, half levels are numbered from $\tilde{1}$ to $\tilde{L} = 24$ corresponding to surface. The average distance between the surface and the lowest full model level is 76 m. Physical quantities treated by the parametrizations are associated with full model levels, unless stated otherwise. A quantity associated with specific level (for example a level l) will have this level specified in the lower index. If the quantity is associated with the surface, the symbol s will be noted in the lower index instead of $\tilde{L}$. The physical quantities represent a gridbox average, if not stated otherwise, such as mentioning perturbations, subgrid-scale processes, etc.

In Table 3.1, there is an overview of full model levels in RegCM with their corresponding pressure and height above the ground based on the International Standard Atmosphere (ISA).

Model level	Pressure (hPa)	Height (m)
1	50	20 643
3	146	13 766
5	243	10 555
7	339	8337
9	435	6583
11	532	5119
13	628	3857
15	724	2743
17	821	1743
19	907	922
20	946	577
21	975	326
22	994	162
23	1004	80

Table 3.1: Full model levels in RegCM and their corresponding pressure (in hPa) and height above the surface (in meters) based on the International Standard Atmosphere (ISA).

Boxplots and domain averaged quantities are computed on several longitude-latitude rectangles which will be called "diagnostic domains". We will study the influence of changes in the screen level interpolation in three different European regions to see how the regional characteristics affect the results. Borders of individual regions are visualized in Fig. 3.2 and their description is as follows

- The Alpine region (ALP) with the left bottom corner at (44°N, 5°E) and the right upper corner at (48°N, 15°E),
- The Balkans (BAL) with the left bottom corner at (40.5°N, 18.5°E) and the right upper corner at (46.5°N, 27.5°E),
- Central Europe (CEU) with the left bottom corner at (48°N, 10°E) and the right upper corner at (52.5°N, 23°E).

To maintain readability, the term "domain averaged" will be often omit if it would have been repeated several times in a paragraph.

The scheme of the surface-atmosphere interface is similar to that in ALADIN (Fig. 2.2). Thus, its description will be omitted. A convention is that the net surface fluxes are positive upwards (from the surface). Note, that the RegCM convention is opposite compared to the convention used in ALADIN.

To evaluate the climate simulation of RegCM, modelled meteorological parameters are compared to the gridded observational dataset E-OBS (Cornes et al., 2018), version 22.0e, with a spatial resolution of 0.1° which will be considered as the atmospheric real state. RegCM model output is regridded to the E-OBS

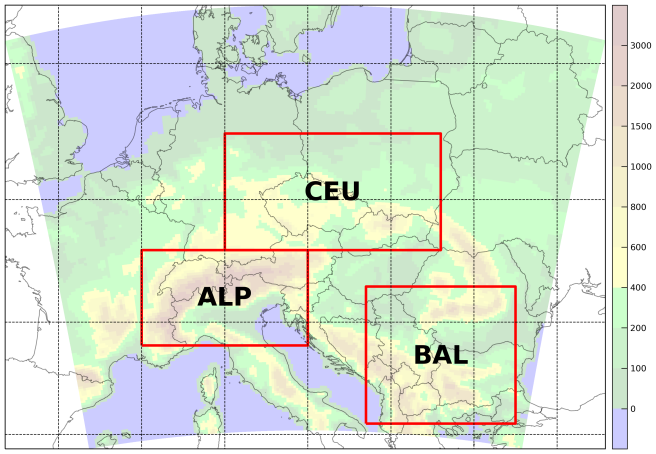

Figure 3.2: Diagnostic domains defined on the RegCM/CE12 model domain. Borders of a diagnostic domain are shown as red lines. The three diagnostic domains are: The Alpine Region (ALP), The Balkans (BAL) and Central Europe (CEU).

projection using bilinear interpolation. Multi-year seasonal statistical scores will be computed. Their definition is as follows

$$\mathrm{BIAS} = \frac{1}{N}\sum_{i=1}^{N}(F_i - O_i) \ , \tag{3.1}$$

$$\mathrm{STDE} = \sqrt{\frac{1}{N-1}\sum_{i=1}^{N}(F_i - O_i - \mathrm{BIAS})^2} \ , \tag{3.2}$$

where BIAS denotes mean error, STDE denotes standard deviation, N is the number of observations, O_i is the i-th observation and F_i is the i-th forecasted parameter.

3.1 ALADIN screen level interpolation case

To compare modelled temperature with surface observations, the model temperature has to be interpolated to the screen level height which is 2 m for temperature. Once the screen level temperature is obtained, the modelled temperature can be verified and thus, its forecast quality can be evaluated.

ALADIN was created as an operational NWP model which puts an emphasis on its computational efficiency and restricts the complexity of employed parametrization schemes. On the other hand, RegCM was constructed as a climate model which is generally run with a lower resolution. It can afford somewhat more complex parametrization schemes since their computational cost is not the main criterion.

The aim of this section is to replace the more detailed screen level interpolation in RegCM by the simpler screen level interpolation used in ALADIN and show if 2 m temperature estimation will change significantly. In the next sub-sections, we will describe in more detail the screen level interpolation used in ALADIN and RegCM to show the reader how they differ from each other.

3.1.1 Relevant parametrizations

To compare modelled temperature with surface observations, the temperature has to be estimated at the height of 2 m. Most often, it is interpolated to this height using the surface temperature and the lowest model level temperature. The interpolation is based upon the Monin-Obukhov similarity theory (Monin and Obukhov, 1954) due to strong temperature gradients near the surface.

The Monin-Obukhov theory describes non-dimensionalized mean velocity and mean temperature profiles in the surface layer under non-neutral conditions using two universal functions (called the stability functions) Φ_m for momentum and Φ_h for heat/moisture. However, the theory does not directly describe a temperature profile. Instead it uses potential temperature or dry static energy because the Monin-Obukhov equations apply only for meteorological variables which do not change during an adiabatic process. The stability functions depend on the dimensionless stability parameter

$$\zeta = \frac{z + z_0}{L} \tag{3.3}$$

where z is the height above surface, z_0 is the roughness length and L is the Monin-Obukhov length defined as

$$L = \frac{u_*^3 \theta_v \rho c_p}{\kappa g H} \tag{3.4}$$

where θ_v is the virtual potential temperature, ρ is the air density, c_p is the specific heat capacity for air at constant pressure, $\kappa \approx 0.4$ is the von Kármán constant, g is the gravitational acceleration, H is the sensible heat flux (with the ALADIN convention that the flux is positive downwards, towards the surface) and u_* is the friction velocity defined as

$$u_* = \sqrt[4]{\left(\overline{u'w'}\right)^2 + \left(\overline{v'w'}\right)^2} \tag{3.5}$$

where the bar indicates the averaging and u', v' and w' are the subgrid-scale perturbations of the respective mean values u, v and w describing the flow velocity. The potential temperature scale is defined as

$$\theta_* = \frac{H}{\rho c_p u_*} \ . \tag{3.6}$$

The Monin-Obukhov equation for mean wind is expressed as

$$\frac{\partial u}{\partial z} = \frac{u_*}{\kappa \left(z + z_{0m}\right)} \Phi_m \left(\frac{z + z_{0m}}{L}\right) \tag{3.7}$$

and the Monin-Obukhov equation for mean potential temperature is as follows

$$\frac{\partial \theta}{\partial z} = \frac{\theta_*}{\kappa \left(z + z_{0h}\right)} \Phi_h \left(\frac{z + z_{0h}}{L}\right) \tag{3.8}$$

where z_{0m} is the roughness length for momentum and z_{0h} is the roughness length for heat/moisture.

The Monin-Obukhov similarity theory does not provide stability functions itself, it only says that they should exist and should be universally applicable. Therefore, they are determined experimentally and fitted suitably. There is a certain freedom how to choose the form of stability functions. If we use Businger et al. (1971) stability functions which are generally accepted, Monin-Obukhov equations cannot be solved analytically. On the other side, if they are in a special form, Monin-Obukhov equations can be solved analytically, but the fit is usually a little less optimal. The Monin-Obukhov length L is positive in stable conditions, negative in unstable conditions and goes to infinity in neutral conditions. Stability functions are monotonic and they are one in neutral conditions (when L goes to infinity).

3.1.1.1 ALADIN screen level interpolation

For description of screen level temperature interpolation in ALADIN, we will be using Geleyn (1988) stability functions. The dry static energy $s = c_p T + gz$ is used in Monin-Obukhov equations in ALADIN instead of potential temperature θ. The Geleyn stability functions are

$$\Phi_{m/h}(\zeta) = \begin{cases} 1 + \alpha_G \zeta & \text{for } \zeta \geq 0 \text{ (stable)}, \\ \frac{1}{1-\alpha_G \zeta} & \text{otherwise (unstable)} \end{cases} \tag{3.9}$$

where α_G is a free parameter which is determined from the requirement that the given quantity (such as dry static energy) must match values at the surface and the lowest model level. An another free parameter is an integration constant which means there are two free parameters for two conditions.

The solution of Monin-Obukhov equations with Geleyn stability functions is an analytical profile of dry static energy s (and specific humidity q). Quantifying them at the height of 2 m yields

$$s_{2m} = s_s + w(s_L - s_s) \ , \tag{3.10}$$

$$q_{2m} = q_s + w(q_L - q_s) \tag{3.11}$$

where $s_s = c_{p_s} T_s$ is the dry static energy at the surface, $s_L = c_{p_L} T_L + g z_L$ is the dry static energy at the lowest model level, T_s is the surface temperature (which is the same for bare ground, vegetation and snow), T_L is the lowest model level temperature, z_L is the height above surface of the lowest model level and the specific heat capacities at constant pressure are expressed as

$$c_{p_s} = c_{pd} + q_s(c_{pv} - c_{pd}) \ , \tag{3.12}$$

$$c_{p_L} = c_{pd} + q_L(c_{pv} - c_{pd}) \tag{3.13}$$

where c_{pd} is the specific heat capacity of dry air at constant pressure, c_{pv} is the specific heat capacity of water vapour at constant pressure, q_s is the specific humidity at the surface and q_L is the specific humidity at the lowest model level.

The weight w for stable conditions is given by

$$w = \frac{1}{b_H} \left[\log\left(1 + \frac{z_{2m}}{z_{oh}}\right) - \frac{z_{2m}}{z_L}(b_{HN} - b_H) \right] \tag{3.14}$$

and for unstable conditions, it is expressed as

$$w = \frac{1}{b_H}\left[\log\left(1+\frac{z_{2m}}{z_{oh}}\right) - \log\left(1+\frac{z_{2m}}{z_L}\left(\mathrm{e}^{b_{HN}-b_H}-1\right)\right)\right] \tag{3.15}$$

where $z_{2m} = 2\,\mathrm{m}$. The exchange coefficient b_H and the exchange coefficient at neutrality b_{HN} are calculated as

$$b_H = \kappa\frac{s_L - s_s}{s_*}\ , \tag{3.16}$$

$$b_{HN} = \log\left(1+\frac{z_L}{z_{0h}}\right) \tag{3.17}$$

where log is the natural logarithm and $z_{oh} = z_{0m}/10$ is the roughness length for heat. The roughness length for momentum z_{0m} used in the computation of z_{0h} has a micrometeorological value because orography with a small slope does not affect turbulent exchange of heat and moisture (Hewer and Wood, 1998). The dry static energy scale is defined as

$$s_* = \frac{H}{\rho_L u_*} \tag{3.18}$$

where ρ_L is the air density at the lowest model level.

Finally, temperature at 2 m is calculated using 2 m dry static energy and 2 m specific humidity as

$$T_{2m} = \frac{1}{c_{p,2m}}\left(s_{2m} - gz_{2m}\right) \tag{3.19}$$

where the specific heat capacity at 2 m at constant pressure $c_{p,2m}$ is calculated as

$$c_{p,2m} = c_{pd} + q_{2m}(c_{pv} - c_{pd})\ . \tag{3.20}$$

The Geleyn solution in ALADIN was replaced with more accurate solutions over time, but the screen level interpolation mechanism is well explained on it. Note that stability functions in ALADIN are different for screen level interpolation and turbulence which is treated by TOUCANS parametrizations (described more in Section 1.3). The analytical solution of screen level interpolation with different stability functions than in turbulence was preferred over a consistent iterative solution due to lower computational cost and modularity.

3.1.1.2 RegCM screen level interpolation

The RegCM screen level temperature interpolation is more complex than in ALADIN and it is thoroughly described by Oleson et al. (2013) and it is also based on Monin-Obukhov equations. Stability functions from RegCM turbulence scheme are used consistently also in screen level interpolation. Therefore, iterative solution of Monin-Obukhov equations is necessary.

Temperature at 2 m is computed as

$$T_{2m} = \theta_s + \frac{\theta_*}{\kappa}\left[\log\left(\frac{z_{2m}+z_{0h}}{z_{0h}}\right) - \Psi_h\left(\frac{z_{2m}+z_{0h}}{L}\right) + \Psi_h\left(\frac{z_{0h}}{L}\right)\right] \tag{3.21}$$

where θ_s is the potential temperature at the surface (for bare ground and lakes) or inside canopy space (for canopy) and Ψ_h is the integrated stability function for heat which is expressed as

$$\Psi_h(\zeta) = \int_{\frac{z_{0h}}{L}}^{\zeta} \frac{1 - \Phi_h(x)}{x} \, \mathrm{d}x \tag{3.22}$$

where $\Phi_h(\zeta)$ is the stability function for heat. It is defined according to Zeng et al. (1998) as

$$\Phi_h(\zeta) = \begin{cases} 0.9\kappa^{4/3} \left(-\zeta\right)^{-1/3} & \text{for } \zeta < -0.465 \text{ (very unstable)}, \\ \left(1 - 16\zeta\right)^{-1/2} & \text{for } -0.465 \leq \zeta < 0 \text{ (unstable)}, \\ 1 + 5\zeta & \text{for } 0 \leq \zeta \leq 1 \text{ (stable)}, \\ 5 + \zeta & \text{for } \zeta > 1 \text{ (very stable)} \ . \end{cases} \tag{3.23}$$

During the iterative solution, potential temperature at the lowest model level θ_L is also needed.

3.1.2 Reference experiments

There are two reference experiments described in this section which share the same model configuration except the used PBL parametrization scheme. Both are based on the RegCM version 4.6.1 with the land surface model CLM4.5 (described more in Section 1.3). They are used as baselines and later experiments will be compared to them.

The two PBL parametrization schemes chosen for the references are

- the Holtslag scheme (Holtslag et al., 1990),
- the UW-PBL scheme (University of Washington; Bretherton et al., 2004).

Their main differences were described in Section 1.3 and we will not be describing them furthermore.

To study the influence of screen level interpolation on temperature at 2 m, the start of the integration is chosen on 1st January 2011 at 0 UTC. The integration ends on 1st January 2014 at 0 UTC and the model spin-up period is the first year, so the data from the year 2011 will not be later used. Boundary conditions are taken from the ERA-Interim reanalysis (Dee et al., 2011) with a spatial resolution of 1.5°. The model runs in a climate mode and thus, it is not nudged towards the reanalysis except at the boundaries.

The meteorological variables of interest are daily average temperature, daily minimum temperature and daily maximum temperature and we will study them on three diagnostic domains described above.

Fig. 3.3 shows boxplots of daily domain averaged mean, minimum and maximum temperatures for each season and diagnostic domains. We will describe the distribution of modelled 2 m temperature and compare it to the distribution of observed temperature, i.e. the interest is put on temperature variability and not on the model error which is described later. For mean 2 m temperature, it can be seen that the UW-PBL scheme distribution matches best the observations in winter, the Holtslag scheme better captures observations in spring except higher

extreme values, both schemes fail to estimate the mean temperature in summer, and both schemes are acceptable in autumn except extreme values which are not captured. Regarding minimum 2 m temperature, the UW-PBL scheme is closest to observations in winter and spring (except Central Europe where the Holtslag scheme is better in spring) but extreme values are higher than observed extremes, both schemes provide similar results in summer, and the UW-PBL scheme better captures observations in autumn but lower extreme values are not captured well compared to observations. For maximum 2 m temperature, the Holtslag scheme falls closer to observations in winter, both schemes underestimate (according to the median) the maximum temperature in spring and even more in summer, and both schemes provide similar results in autumn but higher extreme values are not captured well compared to observations.

Fig. 3.4 shows verification results in a form of biases and standard deviations of daily mean, minimum and maximum temperatures at 2 m. For mean temperature, it can be seen that the UW-PBL scheme bias is shifted consistently from the Holtslag scheme by 0.8 °C. Biases are close to zero in winter and autumn, and the forecast is underestimated in summer. Standard deviations are close to 2.5 °C except the Central Europe domain in winter and autumn where they are smaller with values of 2.0 °C. For minimum temperature, the bias shift of the UW-PBL scheme is also present and standard deviations are 3.0 °C. Regarding maximum temperature, biases in the Balkans domain during spring and summer are significantly high, up to −7 °C, when compared to other domains which is not desired. Standard deviations range from 2.0 °C in winter and autumn for the Central Europe domain, up to 4.0 °C for the Balkans domain in spring and summer. For all temperatures, there is a annual variation in bias which is present in all domains. Generally, biases in spring and summer are higher than in winter and autumn. Both the Holtslag scheme and the UW-PBL scheme provide very similar standard deviations.

Because the two PBL parametrizations perform better compared to each other in different seasons as was presented in Fig. 3.3 and 3.4 (i.e. there is no clear conclusion on which provide more accurate model results), we will use both schemes in experiments described below.

3.1.3 Experiments

The main characteristics of these experiments is the replacement of the RegCM screen level temperature interpolation scheme (Section 3.1.1.2) by the ALADIN screen level temperature interpolation scheme (Section 3.1.1.1) over land. Following RegCM source files were modified

- mod_clm_baregroundfluxes.F90 which performs the calculation of surface fluxes for bare ground and additional variables such as temperature at 2 m,
- mod_clm_canopyfluxes.F90 which calculates surface fluxes, leaf fluxes, transpiration, photosynthesis for canopy and additional variables such as temperature at 2 m,
- mod_clm_slakefluxes.F90 which computes surface fluxes for lakes and additional variables such as temperature at 2 m,

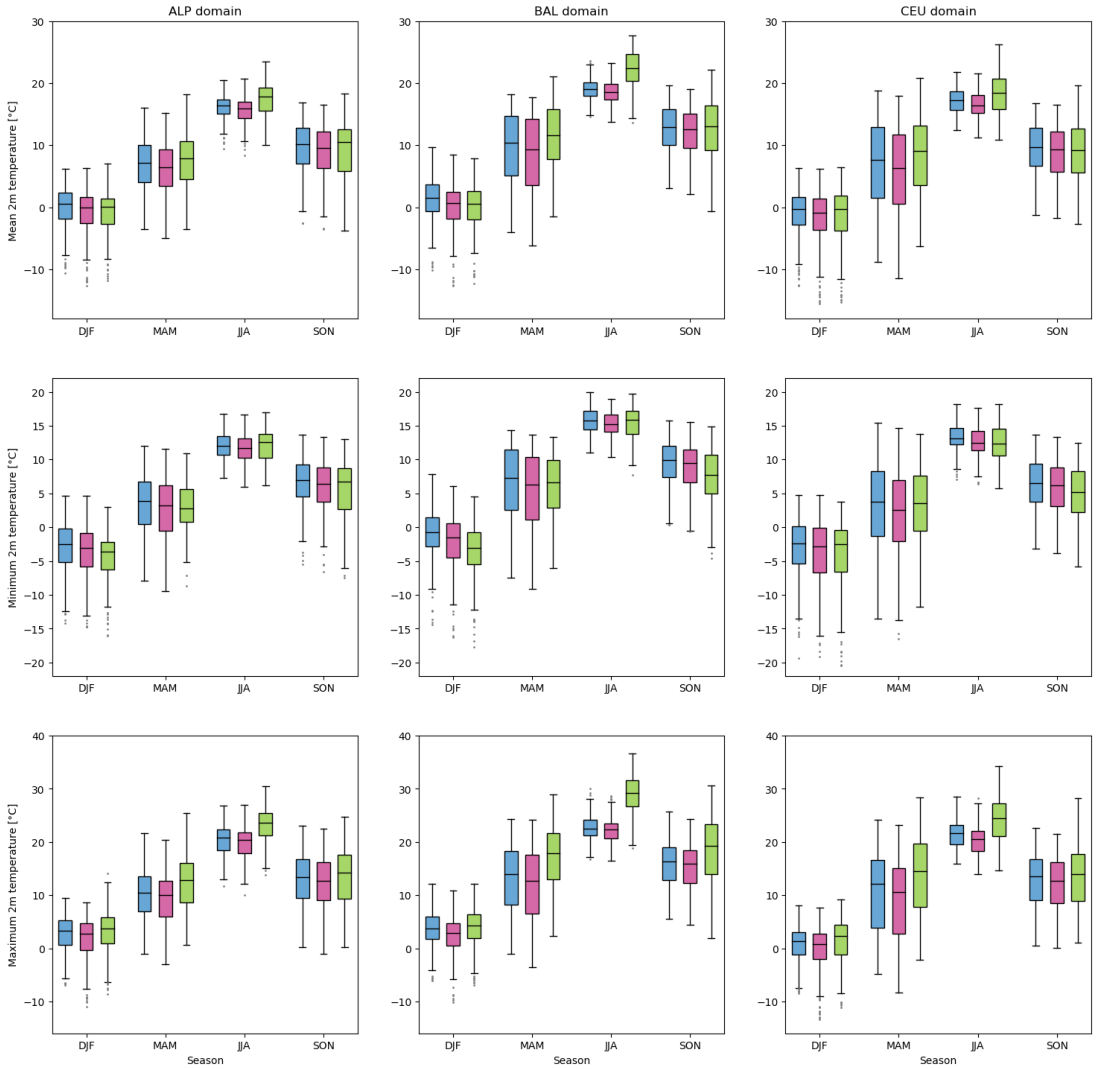

Figure 3.3: Daily domain averaged mean, minimum and maximum temperatures (rows) at 2 m for three diagnostic domains (columns) and for each season. Data from the years 2012 and 2013 are used. The diagnostic domains are: The Alpine Region (ALP), The Balkans (BAL) and Central Europe (CEU). Seasons are abbreviated in the following manner: winter (DJF), spring (MAM), summer (JJA) and autumn (SON). Experiments with two PBL parametrizations, the Holtslag scheme (blue) and the UW-PBL scheme (red), are shown. For comparison, gridded observational E-OBS data (green) are shown as well. A box of a boxplot represents the range between the first quartile (lower horizontal line) and the third quartile (upper horizontal line). The median is shown as a black horizontal line inside the box. Whiskers of a boxplot extend to extreme values, but no further than 1.5x box height from the top/bottom of the box. More distant values are assumed as outliers and are displayed by points.

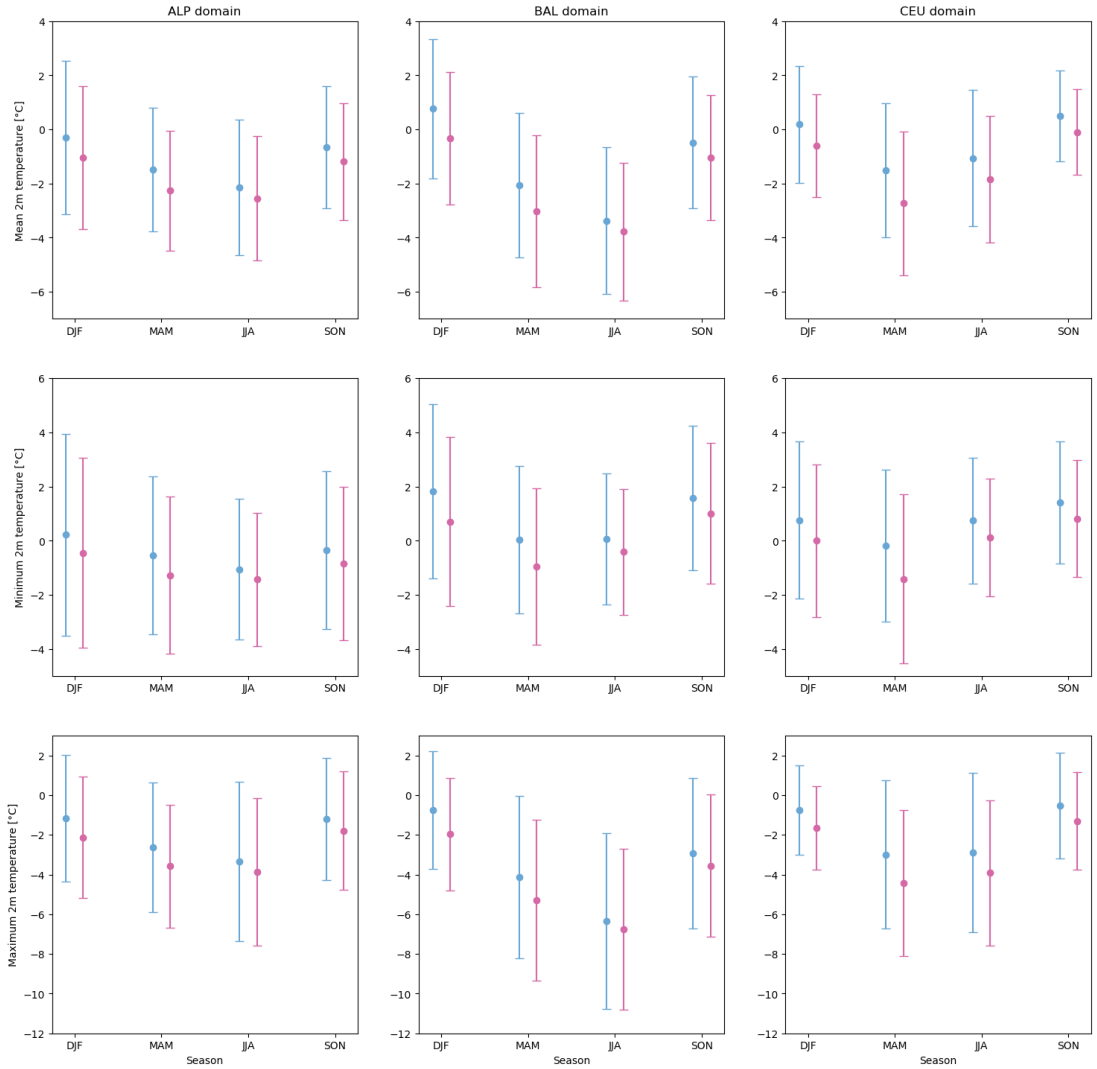

Figure 3.4: Verification of daily mean, minimum and maximum temperatures (rows) at 2 m for three diagnostic domains (columns) and for each season. Biases (points) and standard deviations (error bars) are plotted. Data from the years 2012 and 2013 are used. The diagnostic domains are: The Alpine Region (ALP), The Balkans (BAL) and Central Europe (CEU). Seasons are abbreviated in the following manner: winter (DJF), spring (MAM), summer (JJA) and autumn (SON). Experiments with two PBL parametrizations, the Holtslag scheme (blue) and the UW-PBL scheme (red), are shown.

all located in the directory Main/clmlib/clm4.5 which contains source files for the used land surface model CLM4.5.

There are additional modifications to the original ALADIN screen level interpolation scheme when it is used in RegCM. Friction velocity u_* and Monin-Obukhov length L are passed from an original RegCM function so that they are the same for screen level interpolation and turbulence. Roughness length for heat z_{0h} is also passed from an original RegCM function instead of setting it to $z_{0m}/10$

as in ALADIN where z_{0m} is roughness length for momentum (with an omitted contribution of sub-grid orography). Specific heat of air at constant pressure c_p at the surface, the lowest model level and 2 m is set to the specific heat of dry air at constant pressure $c_{pd} = 1004\,\mathrm{J\,K^{-1}\,kg^{-1}}$ according to the original RegCM screen level interpolation.

Differences described below are calculated between these individual experiments and the references described in Section 3.1.2.

In Fig. 3.5, multi-year seasonal averaged 2 m temperature difference between the ALADIN and the RegCM screen level interpolation scheme is shown for spring. It can be seen that the difference is negative over a large part of the domain. Note the scale maximum absolute value of 0.5 °C and minimum absolute value of 0.01 °C. The 2 m temperature difference between the ALADIN and the RegCM interpolation scheme is subtle.

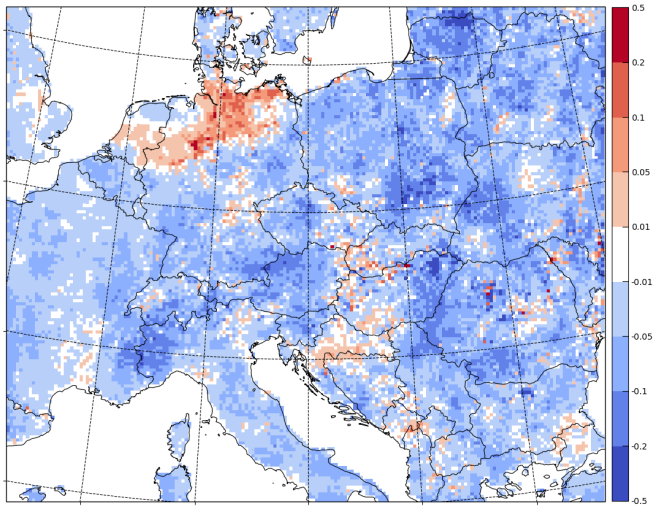

Figure 3.5: Multi-year seasonal averaged 2 m temperature difference (in °C) between the ALADIN and the RegCM screen level interpolation scheme for spring. Data from the years 2012 and 2013 are used. Experiments use the Holtslag scheme.

We will now look closer at how the replacement of the RegCM screen level interpolation scheme by the ALADIN scheme influenced verification scores. Fig. 3.6 shows differences in verification scores (bias, standard deviation) of daily mean, minimum and maximum temperatures at 2 m between the ALADIN and the RegCM screen level interpolation scheme. It can be seen that bias differences are unambiguously negative and standard deviation differences are positive or near zero. We will now describe how the differences of standard deviations were affected. For mean temperature, differences are much higher in spring and summer than in winter and autumn except the Alpine Region. Regarding minimum temperature, the results are inconsistent over diagnostic domains, seasons and PBL parametrizations. However, the lowest increase in the standard deviation differences occur in summer except the UW-PBL scheme for Central Europe. For maximum temperature, differences are lowest in winter and spring. The highest differences are in summer for Central Europe.

Even thought standard deviations are consistently higher in all cases, it should be emphasized that the differences are very small compared to absolute values of standard deviations in Fig. 3.4 which also holds for biases. The results are not unexpected due the use of a less complex screen level interpolation scheme from ALADIN compared to the one in RegCM. Generally, the lowest differences in standard deviations occur in stable conditions (winter, autumn) except the Alpine Region.

3.1.4 Conclusion

The experiments were characterized by the replacement of the RegCM screen level temperature interpolation scheme by the ALADIN scheme over land. The RegCM code was modified accordingly in CLM4.5 routines with some additional modifications.

It was illustrated that 2 m temperature differences (ALADIN – RegCM) are negative over a large part of the domain (Fig. 3.5), but these differences are mostly very small. Then, verification scores of experiments were compared to references (Fig. 3.6) for daily mean, minimum and maximum temperatures at 2 m. The differences in standard deviations are positive for all cases or near zero which is not unexpected due to the use of a less complex screen level interpolation scheme from ALADIN compared to the RegCM screen level interpolation scheme.

However, the differences in verification scores (bias, standard deviation) are not significant compared to absolute values of these scores. Therefore, this also demonstrates that the use of a less complex screen level interpolation scheme is beneficial in NWP where there is an emphasis on computational efficiency compared to climate models. Overall deterioration is acceptable, and in terms of standard deviation it is weakest in stable conditions (autumn, winter).

If analytical integrable stability functions closer to equations (3.23) than Geleyn functions (the equation (3.9)) could be found, the difference between the RegCM and the ALADIN screen level interpolation would be even smaller.

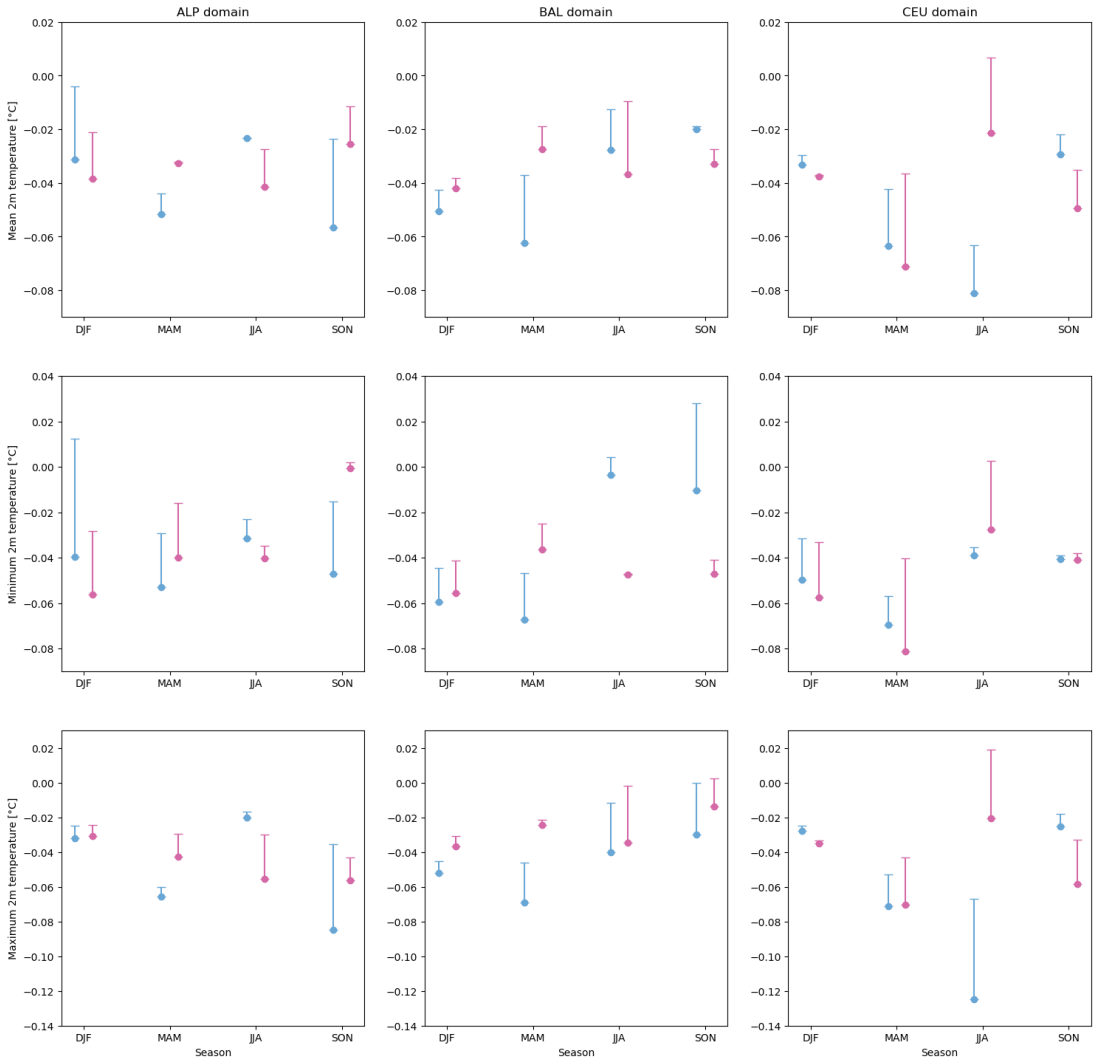

Figure 3.6: Differences in verification scores of daily mean, minimum and maximum temperatures (rows) at 2 m between the ALADIN and the RegCM screen level interpolation scheme for three diagnostic domains (columns) and for each season. Differences (ALADIN – RegCM) of biases (points) and standard deviations (error bars) are plotted. If an error bar is plotted above a point, the ALADIN screen level interpolation scheme has a higher standard deviation compared to the RegCM scheme. If the error bar is plotted below the point, the opposite is true. Data from the years 2012 and 2013 are used. The diagnostic domains are: The Alpine Region (ALP), The Balkans (BAL) and Central Europe (CEU). Seasons are abbreviated in the following manner: winter (DJF), spring (MAM), summer (JJA) and autumn (SON). Experiments using two PBL parametrizations, the Holtslag scheme (blue) and the UW-PBL scheme (red), are shown.

Conclusion

In this text, we studied the influence of selected parametrizations on temperature (and other variables). In Chapter 1, a description of the NWP model ALADIN and the regional climate model RegCM was given. Their dynamical core, history and used parametrizations were described. This helped in next chapters to better orient how those models work and when are they used.

Chapter 2 presented three individual cases using the model ALADIN when some effects on temperature were studied. In low cloudiness case, the aim was to study the unification of the vertical critical relative humidity profiles for the stratiform cloud water in radiation and in microphysics according to the one for microphysics. The direct consequence was the reduction of low clouds due to higher critical relative humidity needed for the cloud formation. We described in detail what happened with cloud water for radiation when using a more realistic critical relative humidity profile and when removing some auxiliary parameters, such as RPHI0 which was set to zero. Several feedback loops were studied according to Fig. 2.10 and thoroughly described. Moreover, we used the radiation ACRANEB2 SCM to detect dominant exchange type causing observed longwave response. The dominant process which influenced temperature at 2 m was the change in surface longwave net radiation flux due to a cloudiness reduction (caused by the changes in the model setup). However, the changes made in the experiment were not suitable for further use due to the significant cloud reduction, the worsening of several verification scores and the binary behaviour of the low clouds cover.

Next, in gravity waves case, we activated the GWD parametrization with its tuning taken from the model version used with the horizontal resolution of 4.7 km. A direct consequence of this setup was the reduction of wind speed at 10 m over almost the entire model domain. The domain averaged wind speed was also reduced. The diagram in Fig. 2.29 represented several feedback loops which were thoroughly described. The dominant process which influenced temperature at 2 m was the change in sensible heat flux before noon and in the evening due to more stable conditions between the surface and the lowest model level. It was shown that for further development, it is possible to keep the GWD parametrization activated, but it is needed to lower its impact via additional tuning.

Finally, in overestimated minimum temperature case, the tuning of the thermic coefficient C_V for vegetation, the bare ground thermic coefficient C_G, and the coefficient n were undertaken for spring and winter case. We created a simple 3-layer model which showed that it was able to represent some temperature characteristics due to a thermic coefficient change. It was found that for the spring case, the tuning works well for Doksany, but minimum night-time temperatures were underestimated for some stations nearby. The main notion was that a high resolution physiography datasets is important for accurate predictions of 2 m temperature, and a more complex snow scheme discriminating between soil and snow temperatures is needed.

In Chapter 3, a description of RegCM modelled temperature in years 2012 and 2013 was provided. Screen level temperature was compared to gridded observational E-OBS dataset and the results were verified. Then, we replaced the

RegCM screen level temperature interpolation scheme by the ALADIN scheme over land and added some small modifications to it. It was presented that temperature differences (ALADIN – RegCM) were negative over a large part of the domain, but they were mostly extremely small. Due to less complex screen interpolation scheme from ALADIN, the differences in standard deviations were positive for all cases or near zero. As a result, it was demonstrated that the use of a less complex screen level interpolation scheme is beneficial in NWP where there is an emphasis on computational efficiency.

Bibliography

I. Bašták Ďurán, J.-F. Geleyn, and F. Váňa. A Compact Model for the Stability Dependency of TKE Production–Destruction–Conversion Terms Valid for the Whole Range of Richardson Numbers. *Journal of the Atmospheric Sciences*, 71(8):3004–3026, 2014.

I. Bašták Ďurán, J.-F. Geleyn, F. Váňa, J. Schmidli, and R. Brožková. A Turbulence Scheme with Two Prognostic Turbulence Energies. *Journal of the Atmospheric Sciences*, 75(10):3381–3402, 2018.

P. Bénard, J. Vivoda, J. Mašek, P. Smolíková, K. Yessad, Ch. Smith, R. Brožková, and J.-F. Geleyn. Dynamical kernel of the Aladin–NH spectral limited-area model: Revised formulation and sensitivity experiments. *Quarterly Journal of the Royal Meteorological Society*, 136(646):155–169, 2010.

A. K. Blackadar. Modeling the Nocturnal Boundary Layer. In *Proceedings of the Third Symposium on Atmospheric Turbulence, Diffusion, and Air Quality*, pages 46–49. American Meteorological Society, Rayeligh, 1976.

G. J. Boer, N. A. McFarlane, R. Laprise, J. D. Henderson, and J.-P. Blanchet. The Canadian Climate Centre spectral atmospheric general circulation model. *Atmosphere-Ocean*, 22(4):397–429, 1984.

C. S. Bretherton, J. R. McCaa, and H. Grenier. A New Parameterization for Shallow Cumulus Convection and Its Application to Marine Subtropical Cloud-Topped Boundary Layers. Part I: Description and 1D Results. *Monthly Weather Review*, 132(4):864–882, 2004.

R. Brožková and J. Mašek. The 3MT Scheme. Presentation, 2020. URL `http://www.umr-cnrm.fr/aladin/IMG/pdf/3mt.pdf`.

R. Brožková, M. Derková, M. Belluš, and A. Farda. Atmospheric forcing by ALADIN/MFSTEP and MFSTEP oriented tunings. *Ocean Science*, 2(2):113–121, 2006.

R. Brožková, A. Bučánek, J. Mašek, P. Smolíková, and A. Trojáková. New high-resolution operational configuration of the ALADIN model. *Meteorological Bulletin*, 72(5):129–139, 2019.

J. A. Businger, J. C. Wyngaard, Y. Izumi, and E. F. Bradley. Flux-Profile Relationships in the Atmospheric Surface Layer. *Journal of Atmospheric Sciences*, 28(2):181–189, 1971.

B. Catry. *Effects of moisture and mountains in Numerical Weather Prediction*. PhD thesis, Ghent University, 2006.

B. Catry, J.-F. Geleyn, M. Tudor, P. Bénard, and A. Trojáková. Flux-conservative thermodynamic equations in a mass-weighted framework. *Tellus A*, 59(1):71–79, 2007.

R. C. Cornes, G. van der Schrier, E. J. M. van den Besselaar, and P. D. Jones. An Ensemble Version of the E-OBS Temperature and Precipitation Data Sets. *Journal of Geophysical Research: Atmospheres*, 123(17):9391–9409, 2018.

D. P. Dee, S. M. Uppala, A. J. Simmons, P. Berrisford, P. Poli, S. Kobayashi, U. Andrae, M. A. Balmaseda, G. Balsamo, P. Bauer, P. Bechtold, A. C. M. Beljaars, L. van de Berg, J. Bidlot, N. Bormann, C. Delsol, R. Dragani, M. Fuentes, A. J. Geer, L. Haimberger, S. B. Healy, H. Hersbach, E. V. Hólm, L. Isaksen, P. Kållberg, M. Köhler, M. Matricardi, A. P. McNally, B. M. Monge-Sanz, J.-J. Morcrette, B.-K. Park, C. Peubey, P. de Rosnay, C. Tavolato, J.-N. Thépaut, and F. Vitart. The ERA-Interim reanalysis: configuration and performance of the data assimilation system. *Quarterly Journal of the Royal Meteorological Society*, 137(656):553–597, 2011.

R. E. Dickinson, A. Henderson-Sellers, and P. J. Kennedy. Biosphere-Atmosphere Transfer Scheme (BATS) Version 1e as Coupled to the NCAR Community Climate Model. Technical Report NCAR/TN-387+STR, UCAR, Boulder, Colorado, 1993.

N. Elguindi, X. Bi, F. Giorgi, B. Nagarajan, J. Pal, F. Solmon, S. Rauscher, A. Zakey, T. O'Brien, R. Nogherotto, and G. Giuliani. Regional Climate Model RegCM: Reference Manual, Version 4.5. Technical report, ICTP, Trieste, Italy, 2014.

J.-F. Geleyn. Interpolation of wind, temperature and humidity values from model levels to the height of measurement. *Tellus A*, 40A(4):347–351, 1988.

J.-F. Geleyn, B. Catry, Y. Bouteloup, and R. Brožková. A statistical approach for sedimentation inside a microphysical precipitation scheme. *Tellus A*, 60(4): 649–662, 2008.

J.-F. Geleyn, J. Mašek, R. Brožková, P. Kuma, D. Degrauwe, G. Hello, and N. Pristov. Single interval longwave radiation scheme based on the net exchanged rate decomposition with bracketing. *Quarterly Journal of the Royal Meteorological Society*, 143(704):1313–1335, 2017.

L. Gerard. ACNEBN radiative cloud properties. Technical report, RC LACE, 2018.

L. Gerard, J.-M. Piriou, R. Brožková, J.-F. Geleyn, and D. Banciu. Cloud and Precipitation Parameterization in a Meso-Gamma-Scale Operational Weather Prediction Model. *Monthly Weather Review*, 137(11):3960–3977, 2009.

F. Giorgi, E. Coppola, F. Solmon, L. Mariotti, M. B. Sylla, X. Bi, N. Elguindi, G. T. Diro, V. Nair, G. Giuliani, U. U. Turuncoglu, S. Cozzini, I. Güttler, T. A. O'Brien, A. B. Tawfik, A. Shalaby, A. S. Zakey, A. L. Steiner, F. Stordal, L. C. Sloan, and C. Brankovic. RegCM4: model description and preliminary tests over multiple CORDEX domains. *Climate Research*, 52:7–29, 2012.

G. A. Grell, J. Dudhia, and D. R. Stauffer. A Description of the Fifth-Generation Penn State/NCAR Mesoscale Model (MM5). Technical Report NCAR/TN-398+STR, UCAR, Boulder, Colorado, 1994.

J. C. H. van der Hage. A parameterization of the Wegener-Bergeron-Findeisen effect. *Atmospheric Research*, 39(1):201–214, 1995.

F. E. Hewer and N. Wood. The effective roughness length for scalar transfer in neutral conditions over hilly terrain. *Quarterly Journal of the Royal Meteorological Society*, 124(547):659–685, 1998.

A. A. M. Holtslag, E. I. F. de Bruijn, and H.-L. Pan. A High Resolution Air Mass Transformation Model for Short-Range Weather Forecasting. *Monthly Weather Review*, 118(8):1561–1575, 1990.

P. Huszár, M. Belda, J. Karlický, P. Pišoft, and T. Halenka. The regional impact of urban emissions on climate over central Europe: present and future emission perspectives. *Atmospheric Chemistry and Physics*, 16(20):12993–13013, 2016.

P. Huszár, J. Karlický, J. Ďoubalová, K. Šindelářová, T. Nováková, M. Belda, T. Halenka, M. Žák, and P. Pišoft. Urban canopy meteorological forcing and its impact on ozone and $PM_{2.5}$: role of vertical turbulent transport. *Atmospheric Chemistry and Physics*, 20(4):1977–2016, 2020.

M. Janoušek. Verification package VERAL (Description and User's Guide). Technical report, RC LACE, 1999.

J. T. Kiehl, J. J. Hack, G. B. Bonan, B. A. Boville, B. P. Briegleb, D. L. Williamson, and P. J. Rasch. Description of the NCAR Community Climate Model (CCM3). Technical Report NCAR/TN-420+STR, UCAR, Boulder, Colorado, 1996.

A. M. G. Klein Tank, J. B. Wijngaard, G. P. Können, R. Böhm, G. Demarée, A. Gocheva, M. Mileta, S. Pashiardis, L. Hejkrlik, C. Kern-Hansen, R. Heino, P. Bessemoulin, G. Müller-Westermeier, M. Tzanakou, S. Szalai, T. Pálsdóttir, D. Fitzgerald, S. Rubin, M. Capaldo, M. Maugeri, A. Leitass, A. Bukantis, R. Aberfeld, A. F. V. van Engelen, E. Forland, M. Mietus, F. Coelho, C. Mares, V. Razuvaev, E. Nieplova, T. Cegnar, J. Antonio López, B. Dahlström, A. Moberg, W. Kirchhofer, A. Ceylan, O. Pachaliuk, L. V. Alexander, and P. Petrovic. Daily dataset of 20th-century surface air temperature and precipitation series for the European Climate Assessment. *International Journal of Climatology*, 22(12):1441–1453, 2002.

R. Laprise. The Euler Equations of Motion with Hydrostatic Pressure as an Independent Variable. *Monthly Weather Review*, 120(1):197–207, 1992.

R. S. Lindzen. Turbulence and Stress Owing to Gravity Wave and Tidal Breakdown. *Journal of Geophysical Research: Oceans*, 86(C10):9707–9714, 1981.

P. Lopez. Implementation and validation of a new prognostic large-scale cloud and precipitation scheme for climate and data-assimilation purposes. *Quarterly Journal of the Royal Meteorological Society*, 128(579):229–257, 2002.

F. Lott and M. J. Miller. A new subgrid-scale orographic drag parametrization: Its formulation and testing. *Quarterly Journal of the Royal Meteorological Society*, 123(537):101–127, 1997.

J. Mašek. Retuning of Xu-Randall scheme in ALARO-0 physics without 3MT. Technical report, SHMÚ, 2008.

J. Mašek. Problem with screen level temperatures above snow in ISBA scheme. Technical report, CHMI, 2017.

J. Mašek, J.-F. Geleyn, R. Brožková, O. Giot, H. O. Achom, and P. Kuma. Single interval shortwave radiation scheme with parameterized optical saturation and spectral overlaps. *Quarterly Journal of the Royal Meteorological Society*, 142 (694):304–326, 2016.

A. S. Monin and A. M. Obukhov. Basic Laws of Turbulent Mixing in the Surface Layer of the Atmosphere. *Contributions of the Geophysical Institute of the Academy of Sciences of the USSR*, 24(151):163–187, 1954.

R. Nogherotto, A. M. Tompkins, G. Giuliani, E. Coppola, and F. Giorgi. Numerical framework and performance of the new multiple-phase cloud microphysics scheme in RegCM4.5: precipitation, cloud microphysics, and cloud radiative effects. *Geoscientific Model Development*, 9(7):2533–2547, 2016.

J. Noilhan and J.-F. Mahfouf. The ISBA land surface parameterisation scheme. *Global and Planetary Change*, 13(1):145–159, 1996.

J. Noilhan and S. Planton. A Simple Parameterization of Land Surface Processes for Meteorological Models. *Monthly Weather Review*, 117(3):536–549, 1989a.

J. Noilhan and S. Planton. A Simple Parametrization of Land Surface Processes for Meteorological Models. *Monthly Weather Review*, 117(3):536–549, 1989b.

K. Oleson, D. M. Lawrence, G. B. Bonan, B. Drewniak, M. Huang, C. D. Koven, S. Levis, F. Li, W. J. Riley, Z. M. Subin, S. Swenson, P. E. Thornton, A. Bozbiyik, R. Fisher, C. L. Heald, E. Kluzek, J.-F. Lamarque, P. J. Lawrence, L. R. Leung, W. Lipscomb, S. P. Muszala, D. M. Ricciuto, W. J. Sacks, Y. Sun, J. Tang, and Z.-L. Yang. Technical description of version 4.5 of the Community Land Model (CLM). Technical Report NCAR/TN-503+STR, UCAR, Boulder, Colorado, 2013.

K. W. Oleson, G. B. Bonan, J. Feddema, M. Vertenstein, and C. S. B. Grimmond. An Urban Parameterization for a Global Climate Model. Part I: Formulation and Evaluation for Two Cities. *Journal of Applied Meteorology and Climatology*, 47(4):1038–1060, 04 2008.

J.-M. Piriou. Diagnostics in Horizontal Domains (DDH). ALADIN documentation, Météo-France, 2018.

L. D. Rotstayn, B. F. Ryan, and J. J. Katzfey. A Scheme for Calculation of the Liquid Fraction in Mixed-Phase Stratiform Clouds in Large-Scale Models. *Monthly Weather Review*, 128(4):1070–1088, 2000.

A. J. Simmons and D. M. Burridge. An Energy and Angular-Momentum Conserving Vertical Finite-Difference Scheme and Hybrid Vertical Coordinates. *Monthly Weather Review*, 109(4):758–766, 1981.

F. Taillefer. CANARI: Technical Documentation. Technical report, Météo-France, Toulouse, France, 2002.

C. Temperton, M. Hortal, and A. Simmons. A two-time-level semi-Lagrangian global spectral model. *Quarterly Journal of the Royal Meteorological Society*, 127(571):111–127, 2001.

P. Termonia, C. Fischer, E. Bazile, F. Bouyssel, R. Brožková, P. Bénard, B. Bochenek, D. Degrauwe, M. Derková, R. El Khatib, R. Hamdi, J. Mašek, P. Pottier, N. Pristov, Y. Seity, P. Smolíková, O. Španiel, M. Tudor, Y. Wang, C. Wittmann, and A. Joly. The ALADIN System and its canonical model configurations AROME CY41T1 and ALARO CY40T1. *Geoscientific Model Development*, 11(1):257–281, 2018.

M. Tiedtke. Representation of Clouds in Large-Scale Models. *Monthly Weather Review*, 121(11):3040–3061, 1993.

M. Tiedtke. An Extension of Cloud-Radiation Parameterization in the ECMWF Model: The Representation of Subgrid-Scale Variations of Optical Depth. *Monthly Weather Review*, 124(4):745–750, 1996.

A. Untch and M. Hortal. A finite-element scheme for the vertical discretization of the semi-Lagrangian version of the ECMWF forecast model. *Quarterly Journal of the Royal Meteorological Society*, 130(599):1505–1530, 2004.

J. Vivoda and P. Smolíková. Finite elements used in the vertical discretization of the fully compressible forecast model ALADIN-NH. *ALADIN-HIRLAM Newsletter*, No. 1:31–46, 2013.

Y. Wang, M. Belluš, A. Ehrlich, M. Mile, N. Pristov, P. Smolíková, O. Španiel, A. Trojáková, R. Brožková, J. Cedilnik, D. Klarić, T. Kovačić, J. Mašek, F. Meier, B. Szintai, S. Tascu, J. Vivoda, C. Wastl, and C. Wittmann. 27 Years of Regional Cooperation for Limited Area Modelling in Central Europe. *Bulletin of the American Meteorological Society*, 99(7):1415–1432, 2018.

K.-M. Xu and D. A. Randall. A Cloudiness Parameterization for Use in Climate Models. *Journal of the Atmospheric Sciences*, 53(21):3084–3102, 1996.

X. Zeng, M. Zhao, and R. E. Dickinson. Intercomparison of Bulk Aerodynamic Algorithms for the Computation of Sea Surface Fluxes Using TOGA COARE and TAO Data. *Journal of Climate*, 11(10):2628–2644, 1998.

List of Figures

2.1 The ALADIN/CHMI model domain with the resolved orography (in meters) used for all experiments. 10
2.2 Scheme of the surface-atmosphere interface with associated fluxes. Red color indicates fluxes which add energy to the surface soil layer; blue color indicates fluxes which remove energy from the surface soil layer. 12
2.3 Scheme of important radiation and microphysics routines in ALADIN that are relevant to cloud cover and cloud water. Blocks with a gray background are used for routines and blocks with a white background indicate input parameters. 14
2.4 Precipitation accumulated in 24 hours (in mm) for the reference on 29.1.2017, 0 UTC. Integration starts on 28.1.2017, 0 UTC. . . 18
2.5 Low cloudiness (in oktas) for the reference on 29.1.2017, 0 UTC. Integration starts on 28.1.2017, 0 UTC. 18
2.6 Evolution of domain averaged surface energy budget and associated fluxes (in W/m^2) for the reference. Integration starts on 28.1.2017, 0 UTC. 19
2.7 Low cloudiness (in oktas) for the experiment with unified critical relative humidity profiles on 29.1.2017, 0 UTC. Integration starts on 28.1.2017, 0 UTC. 21
2.8 Vertical profiles of domain averaged cloud liquid water for radiation (in g/kg) for the experiment with unified critical relative humidity profiles (orange), the reference (red) and their difference (dashed) on 29.1.2017, 0 UTC. Integration starts on 28.1.2017, 0 UTC. The image contains two scales. The lower scale is for reference and experiment values, and the upper scale is for their difference. . . . 21
2.9 Vertical profiles of domain averaged cloud liquid water for microphysics (in g/kg) for the experiment with unified critical relative humidity profiles (orange), the reference (red) and their difference (dashed) on 29.1.2017, 0 UTC. Integration starts on 28.1.2017, 0 UTC. The image contains two scales. The lower scale is for reference and experiment values, and the upper scale is for their difference. 22
2.10 Diagram of feedback loops with numbered paths for the experiment with unified critical relative humidity profiles. 22
2.11 Vertical profiles of domain averaged cloud fraction for radiation (dimensionless) for the experiment with unified critical relative humidity profiles (orange) and the reference (red) on 28.1.2017, 12 UTC. Integration starts on 28.1.2017, 0 UTC. 23
2.12 Evolution of domain averaged surface energy budget and associated fluxes (in W/m^2) for the difference between the experiment with unified critical relative humidity profiles and the reference. Integration starts on 28.1.2017, 0 UTC. 24

2.13 Vertical profiles of domain averaged temperature (in °C) for the experiment with unified critical relative humidity profiles (orange), the reference (red) and their difference (dashed) on 29.1.2017, 0 UTC. Integration starts on 28.1.2017, 0 UTC. The lowest model level corresponds to the surface. The image contains two scales. The lower scale is for reference and experiment values, and the upper scale is for their difference. 25
2.14 Vertical profiles of thermal heating rate (in K/day) for the experiment with unified critical relative humidity profiles (orange), the reference (red) and their difference (dashed) calculated on averaged inputs from 28.1.2017, 12 UTC. The image contains two scales. The lower scale is for reference and experiment values, and the upper scale is for their difference. 26
2.15 Vertical profiles of cooling-to-space heating rate (in K/day) for the experiment with unified critical relative humidity profiles (orange), the reference (red) and their difference (dashed) calculated on averaged inputs from 28.1.2017, 12 UTC. The image contains two scales. The lower scale is for reference and experiment values, and the upper scale is for their difference. 27
2.16 Domain averaged temperature budget (in K/day) for the difference between the experiment with unified critical relative humidity profiles and the reference on 29.1.2017, 0 UTC. Integration starts on 28.1.2017, 0 UTC. 28
2.17 Evolution of domain averaged surface temperature (in °C) for the experiment with unified critical relative humidity profiles (orange), the reference (red) and their difference (dashed). Integration starts on 28.1.2017, 0 UTC. The image contains two scales. The left scale is for reference and experiment values, and the right scale is for their difference. 28
2.18 Evolution of domain averaged temperature at 2 m (in °C) for the experiment with unified critical relative humidity profiles (orange), the reference (red) and their difference (dashed). Integration starts on 28.1.2017, 0 UTC. The image contains two scales. The left scale is for reference and experiment values, and the right scale is for their difference. 29
2.19 Vertical profiles of domain averaged specific humidity (in g/kg) for the experiment with unified critical relative humidity profiles (orange), the reference (red) and their difference (dashed) on 29.1.2017, 0 UTC. Integration starts on 28.1.2017, 0 UTC. The image contains two scales. The lower scale is for reference and experiment values, and the upper scale is for their difference. 31
2.20 Domain averaged water vapour budget (in g/kg/day) for the difference between the experiment with unified critical relative humidity profiles and the reference on 29.1.2017, 0 UTC. Integration starts on 28.1.2017, 0 UTC. 32

2.21 Evolution of domain averaged deep temperature (in °C) for the experiment with unified critical relative humidity profiles (orange), the reference (red) and their difference (dashed). Integration starts on 28.1.2017, 0 UTC. The image contains two scales. The left scale is for reference and experiment values, and the right scale is for their difference. 32
2.22 Evolution of verification scores with the forecast range for the experiment with unified critical relative humidity profiles (orange) and the reference (red). Verification is done for five consecutive 72 hour forecasts which start on 27.–31.1.2017, all of them at 0 UTC. The dark red area and the light red area represent one standard deviation and two standard deviations, respectively, from the mean values of reference verification scores. 34
2.23 The vertical profile of Γ in model and in the reality, after (Catry, 2006). 37
2.24 Vertical profile of domain averaged temperature (in °C) for the reference on 28.1.2017, 12 UTC. Integration starts on 28.1.2017, 0 UTC. 40
2.25 Evolution of domain averaged surface energy budget and associated fluxes (in W/m^2) for the reference. Integration starts on 28.1.2017, 0 UTC. 41
2.26 The difference of wind speed at 10 m above the surface (in m/s) between the experiment with parametrized gravity waves and the reference on 29.1.2017, 0 UTC. Integration starts on 28.1.2017, 0 UTC. 42
2.27 Vertical profiles of domain averaged wind speed (in m/s) for the experiment with parametrized gravity waves (orange), the reference (red) and their difference (dashed) on 29.1.2017, 0 UTC. Integration starts on 28.1.2017, 0 UTC. The image contains two scales. The lower scale is for reference and experiment values, and the upper scale is for their difference. 43
2.28 Vertical profile of domain averaged wind direction (in degrees) for the experiment with parametrized gravity waves on 28.1.2017, 12 UTC. Integration starts on 28.1.2017, 0 UTC. 44
2.29 Diagram of feedback loops with numbered paths for the experiment with parametrized gravity waves. 44
2.30 Evolution of domain averaged surface energy budget and associated fluxes (in W/m^2) for the difference between the experiment with parametrized gravity waves and the reference. Integration starts on 28.1.2017, 0 UTC. 45
2.31 Vertical profiles of domain averaged cloud fraction for radiation (dimensionless) for the experiment with parametrized gravity waves (orange) and the reference (red) on 28.1.2017, 12 UTC. Integration starts on 28.1.2017, 0 UTC. 46

2.32 Vertical profiles of domain averaged temperature (in °C) for the experiment with parametrized gravity waves (orange), the reference (red) and their difference (dashed) on 29.1.2017, 0 UTC. Integration starts on 28.1.2017, 0 UTC. The lowest model level corresponds to the surface. The image contains two scales. The lower scale is for reference and experiment values, and the upper scale is for their difference. 47
2.33 Domain averaged temperature budget (in K/day) for the difference between the experiment with parametrized gravity waves and the reference on 29.1.2017, 0 UTC. Integration starts on 28.1.2017, 0 UTC. 47
2.34 Vertical profiles of domain averaged specific humidity (in g/kg) for the experiment with parametrized gravity waves (orange), the reference (red) and their difference (dashed) on 29.1.2017, 0 UTC. Integration starts on 28.1.2017, 0 UTC. The image contains two scales. The lower scale is for reference and experiment values, and the upper scale is for their difference. 48
2.35 Domain averaged water vapour budget (in g/kg/day) for the difference between the experiment with parametrized gravity waves and the reference on 29.1.2017, 0 UTC. Integration starts on 28.1.2017, 0 UTC. 48
2.36 Evolution of domain averaged surface temperature (in °C) for the experiment with parametrized gravity waves (orange), the reference (red) and their difference (dashed). Integration starts on 28.1.2017, 0 UTC. The image contains two scales. The left scale is for reference and experiment values, and the right scale is for their difference. 49
2.37 Evolution of domain averaged temperature at 2 m (in °C) for the experiment with parametrized gravity waves (orange), the reference (red) and their difference (dashed). Integration starts on 28.1.2017, 0 UTC. The image contains two scales. The left scale is for reference and experiment values, and the right scale is for their difference. 50
2.38 Snow cover (in kg/m^2) for the reference on 28.1.2017, 12 UTC. Integration starts on 28.1.2017, 0 UTC. 52
2.39 Evolution of domain averaged deep temperature (in °C) for the experiment with parametrized gravity waves (orange), the reference (red) and their difference (dashed). Integration starts on 28.1.2017, 0 UTC. The image contains two scales. The left scale is for reference and experiment values, and the right scale is for their difference. 52
2.40 Evolution of verification scores with the forecast range for the experiment with parametrized gravity waves (orange) and the reference (red). Verification is done for one 72 hour forecast which starts on 28.1.2017, 0 UTC. 54
2.41 Scheme of the 3-layer surface-atmospheric model with associated fluxes. The arrow thickness corresponds to the relative ratios of the absolute daily averaged flux values. 58

2.42 Evolution of surface energy budget and associated fluxes (in W/m^2) for the 3-layer model reference where $C_T = 0.8\times10^{-5}\,K\,m^{-2}\,J^{-1}$. Integration starts at 0 UTC. 59
2.43 Evolution of surface temperature (in °C) for the 3-layer model experiment where $C_T = 1.0\times10^{-5}\,K\,m^{-2}\,J^{-1}$ (orange) and the reference where $C_T = 0.8\times10^{-5}\,K\,m^{-2}\,J^{-1}$ (blue). Integration starts at 0 UTC. 59
2.44 Evolution of 2 m temperature (in °C) for the references (red) and observations (black dots). 61
2.45 Snow cover (in $kg\,m^{-2}$) for the references. 61
2.46 Evolution of 2 m temperature (in °C) for experiments (orange, light green, dark green, light blue, dark blue), the references (red) and observations (black dots). 63

3.1 The RegCM/CE12 model domain with the resolved orography (in meters) used for all experiments. 64
3.2 Diagnostic domains defined on the RegCM/CE12 model domain. Borders of a diagnostic domain are shown as red lines. The three diagnostic domains are: The Alpine Region (ALP), The Balkans (BAL) and Central Europe (CEU). 66
3.3 Daily domain averaged mean, minimum and maximum temperatures (rows) at 2 m for three diagnostic domains (columns) and for each season. Data from the years 2012 and 2013 are used. The diagnostic domains are: The Alpine Region (ALP), The Balkans (BAL) and Central Europe (CEU). Seasons are abbreviated in the following manner: winter (DJF), spring (MAM), summer (JJA) and autumn (SON). Experiments with two PBL parametrizations, the Holtslag scheme (blue) and the UW-PBL scheme (red), are shown. For comparison, gridded observational E-OBS data (green) are shown as well. A box of a boxplot represents the range between the first quartile (lower horizontal line) and the third quartile (upper horizontal line). The median is shown as a black horizontal line inside the box. Whiskers of a boxplot extend to extreme values, but no further than 1.5x box height from the top/bottom of the box. More distant values are assumed as outliers and are displayed by points. 72
3.4 Verification of daily mean, minimum and maximum temperatures (rows) at 2 m for three diagnostic domains (columns) and for each season. Biases (points) and standard deviations (error bars) are plotted. Data from the years 2012 and 2013 are used. The diagnostic domains are: The Alpine Region (ALP), The Balkans (BAL) and Central Europe (CEU). Seasons are abbreviated in the following manner: winter (DJF), spring (MAM), summer (JJA) and autumn (SON). Experiments with two PBL parametrizations, the Holtslag scheme (blue) and the UW-PBL scheme (red), are shown. 73

3.5 Multi-year seasonal averaged 2 m temperature difference (in °C) between the ALADIN and the RegCM screen level interpolation scheme for spring. Data from the years 2012 and 2013 are used. Experiments use the Holtslag scheme. 74
3.6 Differences in verification scores of daily mean, minimum and maximum temperatures (rows) at 2 m between the ALADIN and the RegCM screen level interpolation scheme for three diagnostic domains (columns) and for each season. Differences (ALADIN – RegCM) of biases (points) and standard deviations (error bars) are plotted. If an error bar is plotted above a point, the ALADIN screen level interpolation scheme has a higher standard deviation compared to the RegCM scheme. If the error bar is plotted below the point, the opposite is true. Data from the years 2012 and 2013 are used. The diagnostic domains are: The Alpine Region (ALP), The Balkans (BAL) and Central Europe (CEU). Seasons are abbreviated in the following manner: winter (DJF), spring (MAM), summer (JJA) and autumn (SON). Experiments using two PBL parametrizations, the Holtslag scheme (blue) and the UW-PBL scheme (red), are shown. 76

List of Tables

1.1 Overview of important parametrizations used in ALADIN and RegCM. Some schemes are referred to using an author name, so the relevant papers are shown. 9

2.1 Full model levels in ALADIN and their corresponding pressure (in hPa) and height above the surface (in meters) according to the International Standard Atmosphere (ISA). 11
2.2 Tuning parameters used in the Xu-Randall scheme. 15
2.3 Tuning parameters used in the calculation of stratiform cloud water. 16
2.4 Tuning parameters used in the gravity wave drag parametrization scheme. 39
2.5 Tuning parameters used in the ISBA scheme. 57

3.1 Full model levels in RegCM and their corresponding pressure (in hPa) and height above the surface (in meters) based on the International Standard Atmosphere (ISA). 65

List of Abbreviations

3MT: Modular Multiscale Microphysics and Transport
ACRANEB2: (fr. *Actif Calcul de Rayonement et Nébulosité, version 2*) Active Radiation and Cloudiness Calculation, version 2
ALADIN: (fr. *Aire Limitée Adaptation Dynamique Développement International*) International Development for Limited-Area Dynamical Adaptation
ALADIN-NH: Nonhydrostatic dynamical core of ALADIN
ALARO: ALADIN–AROME
AROME: Application of Research to Operations at Mesoscale
ARPEGE: (fr. *Action de Recherche Petite Echelle Grande Echelle*) Research Project on Small and Large Scales
BATS: Biosphere–Atmosphere Transfer Scheme
BIAS: bias, also called mean error
CANARI: (fr. *Code d'Analyse Nécessaire à Arpege pour ses Rejets et son Initialisation*) Code for the Analysis Necessary for ARPEGE for Its Rejects and Its Initialization
CCM3: Community Climate Model, version 3
CCSM: Community Climate System Model
CDO: Climate Data Operator
CHMI: Czech Hydrometeorological Institute
CLM: Community Land Model
CLMU: Community Land Model Urban
CMC: Canonical Model Configuration
DDH: (fr. *Diagnostics par Domaines Horizontaux*) Diagnostics on Horizontal Domains
ECA: European Climate Assessment
ECMWF: European Centre for Medium-range Weather Forecasts
E-OBS: European temperature and precipitation dataset
ERA5: ECMWF Reanalysis, version 5
GCM: General Circulation Model or Global Circulation Model, or Global Climate Model
GMTED2010: Global Multi-resolution Terrain Elevation Data 2010
GrADS: Grid Analysis and Display System
GTOPO30: Global Topographic Data with a horizontal grid spacing of 30 arc seconds
GWD: Gravity Wave Drag
ICTP: Abdus Salam International Centre for Theoretical Physics
IFS: Integrated Forecast System
ISA: International Standard Atmosphere
ISBA: (fr. *Interactions Sol-Biosphère-Atmosphère*) Interactions between Soil, Biosphere and Atmosphere
LAM: Limited Area Model
MM4: Penn State/NCAR Mesoscale Model, version 4
MM5: Penn State/NCAR Mesoscale Model, version 5
NCAR: National Center for Atmospheric Research
NCL: NCAR Command Language

NWP: Numerical Weather Prediction
PBL: Planetary Boundary Layer
PFT: Plant Functional Type
RegCM: Regional Climate Model
RegCNET: Regional Climate Research Network
RMSE: Root Mean Squared Error
SCM: Single Column Model
STDE: Standard Deviation
TOM: Third Order Moment
TOUCANS: Third Order Moments Unified Condensation Accounting and N-Dependent Solver
UW-PBL: University of Washington – Planetary Boundary Layer scheme
VERAL: Verification of ALADIN
WRF: Weather Research and Forecasting